Gate Modulated Raman Spectroscopy of Graphene

PhD. Thesis

Gate Modulated Raman Spectroscopy of Graphene

(グラフェンのゲート変調ラマン分光)

Department of Physics

Graduate School of Science, Tohoku University

Eddwi Hesky Hasdeo

September 2016

Acknowledgements

I thank Professor Riichiro Saito for his guidance through five years of my combined master and Ph.D. courses. He aims the highest standard of research, in such way, I am very thankful working under his supervision. His supportive spirit keeps me move forward to the goal. Spending five years in Saito-lab becomes a life-changing moment of my life. I thank Professor Millie Dresselhaus from MIT, for her important support during my visit to MIT. I learned a lot of different properties of atomic layer materials from that visit. When I submitted a manuscript to her in the night, I got the improved version by the next morning! Dr. Izumida provides fruitful inputs during my practice of defense which improves my presentation so much. Dr. Ahmad Ridwan Tresna Nugraha has been the best tutor for me not only in doing physics but also in developing my skill of ping pong, traditional music, writing, and much more. For my lab mates and ex-lab mates, Tareque, Tapsanit, Tatsumi, Thomas, Mizuno, Shoufie, Syahril, Inoue, Nguyen, and Pourya thank you very much for the time we spend together in Saito-lab, it was very fun and challenging as well. I thank Haihao Liu, an exchange student from Rice University, for his comments and suggestions to make this thesis easier to understand. I thank secretaries in Saito Lab and CMPT group: Sumino-san, Sasaki-san, Wako-san, and Sato-san for helping me with necessary documents for traveling, housing, schooling and many more. I acknowledge the financial support from MEXT during my master and Ph.D. courses. Tami, doing our theses together makes this thesis writing the most exciting experience ever. Vicky and Kris, our togetherness will always be the moment I treasure. Last but not least, I give my deep awe to my heroes: Papa, and Mama, for their pray and faith to make their son be as what he is now. I hope this thesis is acceptable for my mother's birthday present.

Contents

Chapter 1

Introduction

1.1 Purpose of the study

Single atomic layer of graphite, known as graphene, becomes the most fundamental material to study physics of two dimensional (2D) systems [1]. A confined electron in the 2D quantum well of graphene behaves as an effectively massless particle [2]. This electronic property is probed by changing the Fermi energy of graphene through application of an electric gate voltage [1, 3, 4, 5, 6, 7, 8]. A combination of electronic gating and inelastic scattering of light, known as Raman spectroscopy, elucidates interplay of electron, phonons, and photons in graphene because we can tune the Fermi energy of graphene while simultaneously probing phonon excitation [9]. Spectral properties such as intensity, spectral linewidth, peak position, and lineshape of the Raman spectra can be modified by varying the gate voltage, indicating an interplay of the electron-phonon interaction. However, the physical consequence behind the change of spectral properties measured by experiment cannot be understood unless a theoretical calculation of Raman intensity is performed. Understanding detailed mechanism underlying the change of Raman spectral properties mentioned above is essential for the progress of solid state physics, in particular, for the description of the electron-photon, electron-phonon, and electron-electron interaction of graphene. **The purpose of this thesis** is to investigate the gate modulated Raman spectroscopy in graphene theoretically and to understand the origin of the change of spectral properties as a function of the Fermi energy.

1.2 Organization of Thesis

The organization of the present thesis is as follows. In Sec. 1.3 we present basic concepts to understand gate modulated Raman spectroscopy and its related phenomena including the Kohn anomaly (KA) effect, the quantum interference effect, and the Breit-Wigner-Fano (BWF) asymmetry of the Raman spectra. In Chapter 2, methods to calculate electron and phonon dispersion relations of graphene; and electron-photon, and electron-phonon matrix elements are presented. In Chapter 3, calculated results for the first-order Raman spectra is presented. We discuss the KA effect, the quantum interference effect and the BWF lineshape of the first-order Raman spectra. The KA effect and the quantum interference effect of the second-order Raman spectra will be given in Chapter 4. Finally, conclusion of this thesis is given in Chapter 5.

1.3 Background

Here we introduce the backgrounds and concepts which are important to this thesis.

1.3.1 Introduction to graphene

Graphene is one-atom-thick structure made out of carbon atoms arranged on a honeycomb lattice. Among various carbon allotropes, graphene serves as the basis for the understanding of the electronic properties of more complex structures. Its three dimensional counterpart, graphite, became widely known after the invention of the pencil in 1564 [10]. The reason why we can use graphite as a pencil comes from the fact that graphite is made out of stacks of graphene layers that are weakly coupled by the van der Waals force. Although graphene is the most fundamental structure among different carbon allotropes and has been presumably produced whenever someone writes with a pencil, graphene was only isolated after 440 years since the invention of pencil [1]. Novoselov et al. isolated graphene in 2004 by exfoliating graphite flakes with scotch (adhesive) tape and they measured its transport properties [1, 11].

One of the most interesting transport properties of graphene is that an electron in graphene behaves as a massless Dirac fermion described by the linear electronic energy dispersion [2, 1, 12]. In undoped graphene, the Fermi energy lies exactly at a crossing point of the two linear energy bands, known as the Dirac point. This dispersion mimics the physics of quantum electrodynamics (QED) for massless fermions except for the fact that in graphene the Dirac fermions move with a speed 300 times slower than the speed of light. Hence, many of the unusual properties of QED can show up in graphene but at much slower speeds. For example, the integer quantum Hall effect (IQHE) can be observed even at room temperature [3, 4, 13].

The Dirac fermions can transmit through a potential barier with 100% probability for a classically forbidden region of energy, known as the Klein tunneling phenomenon [14]. The Klein tunneling in graphene has been predicted in 2006 [12, 15, 16] and observed experimentally in 2007 [17, 5]. Under certain conditions, Dirac fermions are "immune" to localization effects observed in ordinary electrons [18] and it has been established experimentally that electrons can propagate without scattering over large distance of the order of micrometers in graphene [1].

1.3.2 Raman spectroscopy of graphene

Raman spectroscopy is the inelastic scattering of light in which the difference of energy between the incident and scattered light, known as Raman shift, is absorbed by the material through various light-matter interactions. Studying the Raman spectra of materials allows us not only to measure the phonon frequencies that are used for structure characterization but also to measure their electronic structures, phonon dispersion relations, optical properties, and interactions among elementary excitations (electrons, phonons, and photons) [19]. The use of a photon as probe in Raman spectroscopy provides non-destructive characterization technique at room temperature and ambient pressure.

In conventional Raman spectroscopy, we observe excitation of quantized lattice vibrations

Fig. 1-1: fig/ch1-ramanpros.eps

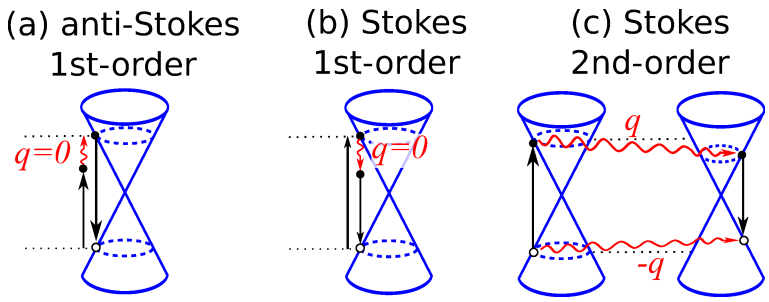

Figure 1-1: Schematics of (a) the first-order anti-Stokes process, (b) the first- and (c) second-order Stokes process. Optical transitions are indicated by straight lines, while the electron-phonon interactions are indicated by wiggly lines.

or phonons. A Raman scattering process consists of (1) an optical transition of an electron from the valence to the conduction bands, (2) the electron-phonon interactions and (3) the electron relaxation back to the valence band by emitting a photon as shown in Fig. 1-1. During the electron-phonon interaction, a phonon can be absorbed, known as the anti-Stokes Raman process [Fig. 1-1(a)], or be emitted known as the Stokes Raman process [Fig. 1-1(b) and (c)]. The anti-Stokes (Stokes) process gives a negative (positive) value of Raman shift because the scattered photon energy is larger (smaller) than the incident photon energy. In this thesis, however, we do not consider the anti-Stokes process and hereafter we simply refer to the Stokes Raman process as the Raman process. The phonon excited during the Raman process can have either a zero momentum $\mathbf{q} = 0$ [Fig. 1-1(b)] or a non-zero momentum $\mathbf{q} \neq 0$ [Fig. 1-1(c)]. The first-order Raman process corresponds to $\mathbf{q} = 0$ phonon emission [Fig. 1-1(b)] while the second-order Raman process corresponds to $\mathbf{q}$ phonon and $-\mathbf{q}$ phonon emission processes [Fig. 1-1(c)] in order for the photoexcited electron to recombine with the hole.

Raman spectroscopy of graphene gives the most fundamental Raman features among sp^2 carbon allotropes. Figure 1-2 shows an example of the Raman spectra in graphene observed by a laser excitation energy $E_{\mathrm{L}} = 3.49\,\mathrm{eV}$ by Liu et al. [20]. The G band occurring at a Raman shift 1600 cm^{-1} originates from vibration of carbon-carbon bond stretching which degenerate in energy for longitudinal optic (LO) and in-plane tangential optic (iTO) modes

Fig. 1-2: fig/ch1-ramanxp.eps

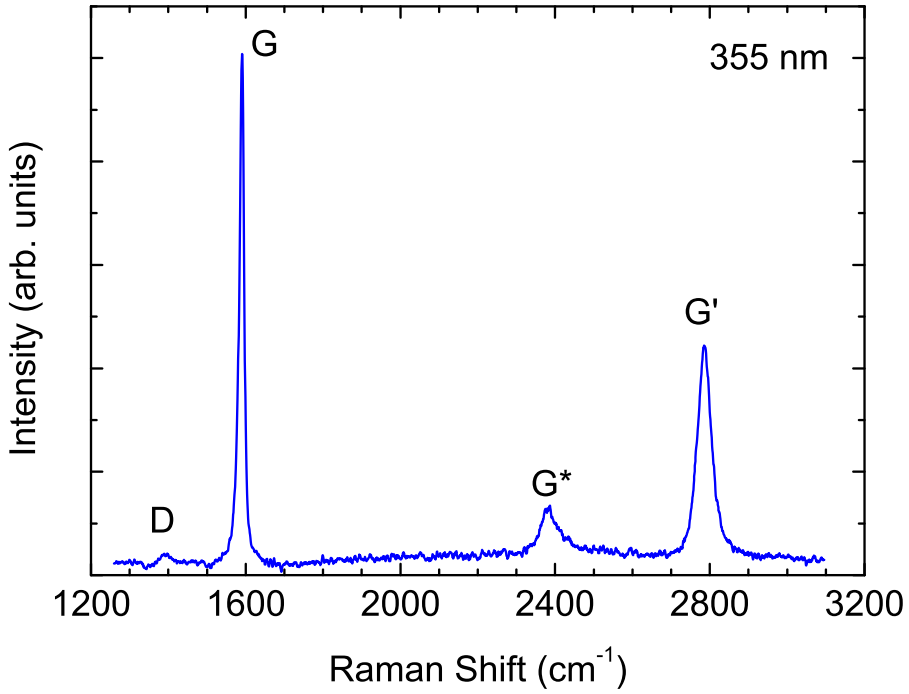

Figure 1-2: An example of the Raman spectra in graphene showing the D ($\sim$ 1400 cm^{-1}), G ($\sim$ 1600 cm^{-1}), G* ($\sim$ 2400 cm^{-1}), and G$'$ ($\sim$ 2800 cm^{-1}) bands for a laser excitation wavelength 355 nm (3.49 eV) from Liu et al. [20].

[see Fig. 2-6 in Chapter 2]. The G band is assigned to the first-order Raman spectra which corresponds to the $\mathbf{q} = 0$ zone-centered (Γ point) phonon as shown in Fig. 1-1(b). The G* and G$'$ bands are also intrinsic Raman features of graphene which are free from the defects in the lattice. Because the Raman shifts of the G$'$ and G* lie above 1600 cm^{-1} which is the largest phonon frequency of a single phonon, the G* and G$'$ bands are assigned to the second-order Raman spectra in which both overtone and combination modes of two phonons with $\mathbf{q} \neq 0$ take place [Fig. 1-1(c)]. We shall discuss detailed origin of the G* and G$'$ bands in Chapter 4.

The G (G$'$) band peak position is dispersionless (dispersive) by changing $E_{\rm L}$. In the case of the G$'$ band, by changing $E_{\rm L}$ the corresponding phonon momentum $\mathbf{q}$ also changes so as to satisfy the resonance condition. Thus the G$'$ band is dispersive as a function of $E_{\rm L}$. The $E_{\rm L}$

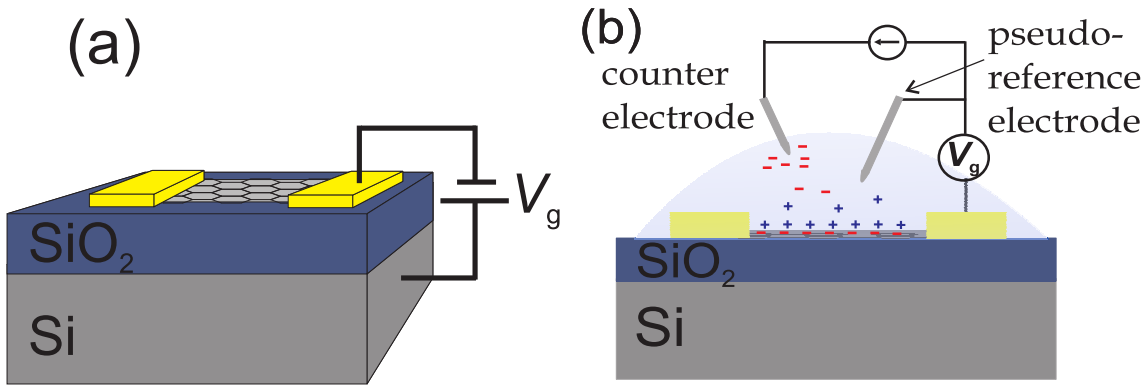

Figure 1-3: (a) Schematic view of the back gate graphene device. A variable voltage V_g can be applied between the graphene and the n-type silicon substrate. The device is treated as a parallel plate capacitor where the silicon oxide layer is the dielectric medium. (b) Schematic view of top gate graphene devices using electrolyte solutions. Figures are taken from Ref. [9]

dependence of the G′ band is important to measure phonon dispersion relation experimentally combined with theory [21]. The intensity ratio $I_{G'}/I_G$ sensitively depends on graphene's number of layers thus it becomes a powerful parameter for the characterization [19].

The D band occurring at ~ 1400 cm^{-1} is a defect oriented Raman feature. The D band is an extrinsic feature of graphene and therefore does not appear if graphene sample does not have any defect. Concentration of point defects (impurities or vacancies) in graphene sample is proportional to the intensity ratio I_D/I_G [22, 23]. The D band peak position, lineshape and intensity are also important to characterize various type of grain boundaries or edges in graphene or in graphene nanoribbon [24, 25, 26, 27]. In this thesis, we exclude the discussion of the D band by assuming clean graphene samples without edges.

1.3.3 Gate modulated Raman spectroscopy

Gate modulated Raman spectroscopy is a method to perform Raman measurements while changing the Fermi energy by applying a gate voltage to the sample. In the experiments, back gated and top gated devices are mostly used. An example of back gated device is shown in Fig. 1-3(a). An applied gate voltage V_g can induce a potential difference between graphene

Fig. 1-3: fig/ch1-gateMR.eps

and the substrate of n-doped silicon separated by an insulator such as silicon oxide (SiO_2) layer. When the V_g is positive or negative relative to the Si substrate, electrons or holes, respectively, are accumulated in the graphene layer. Induced charge density n is proportional to V_g, given by:

$$n = \alpha |V_g|, \tag{1.1}$$

where $\alpha = 7.2 \times 10^{10}$ cm^{-2}V^{-1} is capacitance of the gate for 300 nm-thick SiO_2 [28, 9, 1]. Charge density n is related to E_F of graphene as follows:

$$\begin{aligned} \int_0^{|E_F|} D(E)dE &= n \\ \int_0^{|E_F|} \frac{gE}{2\pi(\hbar v_F)^2} dE &= n \\ \frac{g|E_F|^2}{4\pi(\hbar v_F)^2} &= n \end{aligned} \tag{1.2}$$

where D is the density of state per unit area, $g = 4$ accounting the spin and valley degeneracies and $E = 0$ is taken at the Dirac point. In Eq. (1.2), we have assumed the linear energy dispersion of graphene $E(\mathbf{k}) = \hbar v_F \mathbf{k}$ where $\hbar$ is the Planck constant and $v_F = 10^8$ cm/s is the Fermi velocity of graphene. From Eqs. (1.1) and (1.2), we can relate E_F and V_g as

$$E_F = \text{sign}(V_g)\hbar v_F \sqrt{\pi \alpha |V_g|}, \tag{1.3}$$

where we have defined that + (−) sign of V_g denotes electron (hole) doping.

Figure 1-3(b) shows an example of a top gated device. The polymer electrolyte (liquid, ionic conductor) is put on the sample. When the gate voltage V_g is applied between the sample and a counter electrode, positive (negative) ions from the electrolyte are accumulated near the graphene sample and they form an electric double layer combined with the electrons (holes) in the graphene sample. Most works reviewed in this thesis are related to the bottom gate modulated Raman spectroscopy therefore we use Eq. (1.3) for V_g to E_F conversion.

Fig. 1-4: fig/ch1-yoonexp.eps

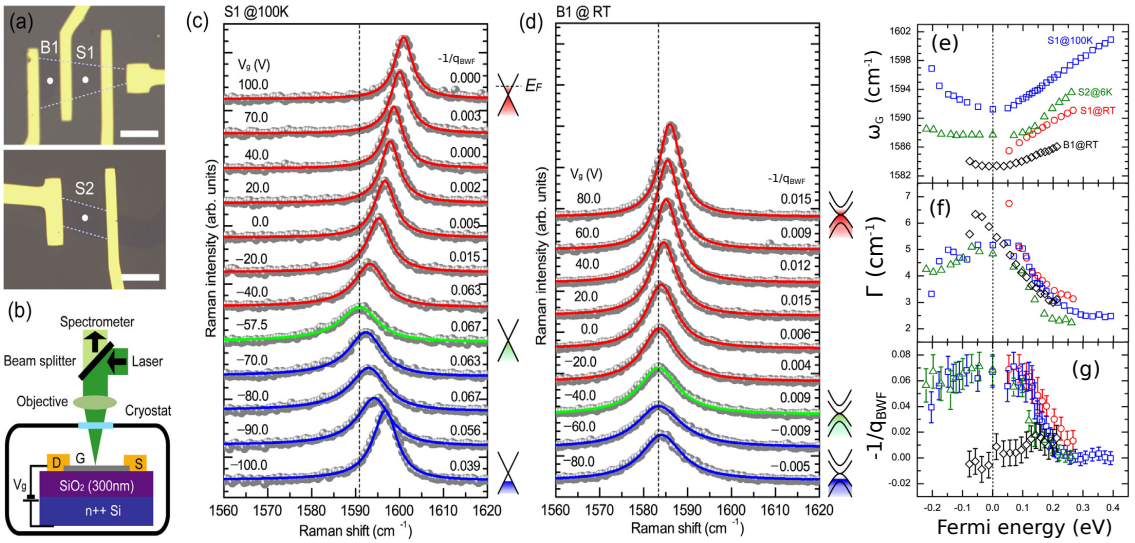

Figure 1-4: An example of a gate modulated Raman measurement by Yoon et al. [28]. (a) Optical microscope images of the back-gated graphene samples. S1 and S2 are single layer graphene samples, and B1 is a bilayer graphene sample. (b) Schematic of the gate modulated Raman measurement set up. (G: graphene, S:source, D: drain, V_g: back-gate bias voltage). (c) G band of the single layer graphene sample (S1) as a function of the back-gate voltage (V_g) at 100 K. The Fermi energy E_F is controlled by V_g. Asymmetric factor of the G band lineshape, $-1/q_{BWF}$, is obtained by fitting to the BWF line shape in Eq. (1.4). (d) G band of the BLG (B1) as a function of V_g at room. (e) G band frequencies ω_G for S1, S2, and B1 as a function of E_F at several temperatures. (f) G band broadening factor Γ and (g) G band asymmetric factor $-1/q_{BWF}$ as a function of E_F.

Figure 1-4 shows an example of a gate modulated Raman measurement by Yoon et al. [28]. They measure the E_F dependence of the G band spectra for two samples of single layer graphene (S1 and S2) and a sample of bilayer graphene (B1) as shown in Fig. 1-4(a). Figure 1-4(b) shows the back gated device with a configuration: (1) metal source (S) and drain (D) electrodes, (2) graphene, (3) SiO_2 and (4) n-type silicon substrate. A gate voltage V_g is applied between n-type silicon substrate and the drain. They convert V_g into E_F according to Eq. (1.3), with a relation $E_F = \mathrm{sign}(V_g - V_0)\hbar v_F \sqrt{\alpha\pi|V_g - V_0|}$ where $V_0 = -57.5$ V is the constant voltage adjusted to the Dirac point in their experiment.

Figures 1-4(c) and (d) show, respectively, the G band spectra for S1 and B1 for several E_F. The G bands for charge neutrality point $E_F = 0$ are shown in green colors and for a positive (negative) E_F values, the G bands are shown in red (blue) colors. The G band

peak position [Fig. 1-4(e)] and linewidth [Fig. 1-4(f)] systematically change upon variation of E_{F}. This phenomenon is known as the Kohn anomaly (KA) effect (see Sec. 1.3.4 for detailed explanation of the KA effect). Furthermore, in single layer graphene, the G band exhibit asymmetric Breit-Wigner-Fano (BWF) lineshape [Eq. (1.4)] with asymmetric factor $1/q_{\mathrm{BWF}}$ also changes by varying E_{F} [Fig. 1-4(g)]. Introduction to the BWF lineshape will be presented in Sec. 1.3.6.

1.3.4 Kohn anomaly effect in graphene

Due to the presence of the gapless linear energy bands of graphene, electrons can easily be excited from the valence band to the conduction band even by a small perturbation. Kohn mentions that a phonon in a metal can excite an electron-hole pair leading to a change of phonon frequency [29] which is known as the Kohn anomaly effect. The change of phonon frequency depends on concentration of the conduction electrons.

KA effect on phonon dispersion of graphene

Phonon dispersion of graphene can be calculated by solving the dynamical matrix based on a force constant model (Sec. 2.2). No matter how accurate our selection of interatomic potential and how precise our calculation by including correction of dynamical matrix from long-range nearest neighbor [27], the calculated results for the highest optical phonon band, LO phonon at the Γ point and iTO phonon at the K point cannot reproduce the experimental results by the force constant model since the experimental results [30, 31] give discontinuous linear bands (kinks) at the Γ and K points as shown in red lines of Fig. 1-5.

Piscanec et al. [32] perform a first-principles calculation as shown in Fig. 1-5(b) for graphene (GE) and graphite (GI) and for two different lattice constants $a_{\mathrm{exp}} = 0.246\,\mathrm{nm}$ and $a_{\mathrm{th}} = 0.2479\,\mathrm{nm}$. In upper panel of Fig. 1-5(b), the calculated results of graphene phonon dispersions are well reproduced the experimental results when using a_{exp} at the Γ point and using a_{th} at the K point. Taking a closer look at the Γ and K points [lower panel of

Fig. 1-5: fig/ch1-phdisp.eps

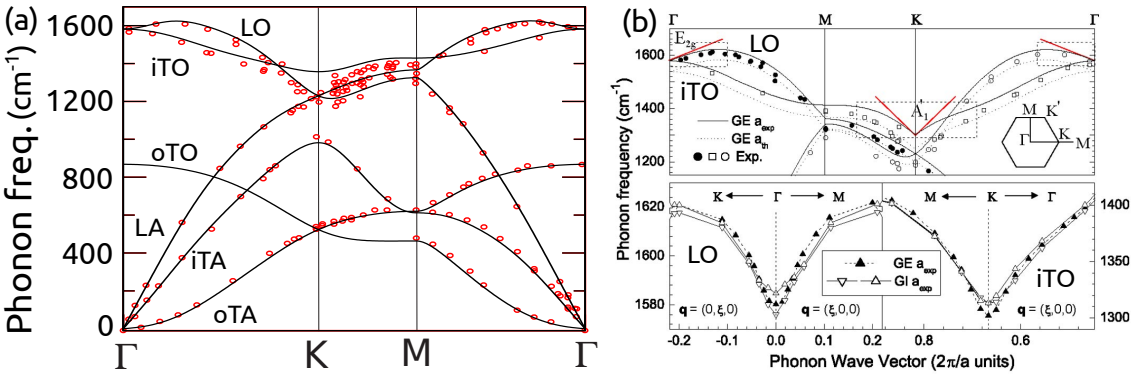

Figure 1-5: (a) Calculation results of phonon dispersion relations from force constant model (lines) compared with experimental results (dots) [30, 31]. (b) Upper panel: phonon dispersion of graphene (GE) from a first principles calculation with lattice constants $a_{\mathrm{exp}} = 0.246\,\mathrm{nm}$ is from experiment [31] and $a_{\mathrm{th}} = 0.2479\,\mathrm{nm}$ is optimized from the first-principles calculation. Points: experimental data from Ref. [9]. The red straight lines at Γ and K are obtained from Eqs. (8) and (10). The two lower panels correspond to the dotted windows in the upper panel. The points are theoretical frequencies obtained by direct calculation. A single graphene band corresponds to two almost degenerate graphite (GI) bands. [32]

Fig. 1-5(b)] , their results show linear dispersion near the Γ and K points for graphene and graphite where slopes α_{K} and α_{Γ} are proportional to the square of electron-phonon coupling at the Γ and K points, respectively. Such a discontinuity of phonon dispersion relation arises because the conduction electron screens lattice vibration, known as the Kohn anomaly effect [29]. In order to understand the mechanism of the electron-phonon interaction in the Kohn anomaly phenomenon, changing the Fermi energy of graphene is useful since part of interband electron-hole excitation can be suppressed by the occupation of electrons in the conduction bands which is called the Pauli blocking effect. The change of the electron-phonon interaction can be measured by gate modulated Raman spectroscopy of the first-order (G band) and the second-order (e.g. G′ and G* bands) Raman spectra.

KA effect on first-order Raman spectra

Gate modulated Raman measurement of the G band shows peak position shift and linewidth change as a function of gate voltage V_g as shown in Fig. 1-6(a) and (b) respectively. This

Fig. 1-6: fig/ch1-KA-G.eps

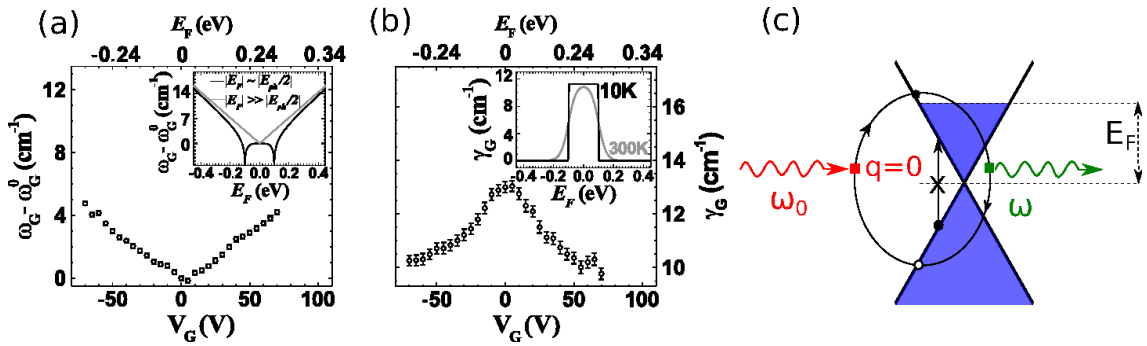

Figure 1-6: The G band (a) peak shift and (b) spectral linewidth as a function of the Fermi energy [33]. (c) The $\mathbf{q} = 0$ Kohn anomaly process. A phonon with frequency ω_0 excites an electron-hole pair. This electron-hole pair then recombines and excites a renormalized phonon with frequency ω [34].

phenomena is attributed to the Kohn anomaly (KA) effect of the G band. There are a number of works reporting the KA effect of the G band [33, 35, 36, 37, 34, 38, 39] and all experimental and calculation results show that the G band peak position (linewidth) increases (decreases) as $|E_F|$ increases. The origins of peak shift and linewidth change are renormalization of phonon frequency by excitation of an electron-hole pair as shown in Fig. 1-6(c). The G phonon, that is excited during the Raman process in Fig. 1-1(b) with frequency ω_0, now excites an electron-hole pair vertically by the electron-phonon interaction. The electron-hole pair is then recombined by emitting a renormalized phonon with frequency ω. The frequency ω is a complex number with its real part gives the renormalized frequency and its imaginary part corresponds to the phonon linewidth. When E_F is nonzero, some electron-hole pairs cannot be excited due to the Pauli exclusion principle. Therefore the decrease of phonon linewidth at a finite E_F which is nothing but the increase of phonon lifetime can be achieve because the phonon is less scattered by electron-hole pairs.

KA effect on second-order Raman spectra

Araujo et al. also measure the gate modulated Raman spectra of the second order Raman spectra, namely the G* and G$'$ [33]. Figure 1-7(a) shows the second order Raman spectra

Fig. 1-7: fig/ch1-KA-Gp.eps

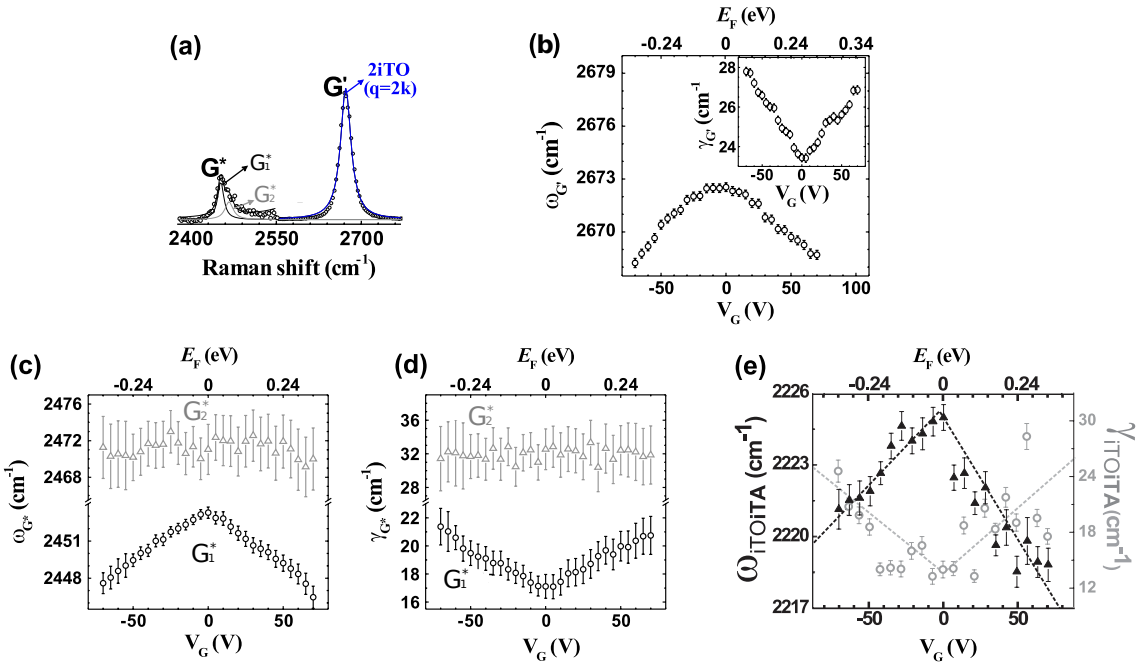

Figure 1-7: (a) The second order Raman spectra including the G′ and G* bands taken from Araujo et al. [33]. (b) The G′ peak shift and spectral linewidth (inset) as a function of the Fermi energy [33]. The G* (c) peak shift and (d) spectral linewidth as a function of the Fermi energy [33]. (e) The iTA + iTO peak shift and spectral linewidth as a function of the Fermi energy [37].

obtained by Araujo et al. The G′ band occurring at ~ 2600 cm^{-1} is fitted by a Lorentzian while the G* band is fitted by two Lorentzians with peaks located at ~ 2450 cm^{-1} labeled by G_1^* and ~ 2470 cm^{-1} labeled by G_2^*. The G′ band peak and linewidth as a function of gate voltage V_g or the Fermi energy E_F are shown in Fig.1-7(b). Compared with the Kohn anomaly (KA) effect of the G band in Fig. 1-6, the KA effect of the G′ band is opposite in terms of both peak position and linewidth. The opposite behavior comes from the non-zero **q** phonons which non vertically excite the electron and hole pair. Because of this non vertical transition with $\mathbf{q} \neq 0$, both intraband and interband electron-hole pairs contribute to the KA effect. One can expect that intraband and interband transition may give opposite KA effect with each other.

The opposite KA effect also exhibit at the G_1^* peak position [Fig. 1-7(c)] and linewidth [Fig. 1-7(d)]. However the G_2^* band does not seem to be affected by the KA effect [Figs. 1-7(c)

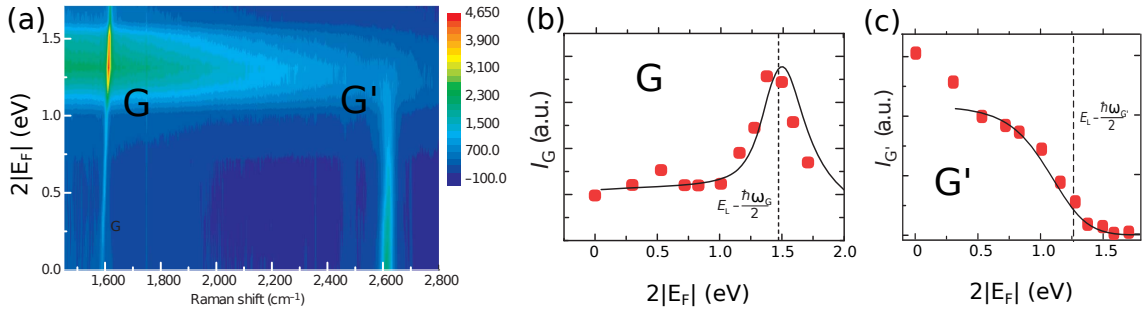

Figure 1-8: (a) Raman intensity of the G and G′ bands as a function of $2E_{\mathrm{F}}$ and the Raman shift. (b) The G band intensity and frequency (inset) as a function of $2E_{\mathrm{F}}$. (c) The G′ band intensity as a function of $2E_{\mathrm{F}}$. [41]

and (d)]. Additionally, a combination phonon mode iTA + iTO occurring at ~ 2220 cm^{-1} measured by Mafra et al. show the same KA effect as that of the G′ and G_1^* [37][Fig. 1-7(e)].

Sasaki et al, discussed the opposite KA effect of the first- and second-order Raman spectra [40]. They consider the competition of interband and intraband electron-hole excitation in phonon perturbation to be of important contribution. However, since the Raman intensity as a function of E_{F} is not calculated, different dispersion of Raman peaks as a function of E_{F} cannot be explained from that theory. In this thesis, we would like to confirm the origin of the KA effect in the second-order process by evaluating the electronic and vibrational properties of graphene. Thus both the first-order and the second-order Raman spectra as a function of E_{F} can be calculated to be compared with the experimental results.

1.3.5 Quantum interference effect in graphene Raman spectra

In the viewpoint of Raman spectroscopy experiment, one can determine only photon states (e.g. energy and polarization) of the incident photon and the states of the scattered photon. Electronic states taking parts on the intermediate state of Raman scattering process are, however, unknown. Quantum physics suggests that for a given initial and a final states of a scattering event, scattering amplitudes through several intermediate states interfere with each other.

Fig. 1-8: fig/ch1-qi.eps

The quantum interference effect on a Raman scattering event can be observed if one can disturb part of the intermediate states so that the Raman intensity changes. Gate modulated Raman spectroscopy allows us to disturb that intermediate state, by changing E_{F} of graphene in which optical transition to the occupied states are not allowed due to the Pauli exclusion principle. As a result, Raman intensity changes by varying E_{F} indicate the observation of the quantum interference effect.

Chen et al. observe the change of the G band and G$'$ band intensity by varying E_{F} as shown in Fig. 1-8 [41]. A 3D plot in Fig. 1-8(a) shows Raman intensity as functions of Raman shift and $2|E_{\mathrm{F}}|$. By taking a particular Raman shift, they plot G and G$'$ Raman intensities as a function of $2|E_{\mathrm{F}}|$ as shown in Fig. 1-8(b) and (c), respectively. Interestingly, the G band intensity shows a peak when $2|E_{\mathrm{F}}| = E_{\mathrm{L}} - \hbar\omega_{\mathrm{G}}/2$ where E_{L} is the laser excitation energy and ω_{G} is the G band frequency. On the other hand, the G$'$ band intensity is monotonically decreasing as a function of $2|E_{\mathrm{F}}|$.

Chen et al. [41] argue that the peak observed at $2|E_{\mathrm{F}}| = E_{\mathrm{L}} - \hbar\omega_{\mathrm{G}}/2$ of the G band intensity originates from opposite phase between two resonant condition, namely the incident resonant condition when electron-hole energy equals E_{L} and the scattered resonant condition when electron-hole energy equals $E_{\mathrm{L}} - \hbar\omega_{\mathrm{G}}$. Thus when we set $2|E_{\mathrm{F}}| = E_{\mathrm{L}} - \hbar\omega_{\mathrm{G}}/2$, the scattered resonant condition is suppressed while the incident resonant condition survives. For the case of the G$'$ band, because electron emits two phonons, no opposite phases between the two resonant conditions are expected. Therefore they obtain monotonically decreasing Raman intensity when number of scattering paths are reduced. However, the theoretical analysis in their work assumes a constant matrix element therefore neglecting the change of the Raman phase due to the electron-phonon matrix elements [41]. Previous theoretical calculations by Jiang et al. [42] and Sasaki et al. [43] show that the electron-phonon matrix elements change sign along electronic equi-energy lines in graphene and therefore can change the Raman phase. A quantitative calculation is, therefore, necessary to understand how the quantum interference effect affects the first- and the second-order Raman intensity.

1.3.6 Breit-Wigner-Fano lineshape observed in carbon systems

Finally we introduce the Breit-Wigner-Fano effects of the G band in graphene. The asymmetric Breit-Wigner-Fano (BWF) spectral lineshape is observed as a result of the interference between continuous with discrete spectra [44]. The BWF lineshape is defined by the following formula

$$\begin{aligned} I_{\mathrm{BWF}}(\omega_{\mathrm{s}}) =& I_0 \frac{(1+s/q_{\mathrm{BWF}})^2}{1+s^2} \\ =& I_0 \left[\frac{1}{q_{\mathrm{BWF}}^2} + \frac{1-1/q_{\mathrm{BWF}}^2}{1+s^2} + \frac{2s/q_{\mathrm{BWF}}}{1+s^2} \right], \end{aligned} \tag{1.4}$$

where $s = (\omega_{\mathrm{s}} - \omega_{\mathrm{G}})/\Gamma$. Here ω_{s}, ω_{G}, $1/q_{\mathrm{BWF}}$, Γ, and I_0 are the Raman shift, the spectral peak position, the asymmetric factor, the spectral width, and the maximum intensity of the BWF spectra, respectively. Equation (1.4) tells us that the three terms in the right hand side consists of a constant continuous spectrum, a discrete Lorentzian spectrum, and an interference effect between both spectra. When $1/q_{\mathrm{BWF}} = 0$, Eq. (1.4) gives a Lorentzian lineshape which represents a discrete phonon spectrum. The interference term gives rise to an asymmetric lineshape because s is a negative (positive) value when $\omega_s < \omega_{\mathrm{G}}$ ($\omega_s > \omega_{\mathrm{G}}$). The asymmetric factor is defined by a dimensionless parameter $1/q_{\mathrm{BWF}}$, mimicking the ratio of amplitude of the discrete spectra to that of the continuous spectra [45].

Historically, graphite intercalation compounds (GICs) are firstly observed in carbon materials to exhibit the BWF of the G band spectra [46]. An example is the G band of C_8Cs (donor atoms of Cs are inserted between graphite layers) as shown in Fig. 1-9(a). The contribution of donated electrons from intercalated atoms (Cs) give the continuous spectra which modify the discrete phonon spectral shapes to become the BWF lineshape. Metallic single wall carbon nanotubes (m-SWNTs) also show the BWF lineshape of the G band [47] as shown in Fig. 1-9(b). This asymmetric G band lineshape of m-SWNTs becomes an important hallmark to distinguish m-SWNT samples from the semiconducting ones (s-SWNT) [48, 49]. In graphene, the BWF lineshape of the G band can be observed by the gate modulated Raman spectroscopy as shown in Fig. 1-4(g) and 1-9(c) by Yoon et al. [28].

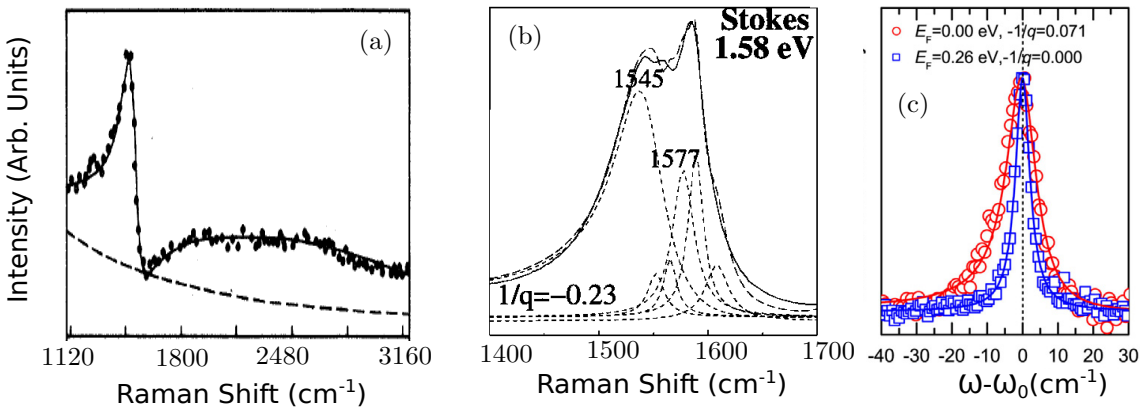

Figure 1-9: Examples of BWF lineshapes found in carbon materials. (a) graphite intercalation compound (C_8Cs) [46], (b) m-SWNTs bundle [47], and (c) graphene with asymmetric factor ($1/q_{\mathrm{BWF}} = -0.071$) when the Fermi energy equals zero [28].

A clue to find the origin of the BWF in graphene-related systems comes from the observation of electronic Raman scattering (ERS) feature in m-SWNTs by Farhat et al. [50]. The ERS spectra were observed exclusively in m-SWNTs but not in s-SWNTs. Although the ERS spectra have well-defined peaks, their features are very broad with linewidth about 100 cm^{-1}. That might be a reason why the ERS spectra are overlooked especially in bundled or defective SWNTs. This ERS spectra in m-SWNTs can be distinguished from conventional phonon spectra based on the E_{L} dependence of the Raman spectra. Scattered photon energy (E_{s}) of the ERS is always resonant to the excitonic energy E_{ii} of m-SWNTs while E_{s} of the phonon spectra changes by varying E_{L} as $E_{\mathrm{s}} = E_{\mathrm{L}} - \omega_{\mathrm{G}}$, where $\omega_{\mathrm{G}} = 1600$ cm^{-1} is the G band Raman shift. The ERS spectra originate from the electron-electron interaction between photoexcited carriers and electrons near the linear energy band of m-SWNTs [51]. Existence of energy gap in s-SWNTs prevents the ERS mechanism therefore there is no ERS spectrum observed in s-SWNTs. Interference between the ERS spectra with the G phonon spectra give rise to the asymmetric BWF lineshape of the G band. In this thesis, calculation of the ERS spectra of graphene will be performed to explain systematic changes of $1/q_{\mathrm{BWF}}$ as a function of E_{F} as shown in Fig. 1-4(g).

Fig. 1-9: fig/ch1-bwf-gic.eps

1.3.7 Summary of Background

There are three phenomena arising from the gate modulated Raman spectroscopy that are discussing in this thesis, (1) the Kohn anomaly effect, (2) the quantum interference effect, (3) and the Breit-Wigner-Fano lineshape of Raman spectra. Motivations of this thesis which are based on the three phenomena will be summarized in the following paragraphs.

In Raman spectroscopy of solids, frequency of lattice vibration (phonon) can be probed from the difference of incident to scattered light frequencies. The frequency of an excited phonon during the Raman process corresponds to a peak in the Raman spectra. When a gate voltage is applied to graphene, the peak position and linewidth of Raman spectra change because the Fermi energy (E_{F}) of graphene is varied. This phenomenon is known as the Kohn anomaly (KA) effect, i.e. a modification of phonon frequency by means of an electron-hole pair excitation via the electron-phonon interaction [29] (see Sec. 1.3.4). The KA effects appear in the first-order (G band) and second-order (e.g. G$'$ and G* bands) Raman spectra. The KA effect for the first-order Raman spectra show increasing (decreasing) of peak frequency (spectral linewidth) when $|E_{\mathrm{F}}|$ is increased. Theoretical works agree well with the Raman measurements of the E_{F} dependence of the first-order Raman spectra [52, 32, 53]. However, for the second-order Raman spectra, in particular the G$'$ band, Araujo et al. show opposite results for the G$'$ band spectra as a function of E_{F} compared to the G band spectra in both peak position and spectral linewidth [33]. In this thesis, we present calculated results of the second-order Raman spectra as a function of E_{F} from which we understand the origin of the opposite KA effects of the first- and second-order Raman spectra.

In gate modulated Raman spectroscopy, the quantum interference effect of Raman spectra can be observed as the change of Raman intensity as a function of E_{F} (see Sec. 1.3.5). When E_{F} is non-zero, some electronic states cannot contribute to Raman scattering process due to the Pauli exclusion principle. Even with the reduced number of photo-excited electrons, the G band intensity surprisingly increases when $2|E_{\mathrm{F}}|$ is very close to the laser excitation energy as reported by Chen et al [41]. The theoretical analysis by Chen et al. only consider the phase of Raman spectra based on the resonant condition and set the electron-phonon

matrix element as a constant. However, the electron-phonon matrix elements do change the sign for different electron or phonon states, therefore a quantitative calculation of Raman intensity is needed to understand how quantum interference effect affects the first- and the second-order Raman intensity.

Finally, we discuss the asymmetric Breit-Wigner-Fano (BWF) lineshape found in the G band of graphene (see Sec. 1.3.6). For long years, the G band of graphene is fitted to a symmetric Lorentzian lineshape. Recently, the BWF asymmetry has been observed by Yoon et al. [28] in graphene with the BWF asymmetric factor systematically decreases by increasing $|E_{\rm F}|$. Historically the BWF lineshape is observed in the Raman spectra of graphite interacalation compounds (GICs) [46] and metallic single wall carbon nanotubes (m-SWNTs) [47]. Those BWF lineshapes probe interference effect between the continuous spectra with discrete spectra [44]. The appearance of the BWF lineshape in the G band of graphene indicates a common origin of the BWF lineshape of the graphite-related systems (i.e. GICs, m-SWNTS, and graphene) that arise due to the presence of the Dirac cone or the linear energy band structure. These results give a clue that the BWF asymmetric factor strongly depends on the electronic states near the Dirac point.

In order to quantitatively study all those phenomena, we calculate the $E_{\rm F}$ dependence of the first- and the second-order Raman spectra. The calculated spectral quantities are the Raman peak shift, spectral linewidth, and the Raman intensity as a function of $E_{\rm F}$ for both the first- and the second-order Raman spectra. We calculate the BWF asymmetric factor only for the first-order Raman and not for the second-order ones for simplicity. The KA correction including both shift of phonon frequency and phonon linewidth is modeled based on the second-order perturbation theory. The KA of the first-order Raman spectra which is relevant to the $\mathbf{q} = 0$ phonon is calculated so as to reproduce the existing theoretical and experimental results and to compare with the KA of $\mathbf{q} \neq 0$ phonon. For the case of the second-order Raman spectra, we focus on the intervalley scatterings which give three prominent peaks, namely, the G$'$, G*, and iTA + iTO bands (see Sec. 4.1). Finally the $E_{\rm F}$ dependence of those Raman spectra are analyzed and compared to the experimental results.

Chapter 2

Electronic, Vibrational, and Optical Properties of Graphene

Calculation of Raman intensity requires knowledge of electronic, vibrational, and optical properties of the material of interest. In Sec. 2.1, the electronic properties of graphene are reviewed based on the tight binding method. We first define the geometry of graphene and considering the nearest neighbor interaction to obtain electronic structure of graphene from the simple tight binding (STB) method. Although STB framework explains electron energy dispersion near the Fermi level very well, it fails at far from the Fermi level. Thus we should incorporate more interaction from extended neighbors measured from atomic site of interest within the extended tight binding (ETB) method. In Sec. 2.2, we derive the phonon dispersion relations of graphene within force constant model. We assume interatomic potential to be of harmonic potential and solve equation of motion for atoms based on the harmonic oscillator equation. The force constant is constructed from accounting the contribution up to the 20-th nearest neighbor. The electron-photon, and electron-phonon interactions will be discussed in Sec.2.3-2.4 based on the knowledge of electron wave function from the ETB method.

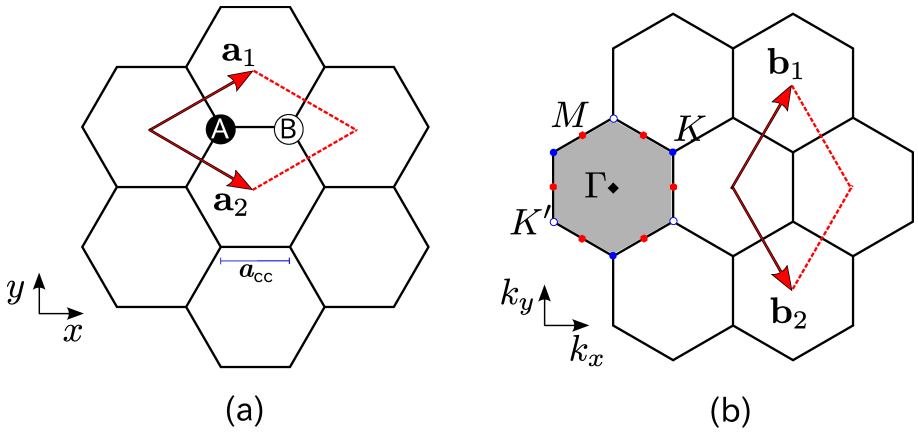

Figure 2-1: (a) The unit cell of graphene which consists of two atomic sites A and B. $\mathbf{a}_1$, and $\mathbf{a}_2$ are the unit vectors and a_{CC} is the carbon-carbon distance. (b) Brillouin zone of graphene. The Γ, K, K$'$, and M points indicated with a closed diamond, closed circles, opened circles, and closed hexagons, respectively, are the high symmetry points. Reciprocal lattice vectors is denoted by $\mathbf{b}_1$ and $\mathbf{b}_2$.

2.1 Electronic Properties of Graphene

2.1.1 Graphene unit cell and Brillouin zone

Graphene is a single atomic layer of two dimensional (2D) hexagonal carbon lattice whose structure is considered the basic building block of sp^2 carbon allotropes. The carbon-carbon atoms of graphene are bound by covalent bondings (σ-bonds) to form the graphene layer. Several layers of graphene sheets are stacked together by the van der Waals force to form three dimensional (3D) graphite.

Figure 2-1 gives the unit cell and Brillouin zone of graphene. Each unit cell consist of two atoms, labeled by A and B atomic sites as shown in Fig. 2-1(a). Unit vectors $\mathbf{a}_1$ and $\mathbf{a}_2$ are given by

$$\mathbf{a}_1 = a\left(\frac{\sqrt{3}}{2}, \frac{1}{2}\right), \quad \mathbf{a}_2 = a\left(\frac{\sqrt{3}}{2}, -\frac{1}{2}\right), \tag{2.1}$$

where $a = \sqrt{3}a_{CC}$ is the lattice constant for the graphene unit cell and $a_{CC} = 0.142$nm is the nearest carbon-carbon distance. In Fig. 2-1(b), reciprocal lattice vectors $\mathbf{b}_1$ and $\mathbf{b}_2$ are

Fig. 2-1: fig/grapbz.eps

obtained from the relations:

$$\mathbf{a}_i \mathbf{b}_j = 2\pi\delta_{ij}, \tag{2.2}$$

where δ_{ij} is the Kronecker delta ($\delta_{ij} = 1$ for $i = j$, $\delta_{ij} = 0$ otherwise) and $\mathbf{b}_1$ and $\mathbf{b}_2$ are given by

$$\mathbf{b}_1 = \frac{2\pi}{a}\left(\frac{1}{\sqrt{3}}, 1\right), \quad \mathbf{b}_2 = \frac{2\pi}{a}\left(\frac{1}{\sqrt{3}}, -1\right). \tag{2.3}$$

The first Brillouin zone is the rhombic area whose sides consist of $\mathbf{b}_1$ and $\mathbf{b}_2$ as shown in Fig. 2-1(b). That rhombic area is equivalent to the shaded hexagon that we will adopt as the Brillouin zone. The high symmetry points are defined at hexagon center Γ, the center of an edge M, and the hexagonal corners K and K$'$ of the Brillouin zone which are commonly used in the analysis of electronic structure of Graphene (Sec. 2.1.2).

2.1.2 Electronic structure of graphene

The electronic dispersion relations of graphene are reviewed within the tight-binding method. Let us start from a simple tight-binding (STB) method. The STB method (or linear combination of atomic orbitals, LCAO) is used to calculate the electronic energy dispersion relation of a crystal, that is the energy E as a function of wavevector $\mathbf{k}$. In the tight binding approximation of a crystal, the eigenfunctions of electrons are made up by the Bloch functions corresponding to atomic orbitals. Thus the problem of finding an eigenfunction is reduced to finding the coefficients for the Bloch functions consisting of atomic orbitals.

Per one unit cell of graphene, we have 5 atomic orbitals (1s, 2s, $2p_x$, $2p_y$, and $2p_z$) from each A and B atomic sites (Fig. 2-1(a)), which give 10 atomic orbitals all together in the unit cell. Electrons in 2s, $2p_x$, and $2p_y$ orbitals construct the σ bonding while $2p_z$ orbital gives the π bonding. Hereafter, in this thesis, we consider only the π electron since its energy is very close to the Fermi energy and it dominantly contributes to electronic transport and optical properties for visible light [54].

The electron wavefunction for a band index b is given by given by

$$\psi^b(\mathbf{k},\mathbf{r}) = \sum_{s=\mathrm{A,B}} C_s^b(\mathbf{k})\phi_s(\mathbf{k},\mathbf{r}), \quad (b=1,2). \tag{2.4}$$

Here $b = \mathrm{v,c}$ is index of the electronic energy band for π bonding (valence band) and π^* anti-bonding (conduction band), respectively and s in the sum is taken over the A and B atomic sites. The $C_s^b(\mathbf{k})$ are coefficients of the Bloch functions $\phi_s(\mathbf{k},\mathbf{r})$ that are needed to be solved. The Bloch wavefunctions are given by linear combination of atomic orbital $\varphi(\mathbf{r}-\mathbf{R}_{js})$ at the j–th crystal site weighted by a phase factor $e^{i\mathbf{k}\cdot\mathbf{R}_{js}}$, given explicitly as:

$$\phi_s(\mathbf{k},\mathbf{r}) = \frac{1}{\sqrt{N}}\sum_{j}^{N} e^{i\mathbf{k}\cdot\mathbf{R}_{js}}\varphi(\mathbf{r}-\mathbf{R}_{js}), \quad (s=\mathrm{A,B})\,. \tag{2.5}$$

The Hamiltonian of graphene can be written as:

$$H = \frac{\mathbf{p}^2}{2m} + \sum_{js} V(\mathbf{r}-\mathbf{R}_{js}). \tag{2.6}$$

In the right hand side of Eq. (2.6), the first term is the kinetic energy while the second term is the periodic potential of solids. We solve the energy for eigen state b by variational method through minimizing expectation value

$$E^b = \frac{\langle\psi^b|H|\psi^b\rangle}{\langle\psi^b|\psi^b\rangle}, \quad (b=\mathrm{v,c}), \tag{2.7}$$

as a function of the wavefunction coefficients. The variational condition for finding the minimum is

$$\frac{\partial E^b}{\partial C_s^{b*}} = 0, \quad (b=\mathrm{v,c}). \tag{2.8}$$

The resulting equations for $C_s^b(\mathbf{k})$ after minimization Eq. (2.8) are

$$\sum_{s'} H_{\mathrm{ss'}} C_{s'}^b(\mathbf{k}) = E^b \sum_{s'} S_{\mathrm{ss'}} C_{s'}^b(\mathbf{k}) \quad (s,s'=\mathrm{A,B}), \tag{2.9}$$

where the matrix elements $H_{ss'} = \langle\phi_s|H|\phi_{s'}\rangle$ and $S_{ss'} = \langle\phi_s|\phi_{s'}\rangle$. We may write explicitly the matrix elements in Eq. (2.9) as

$$H(\mathbf{k}) = \begin{pmatrix} H_{\mathrm{AA}}(\mathbf{k}) & H_{\mathrm{AB}}(\mathbf{k}) \\ H_{\mathrm{BA}}(\mathbf{k}) & H_{\mathrm{BB}}(\mathbf{k}) \end{pmatrix}, \quad \text{and} \quad S(\mathbf{k}) = \begin{pmatrix} S_{\mathrm{AA}}(\mathbf{k}) & S_{\mathrm{AB}}(\mathbf{k}) \\ S_{\mathrm{BA}}(\mathbf{k}) & S_{\mathrm{BB}}(\mathbf{k}) \end{pmatrix}. \tag{2.10}$$

Because we expect to obtain E^b as a real quantity, $H(\mathbf{k})$ and $S(\mathbf{k})$ should form the Hermitian matrices, we require

$$H_{\mathrm{BA}}(\mathbf{k}) = H^*_{\mathrm{AB}}(\mathbf{k}), \quad \text{and} \quad S_{\mathrm{BA}}(\mathbf{k}) = S^*_{\mathrm{AB}}(\mathbf{k}). \tag{2.11}$$

Now we evaluate each component of matrix elements. By using Eq. (2.5),

$$\begin{aligned} H_{\mathrm{AA}}(\mathbf{k}) &= \frac{1}{N}\sum_{j,j'} e^{i\mathbf{k}\cdot(\mathbf{R}_{j\mathrm{A}}-\mathbf{R}_{j'\mathrm{A}})}\langle\varphi(\mathbf{r}-\mathbf{R}_{j'\mathrm{A}})|H|\varphi(\mathbf{r}-\mathbf{R}_{j\mathrm{A}})\rangle \\ &= \epsilon_{2\mathrm{p}} + \mathcal{O}(\mathbf{R}_{j'\mathrm{A}} \geq \mathbf{R}_{j\mathrm{A}} \pm \mathbf{a}_i). \end{aligned} \tag{2.12}$$

In STB method we neglect hopping of electron from $\mathbf{R}_{j\mathrm{A}}$ to $\mathbf{R}_{j'\mathrm{A}} \geq \mathbf{R}_{j\mathrm{A}} \pm \mathbf{a}_i$, with $i = 1, 2$, for simplicity. Longer distance hopping will not be considered in the STB method but will be taken into account in the ETB method in Sec. 2.1.3. Orbital energy of $2p$ level is obtained from $\epsilon_{2\mathrm{p}} = \dfrac{1}{N}\displaystyle\sum_j \langle\varphi(\mathbf{r}-\mathbf{R}_{j\mathrm{A}})|H|\varphi(\mathbf{r}-\mathbf{R}_{j\mathrm{A}})\rangle$. In the same manner, H_{BB} gives the same $\epsilon_{2\mathrm{p}}$. Since the difference of H_{AA} and H_{BB} is more important than their values themselves, we may set $H_{\mathrm{AA}} = H_{\mathrm{BB}} = 0$ by changing the energy threshold.

For $H_{\mathrm{AB}}(\mathbf{k})$, the largest contribution to the matrix element arise when atoms A and B are nearest neighbors with distance $\mathbf{R}_i$, $(i = 1, \ldots, 3)$ for the first nearest neighbors (Fig. 2-2). Thus we only consider $\mathbf{R}_{j'\mathrm{B}} = \mathbf{R}_{j\mathrm{A}} + \mathbf{R}_i$ in the summation over j' and neglecting the more

Fig. 2-2: fig/ch2-ab.eps

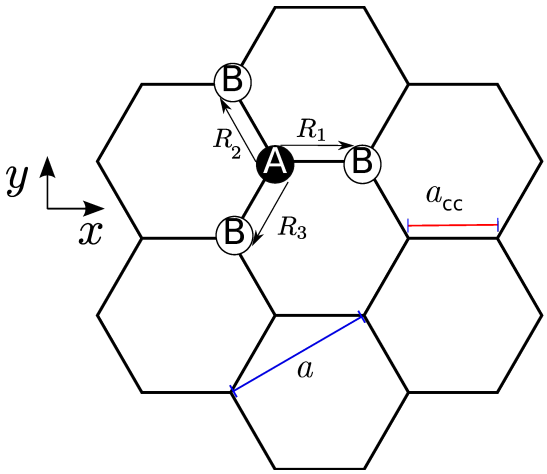

Figure 2-2: A and B atomic site of a graphene unit cell. A atom lies at center $(0,0)$ and three nearest neighbor B atoms are indicated by $R_1 = a\left(\frac{1}{\sqrt{3}}, 0\right)$, $R_2 = a\left(-\frac{1}{2\sqrt{3}}, \frac{1}{2}\right)$, and $R_3 = a\left(-\frac{1}{2\sqrt{3}}, -\frac{1}{2}\right)$ where $a = 2.46$ Å.

distant term to obtain

$$\begin{aligned} H_{\mathrm{AB}}(\mathbf{k}) &= \frac{1}{N}\sum_j e^{i\mathbf{k}\cdot\mathbf{R}_i}\langle\varphi(\mathbf{r}-\mathbf{R}_{j\mathrm{A}})|H|\varphi(\mathbf{r}-\mathbf{R}_{j\mathrm{A}}-\mathbf{R}_i), \quad i=1,\ldots 3 \\ &\equiv tf(\mathbf{k}) \end{aligned} \tag{2.13}$$

where $t = -3.033$ eV [55] is the hopping integral $\langle\varphi(\mathbf{r}-\mathbf{R})|H|\varphi(\mathbf{r}-\mathbf{R}-\mathbf{R}_i)\rangle$ which are the same for three nearest neighbor B atoms in Fig. 2-2. In general, the nearest neighbor hopping integral should have negative value so that total energy of a solid becomes smaller than total energy of individual atoms which make sure that the solid is stable. $f(\mathbf{k})$ is a function of the sum of the phase factor $f(\mathbf{k}) = \sum_{i=1}^{3} e^{i\mathbf{k}.\mathbf{R}_i}$. By using x, y coordinates as shown in Fig. 2-2, $f(\mathbf{k})$ is given by

$$f(\mathbf{k}) = e^{ik_x a/\sqrt{3}} + 2e^{-ik_x a/2\sqrt{3}}\cos\left(\frac{k_y a}{2}\right). \tag{2.14}$$

Using Eq. (2.5), the overlap matrix elements $S_{\mathrm{AA}} = S_{\mathrm{BB}} = 1$, and $S_{\mathrm{AB}} = sf(\mathbf{k}) = S^*_{\mathrm{BA}}$.

Here the overlap parameter s is defined by

$$s = \langle \varphi(\mathbf{r} - \mathbf{R}) | \varphi(\mathbf{r} - \mathbf{R} - \mathbf{R}_i) \rangle. \tag{2.15}$$

In this work, we take $s = 0.129$ [55] in order to reproduce the result from first principle calculation of graphite energy bands. Combining Eqs. (2.10)-(2.15), Eq.(2.9) becomes,

$$\begin{pmatrix} -E^b(\mathbf{k}) & f(\mathbf{k})\left\{t - sE^b(\mathbf{k})\right\} \\ f^*(\mathbf{k})\left\{t - sE^b(\mathbf{k})\right\} & -E^b(\mathbf{k}) \end{pmatrix} \begin{pmatrix} C_A^b(\mathbf{k}) \\ C_B^b(\mathbf{k}) \end{pmatrix} = \mathbf{0}\ , \quad (b = \mathrm{c},\ \mathrm{v}). \tag{2.16}$$

There are two solutions for Eq. (2.16) given by:

$$E^b(\mathbf{k}) = \frac{\pm t w(\mathbf{k})}{1 \pm s w(\mathbf{k})} \tag{2.17}$$

where $w(\mathbf{k}) = \sqrt{f(\mathbf{k}) f^*(\mathbf{k})}$ + $(-)$ sign denotes the valence (conduction) band, by noting that t has a negative value. The electronic structure of π electron now can be obtained by mapping $E^b(\mathbf{k})$ over first Brillouin zone in Fig. 2-1(b). In Fig. 2-3(a), the 3D picture of $E^b(\mathbf{k})$ in the first Brillouin zone is plotted. E^{v} and E^{c} bands touch each other at $\mathbf{k} = \mathrm{K}$ and $\mathbf{k} = \mathrm{K}'$ points.

For a small electron wavevector $\mathbf{k}$, which is measured from the K points, we expand Eq. (2.17) around K and K′ as $f(\mathbf{K}+\mathbf{k})$ and $f(\mathbf{K}'+\mathbf{k})$. The K and K′ points have coordinates $\mathbf{K} = (0, -4\pi/(3a))$ and $\mathbf{K}' = (0, 4\pi/(3a))$. With $\mathbf{k} = (k_x, k_y)$ we obtain

$$f(\mathbf{K} + \mathbf{k}) = \frac{\sqrt{3}a}{2}\left(ik_x + k_y\right), \quad \text{and} \quad f(\mathbf{K}' + \mathbf{k}) = \frac{\sqrt{3}a}{2}\left(ik_x - k_y\right). \tag{2.18}$$

Substituting Eqs. (2.18) into Eq. (2.17), we get an approximation for the electron energy dispersion relations close to the K points. It turns out that in the linear order approximation we get the same energy dispersion relation around K and K′ points,

$$E^b(\mathbf{k} + \mathbf{K}) = E^b(\mathbf{k} + \mathbf{K}') = \pm\frac{\sqrt{3}at}{2}\sqrt{k_x^2 + k_y^2}. \tag{2.19}$$

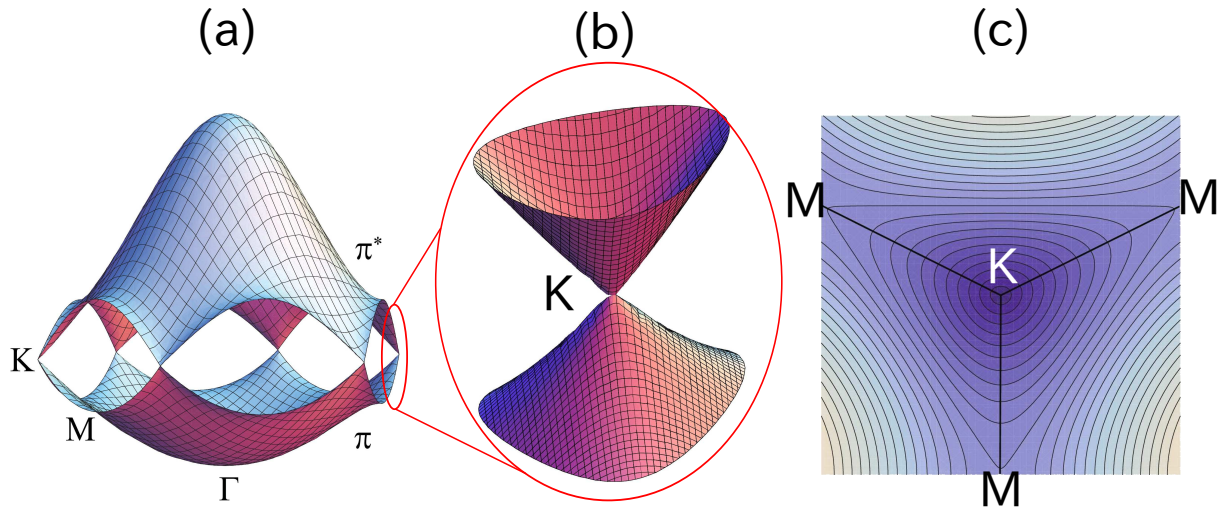

Figure 2-3: (a) π electron energy dispersion relation in the first Brillouin zone from Eq. (2.17). (b) Dirac-cone around K point (Eq. (2.18)). (c) Equi–energy contour of $E_g(\mathbf{k})$ which shows circle near K point and deform to triangle, known as trigonal warping effect [56], if we go further to M point. Separation between two equi-energy lines are 0.7 eV.

Here the "+(–)" sign corresponds to valence (conduction) band. In Fig. 2-3(b), we plot the $E^b(\mathbf{k})$ for Eq. (2.19) which has a cone shape, known as the Dirac cone. In Fig. 2-3(c) we plot equi–energy contours which are almost circles around the K and K points. The equi–energy circles deform to triangles, when going to the higher electron energies. This is known as the trigonal warping effect of graphene energy dispersion [56]. The equi–energy contour connecting three nearest M points is a triangle as shown in Fig. 2-3(c). Optical transitions occur between the π and π^* energy bands and from Fig. 2-3(a) it is clear that low energy optical spectroscopy in the region of visible light mainly probes electrons around K points between the π and π^* bands.

We now calculate the wavefunction coefficients for electrons for A and B atoms, $C^b_{\rm A}$ and $C^b_{\rm B}$, respectively. The relation between $C^b_{\rm A}$ and $C^b_{\rm B}$ is obtained from Eq. (2.16) and is given

Fig. 2-3: fig/ch2-triek.eps

by

$$C^b_{\rm A}(\mathbf{k}) = C^b_{\rm B}(\mathbf{k})\frac{f(\mathbf{k})\left\{t - sE^b(\mathbf{k})\right\}}{E^b(\mathbf{k})}, \tag{2.20}$$

$$C^b_{\rm A}(\mathbf{k}) = C^b_{\rm B}(\mathbf{k})\frac{E^b(\mathbf{k})}{f^*(\mathbf{k})\left\{t - sE^b(\mathbf{k})\right\}} \tag{2.21}$$

We can simplify Eqs. (2.20) and (2.21) to get:

$$\frac{C^b_{\rm A}(\mathbf{k})}{C^b_{\rm B}(\mathbf{k})} = \pm\sqrt{\frac{f(\mathbf{k})}{f^*(\mathbf{k})}} \equiv \pm\frac{f(\mathbf{k})}{w(\mathbf{k})} \tag{2.22}$$

Signs + and − are for the valence and conduction bands, respectively. We can then obtain four eigenvectors $C^b_s(\mathbf{k})$ for $b = \mathrm{v},\ \mathrm{c}$ and $s = \mathrm{A}, \mathrm{B}$ as

$$\begin{aligned}
C^{\rm v}_{\rm A}(\mathbf{k}) &= \exp(i\phi_{\rm v})\sqrt{\frac{1}{2\left\{1 + sw(\mathbf{k})\right\}}},\\
C^{\rm c}_{\rm A}(\mathbf{k}) &= \exp(i\phi_{\rm c})\sqrt{\frac{1}{2\left\{1 - sw(\mathbf{k})\right\}}},\\
C^{\rm v}_{\rm B}(\mathbf{k}) &= \exp\left[i(\phi_{\rm v} + \theta(f^*)\right]\sqrt{\frac{1}{2\left\{1 + sw(\mathbf{k})\right\}}},\\
C^{\rm c}_{\rm B}(\mathbf{k}) &= -\exp\left[i(\phi_{\rm c} + \theta(f^*)\right]\sqrt{\frac{1}{2\left\{1 - sw(\mathbf{k})\right\}}}.
\end{aligned} \tag{2.23}$$

where $\tan\theta(f^*) = \mathrm{Im}(f^*)/\mathrm{Re}(f^*)$. Note that the phase factors $\phi_{\rm v}$ or $\phi_{\rm c}$ for Eq. (2.21) can be chosen arbitrarily as long as the phase difference between the A and B atoms is preserved.

2.1.3 Extended tight binding method

Extended tight binding (ETB) method improves the STB method by adding long range electronic hopping and optimizing the lattice constant of graphene. Historically the ETB method was developed by Samsonidze [58] to improve the electronic structure of SWNTs so as to match the experimental results of SWNTs transition energy [59, 60]. In the case of

Fig. 2-4: fig/ch2-stb-etb.eps

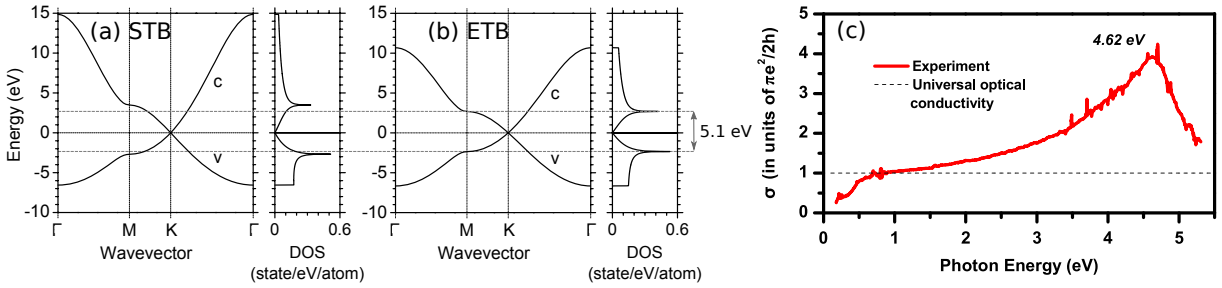

Figure 2-4: Graphene energy dispersion relations and density of states calculated from (a) simple tight binding method (b) extended tight binding method. Indices v and c indicate valence and conduction band respectively. (c) Optical conductivity of graphene measured by Mak et al., [57].

graphene electronic structure, the use of the ETB method improves the energy separation between the valence and conduction bands at the M point $E_{\mathrm{M}}^{\mathrm{cv}}$ as shown in Fig. 2-4. The STB calculation show that $E_{\mathrm{M}}^{\mathrm{cv}} \approx 6\,\mathrm{eV}$ in Fig. 2-4(a), however the measurement of optical conductivity by Mak et al., show that $E_{\mathrm{M}}^{\mathrm{cv}}$ should be about 4.62 eV in Fig. 2-4(c) [57]. The $E_{\mathrm{M}}^{\mathrm{cv}}$ measured in the experiment is shown as the maximum optical conductivity because of the Van Hove singularity in the density of state of graphene originating from the saddle point energy bands at the M point. Using the ETB calculation, we can get $E_{\mathrm{M}}^{\mathrm{cv}} = 5.1\,\mathrm{eV}$. The discrepancy between the ETB result and experimental measurement of $E_{\mathrm{M}}^{\mathrm{cv}}$ is about 0.5 eV which comes from excitonic effect [61].

In the ETB method, matrix elements of $H(\mathbf{k})$ and $S(\mathbf{k})$ in Eq. (2.10) are now given by:

$$H(\mathbf{k}) = \begin{pmatrix} \sum_{j}^{C} t(\mathbf{R}_{j1}^{\mathrm{AA}}) f_j^{\mathrm{AA}}(\mathbf{k}) & \sum_{j}^{C} t(\mathbf{R}_{j1}^{\mathrm{AB}}) f_j^{\mathrm{AB}}(\mathbf{k}) \\ \sum_{j}^{C} t(\mathbf{R}_{j1}^{\mathrm{BA}}) f_j^{*\mathrm{BA}}(\mathbf{k}) & \sum_{j}^{C} t(\mathbf{R}_{j1}^{\mathrm{BB}}) f_j^{\mathrm{BB}}(\mathbf{k}) \end{pmatrix}, \tag{2.24}$$

$$S(\mathbf{k}) = \begin{pmatrix} \sum_{j}^{C} s(\mathbf{R}_{j1}^{\mathrm{AA}}) f_j^{\mathrm{AA}}(\mathbf{k}) & \sum_{j}^{C} s(\mathbf{R}_{j1}^{\mathrm{AB}}) f_j^{\mathrm{AB}}(\mathbf{k}) \\ \sum_{j}^{C} s(\mathbf{R}_{j1}^{\mathrm{BA}}) f_j^{*\mathrm{BA}}(\mathbf{k}) & \sum_{j}^{C} s(\mathbf{R}_{j1}^{\mathrm{BB}}) f_j^{\mathrm{BB}}(\mathbf{k}) \end{pmatrix}, \tag{2.25}$$

where $\mathbf{R}_{jn}^{ss'} = \mathbf{R}_{js'}^{n} - \mathbf{R}_{0s}$ is distance between a center atom located at $\mathbf{R}_{0s}$ to a n–th atom

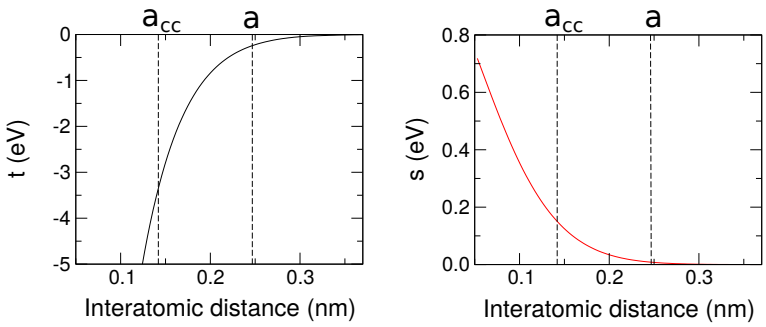

Figure 2-5: (a) Hopping integral t and (b) overlap integral s as a function of interatomic distance. Carbon-carbon distance $a_{\rm cc} = 0.142\,$nm and lattice constant $a = 0.246\,$nm are indicated in the figures.

of j–th nearest neighbor at $\mathbf{R}^n_{js'}$. C–th nearest neighbor is defined by the outer most atom position inside a cutoff range, here we set $R_C = 7a_0$ with $a_0 = 0.052917721$ nm is the Bohr radius. Now we change definition of the hopping integral t in Eq. (2.13), overlap integral s in Eq. (2.15), and the tight binding phase factor f in Eq. (2.14) to become:

$$t(\mathbf{R}^{ss'}_{jn}) = \langle\varphi(\mathbf{r}-\mathbf{R}^n_{js'})|H|\varphi(\mathbf{r}-\mathbf{R}_{0s}\rangle \quad , \tag{2.26}$$

$$s(\mathbf{R}^{ss'}_{jn}) = \langle\varphi(\mathbf{r}-\mathbf{R}^n_{js'})|\varphi(\mathbf{r}-\mathbf{R}_{0s}\rangle \quad , \tag{2.27}$$

$$f^{ss'}_j(\mathbf{k}) = \sum_n e^{i\mathbf{k}\cdot\mathbf{R}^{ss'}_{nj}}. \tag{2.28}$$

Functions $t(\mathbf{R})$ and $s(\mathbf{R})$ are parameterized from density-functional theory employing the local density approximation (LDA) and using a local orbital basis set [62]. In Fig. 2-5, the ETB transfer and overlap integrals at the first nearest neighbor $t(a_{\rm cc}) = -3.351$ eV and $s(a_{\rm cc}) = 0.150$, with $a_{cc} = 0.142\,$nm, differ slightly from the STB integrals $t = -3.033$ eV and $s = 0.129$ introduced in Sec. 2.1.2. At the second nearest neighbor with a distance $a = \sqrt{3}a_{\rm cc} = 0.246\,$nm the ETB transfer and overlap integrals $t(a) = -0.248$ eV and $s(a) = 0.008$ decrease significantly from $t(a_{\rm cc})$ and $s(a_{\rm cc})$, respectively.

Fig. 2-5: fig/ch2-st.eps

2.2 Vibrational Properties of Graphene

In this section we shall derive the phonon dispersion of graphene. Interatomic potential of graphene can be regarded as a harmonic potential and we shall solve atomic motion similar to the harmonic oscillator. We utilize the force-constant model and solve the dynamical matrix to obtain phonon dispersion relations of graphene. The force-constant parameters are taken by considering up to the 20-th nearest neighbor with interatomic potential fitted to the density functional theory (DFT) results [63].

Let us consider a carbon atom of mass m under influence of harmonic potential, the equation of motion is given by:

$$m\frac{d^2u^{\nu}_{j's'\alpha'}}{dt^2} = \sum_{j=1}^{N}\sum_{s=1}^{2}\sum_{\alpha=1}^{3}\mathcal{K}^{js\alpha}_{j's'\alpha'}\left(u^{\nu}_{js\alpha} - u^{\nu}_{j's'\alpha'}\right), \tag{2.29}$$

where $\mathbf{u}^{\nu}_{js}$ is displacement vector of carbon atom from equilibrium position $\mathbf{R}_{js}$ with number of unit cell $j = 1, \ldots, N$, atomic site $s = 1, 2$ labels either A or B atom, $\alpha = x, y, z$ is the Cartesian coordinates, ν is the phonon mode and $\mathcal{K}^{js\alpha}_{j's'\alpha'}$ is the interatomic force constant. The Fourier transform of $\mathbf{u}^{\nu}_{js}$ gives normal mode of phonon vibration $\boldsymbol{\varepsilon}^{\nu}_{s}(\mathbf{q})$ as follows:

$$\mathbf{u}^{\nu}_{js} = \sum_{\mathbf{q}} A^{\nu}(\mathbf{q})\boldsymbol{\varepsilon}^{\nu}_{s}(\mathbf{q})e^{i(\mathbf{q}\cdot\mathbf{R}_{js} - \omega^{\nu}(\mathbf{q})t)}\ , \tag{2.30}$$

where $A^{\nu}(\mathbf{q})$ is amplitude of the ν phonon, $\omega^{\nu}(\mathbf{q})$ is the ν phonon frequency, and $\mathbf{q}$ is the phonon wave vector. $\boldsymbol{\varepsilon}^{\nu}_{s}(\mathbf{q})$ can be obtained by the group theory analysis even without solving Eq. (2.29) [64]. Two atoms in a unit cell of graphene gives 3 acoustic modes, namely longitudinal acoustic (LA), in-plane tangential acoustic (iTA), out of plane tangential acoustic (oTA) modes and 3 optic modes, namely longitudinal optic (LO), in-plane tangential optic (iTO), out of plane tangential optic (oTO). Figure 2-6 shows $\boldsymbol{\varepsilon}^{\nu}_{s}(\mathbf{q})$ for six phonon modes (LA, iTA, oTA, LO, iTO, and oTO) at $\mathbf{q} = \Gamma$ [Figs. 2-6(a)-(f)] and at $\mathbf{q} = \mathrm{K}$ [Figs. 2-6(g)-(l)].

The normal mode $\boldsymbol{\varepsilon}_s^{\nu}(\mathbf{q})$ obeys the orthogonality condition:

$$\sum_{s=1}^{2}\sum_{\alpha}\varepsilon_{s\alpha}^{\nu'*}(\mathbf{q})\varepsilon_{s\alpha}^{\nu}(\mathbf{q}) = \delta_{\nu'\nu} \ , \tag{2.31}$$

where $\delta_{\nu'\nu}$ is the Kronecker delta which gives unity for $\nu' = \nu$ and zero for otherwise. Additional condition for $\boldsymbol{\varepsilon}_s^{\nu}(\mathbf{q})$ is

$$\boldsymbol{\varepsilon}_s^{\nu*}(\mathbf{q}) = \boldsymbol{\varepsilon}_s^{\nu}(-\mathbf{q}) \tag{2.32}$$

so as to ensure that $\mathbf{u}_{js}^{\nu}$ is real when $t = 0$.

Substituting Eq. (2.30) to Eq. (2.29) yields:

$$\begin{aligned} m\sum_{\mathbf{q}}\left(\omega^{\nu}(\mathbf{q})\right)^2 e^{i(\mathbf{q}\cdot\mathbf{R}_{j's'}-\omega^{\nu}(\mathbf{q})t)}\varepsilon_{s'\alpha'}^{\nu} \quad &= \sum_{j=1}^{N}\sum_{s=1}^{2}\sum_{\alpha=1}^{3}\mathcal{K}_{j's'\alpha'}^{js\alpha} \\ &\times\left(\sum_{\mathbf{q}_1} e^{i(\mathbf{q}_1\cdot\mathbf{R}_{js}-\omega^{\nu}(\mathbf{q}_1)t)}\varepsilon_{s\alpha}^{\nu}(\mathbf{q}_1)\right. \\ &\left.-\sum_{\mathbf{q}_2} e^{i(\mathbf{q}_2\cdot\mathbf{R}_{j's'}-\omega^{\nu}(\mathbf{q}_2)t)}\varepsilon_{s\alpha}^{\nu}(\mathbf{q}_2)\right). \end{aligned} \tag{2.33}$$

Multiplying both sides of Eq. (2.33) with $e^{-i(\mathbf{q}'\cdot\mathbf{R}_{j's'}-\omega^{\nu}(\mathbf{q}')t)}$, taking a summation $\sum_{j'=1}^{N}$, and using orthonormality condition:

$$\sum_{j'}^{N} e^{i[(\mathbf{q}-\mathbf{q}')\cdot\mathbf{R}_{j's'}-\omega^{\nu}(\mathbf{q}')t]} = N\delta_{\mathbf{q}\mathbf{q}'} \quad , \tag{2.34}$$

we get the dynamical matrix equation:

$$\sum_{s=1}^{2}\sum_{\alpha} D_{s'\alpha'}^{s\alpha}(\mathbf{q}')\varepsilon_{s\alpha}^{\nu}(\mathbf{q}') = m\left(\omega^{\nu}(\mathbf{q}')\right)^2\varepsilon_{s'\alpha'}^{\nu}(\mathbf{q}') \quad , \tag{2.35}$$

Fig. 2-6: fig/ch2-normode.eps

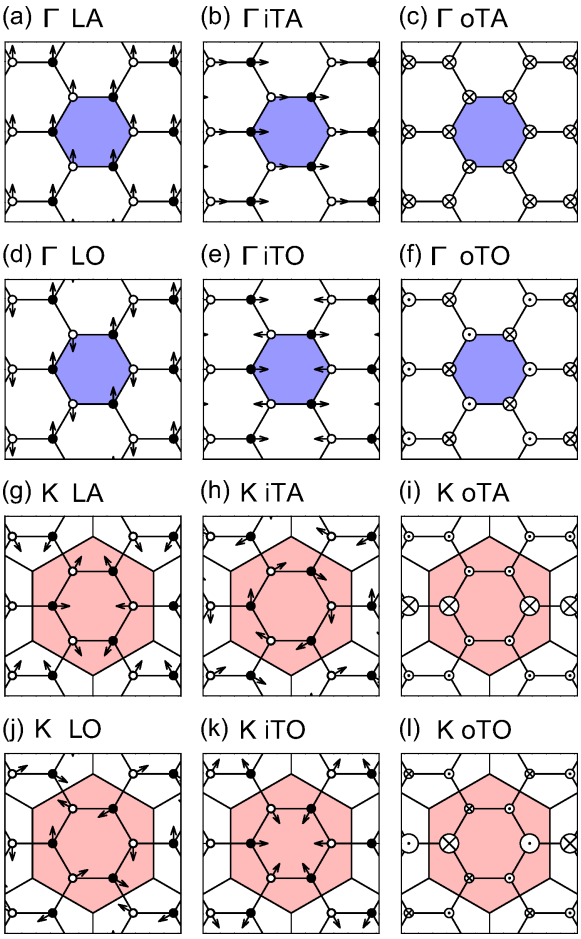

Figure 2-6: Normal mode $\boldsymbol{\varepsilon}^{\nu}(\mathbf{q})$ for six phonon modes (LA, iTA, oTA, LO, iTO, and oTO) at $\mathbf{q} = \Gamma$ [Figs. (a)-(f)] and at $\mathbf{q} = \mathrm{K}$ [Figs. (g)-(l)] [58]. The large and small points in (c),(i) and (f),(l) indicate the magnitudes of the vectors equal to $\sqrt{2}$ and $1/\sqrt{2}$, respectively, of the magnitudes of the vectors in (a), (b), (d), (e), (g), (h), (j), and (k).

where $D^{s\alpha}_{s'\alpha'}(\mathbf{q}')$ is given by:

$$D^{s\alpha}_{s'\alpha'}(\mathbf{q}') = \sum_{j=1}^{N} \left(\delta_{ss'} \sum_{s''}^{2} \mathcal{K}^{js\alpha}_{j's''\alpha'} - e^{i\mathbf{q}'\cdot(R_{js}-R_{j's'})} \mathcal{K}^{js\alpha}_{j's'\alpha'} \right) \quad . \tag{2.36}$$

The force-constant parameters $\mathcal{K}^{js\alpha}_{j's'\alpha'}$ will be presented in Appendix A. Figure 2-7(a) shows the calculated results of the phonon dispersion relations (solid lines) from solving Eq. (2.35) and the corresponding experimental phonon dispersion relations (red dots) for comparison from Refs. [65, 30]. Because of the Kohn anomaly effect (Sec. 1.3.4, the dispersion of the

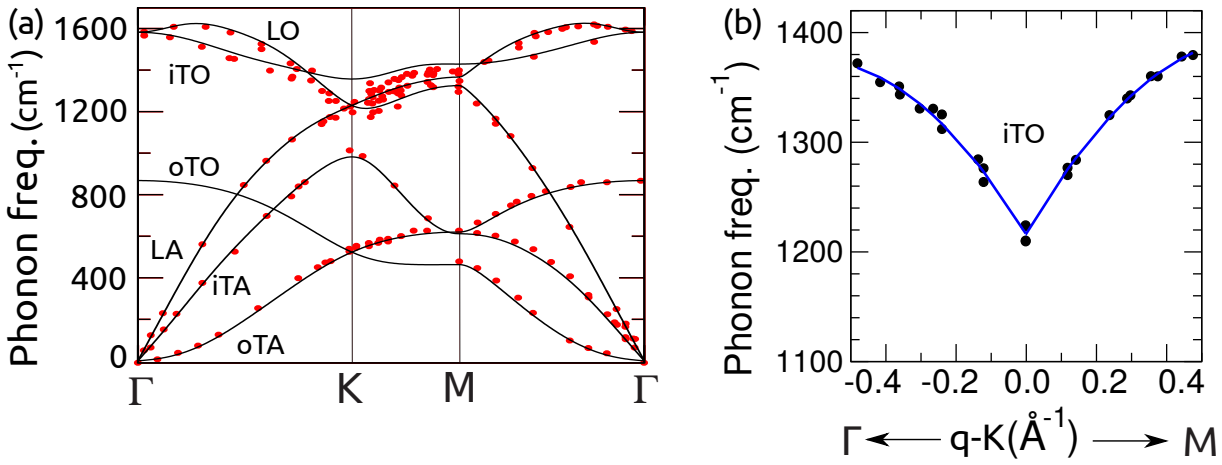

Figure 2-7: (Color online) (a) Calculated (solid lines, this work) and experimental (red dots, from Refs. [65, 30]) phonon dispersion relations. (b) Fitting of Eq. (2.37) (blue line) to the iTO branch from Ref. [66] (dots) near the K point.

in-plane tangential optic (iTO) branch near the K point is discontinuous along the $\Gamma - \mathrm{K} - \mathrm{M}$ path which cannot be reproduced by the force constant model [32]. We fit the iTO frequency from the experiment [66] and use the following fitting formula for the Raman spectra calculation [Fig. 2-7(b)]:

$$\omega_{\mathbf{q}}^{\mathrm{iTO}} = \left\{ -424.81q^2 + 534.47q + 1215.95 + (6.94q^2 + 10.89q)\cos(3\theta) \right\} \text{ cm}^{-1}, \qquad (2.37)$$

where $\mathbf{q}$ is defined using polar coordinates (q, θ) whose center is at the K point and θ is measured from the KM direction. Eq. (2.37) is valid only for $q \leq 0.4$ Å^{-1}, and when $q > 0.4$ Å^{-1}, we use the results from the force constant model for $\omega_{\mathbf{q}}^{\mathrm{iTO}}$. $\omega^{\nu}(\mathbf{q})$ as shown in Fig. 2-7(a).

Fig. 2-7: fig/ch2-phdisp.eps

2.3 Electron-Photon Interaction

The Hamiltonian in Eq. (2.6) is modified in the presence of electromagnetic field as [67]:

$$\begin{aligned} H_{\rm tot} &= \frac{[\mathbf{p} - e\mathcal{A}(\mathbf{r},t)]^2}{2m} + \sum_{js} V(\mathbf{r} - \mathbf{R}_{js}), \\ &= \frac{\mathbf{p}^2}{2m} + \sum_{js} V(\mathbf{r} - \mathbf{R}_{js}) - \frac{e}{m}\mathcal{A}(\mathbf{r},t)\cdot\mathbf{p} + \frac{[e\mathcal{A}(\mathbf{r},t)]^2}{2m}, \\ &= H + H_{\rm op}, \end{aligned} \tag{2.38}$$

where $\mathcal{A}(\mathbf{r},t)$ is the vector potential operator and e is electron charge. Noting that $\boldsymbol{p} = -i\hbar\nabla$, we have used the Coulomb gauge $\nabla\cdot\mathcal{A}(\mathbf{r},t) = 0$ to obtain Eq. (2.38). Here we assume linear optics regime with a small laser intensity so that the term containing $\mathcal{A}^2$ is neglected. Electron-photon interaction thus can be expressed by:

$$M_{\rm op}^{fi}(\mathbf{k}_f,\mathbf{k}_i) = \langle f|H_{\rm op}|i\rangle = \left\langle \psi^f(\mathbf{k}_f,\mathbf{r}) \left| i\frac{e\hbar}{m}\mathcal{A}(\mathbf{r},t)\cdot\nabla \right| \psi^i(\mathbf{k}_i,\mathbf{r}) \right\rangle. \tag{2.39}$$

In order to explicitly write $\mathcal{A}(\mathbf{r},t)$ we assume a classical electric field $\mathbf{E}^{\pm}(\mathbf{r},t) = E_0\exp[i(\boldsymbol{\kappa}\cdot\mathbf{r}\pm\omega_{\pm}t]\mathbf{P}$ with photon energy $\hbar\omega_{\pm}$ and polarization direction $\mathbf{P}$. Electric field notation $\mathbf{E}^{+}$ ($\mathbf{E}^{-}$) represents electric field for photon emission (absorption). From the Maxwell equation, we obtain the following relations:

$$\begin{aligned} \mathcal{A}^{\pm}(\mathbf{r},t) &= \frac{1}{\omega_{\pm}^2}\frac{\partial\mathbf{E}^{\pm}(\mathbf{r},t)}{\partial t}, \\ &= \frac{-i}{\omega_{\pm}}\sqrt{\frac{I_0}{c\epsilon_0}}e^{i(\boldsymbol{\kappa}\cdot\mathbf{r}\pm\omega_{\pm}t)}\mathbf{P}, \end{aligned} \tag{2.40}$$

where $I_0 = E_0^2/\mu_0 c$ is the laser intensity defined by the length of the Poynting vector, μ_0 is the permeability of vacuum, ϵ_0 is the dielectric constant of vacuum, and c is the speed of light. When light wavelength $\lambda = 2\pi/\kappa \sim 500\,\text{nm}$ is much greater than the lattice constant of graphene $a \sim 0.2\,\text{nm}$, we use the dipole approximation by assuming that $\kappa \ll \mathbf{k}_i$ and $\kappa \ll \mathbf{k}_f$. Momentum conservation of Eq. (2.39) requires $\mathbf{k}_f = \mathbf{k}_i + \boldsymbol{\kappa}$, now with the dipole

approximation we assume $\mathbf{k}_f \approx \mathbf{k}_i$. Substituting Eq. (2.40) into Eq. (2.39) we obtain:

$$M_{\rm op}^{fi}(\mathbf{k}) = \frac{e\hbar}{m\omega_{\pm}}\sqrt{\frac{I_0}{\epsilon_0 c}}\mathbf{D}^{fi}(\mathbf{k})\cdot\mathbf{P}, \tag{2.41}$$

where

$$\mathbf{D}^{fi}(\mathbf{k}) = \left\langle \psi^f(\mathbf{k},\mathbf{r})|\nabla|\psi^i(\mathbf{k},\mathbf{r})\right\rangle, \tag{2.42}$$

is the dipole matrix element. The selection of + or − sign in Eq. (2.41) depends on selection of i and f. In case of the Stokes Raman scattering which considers phonon emission, for $M_{\rm op}^{\rm cv}(\mathbf{k})$ we select $\hbar\omega_+ = E_{\rm L}$ with $E_{\rm L}$ is the photon energy and for $M_{\rm op}^{\rm vc}(\mathbf{k})$ we select $\hbar\omega_- = E_{\rm L} - \hbar\omega_{\rm ph}$ with $\hbar\omega_{\rm ph}$ is the phonon energy. Substituting electron wave function from Eq. (2.4) into Eq. (2.42), we obtain:

$$\mathbf{D}^{fi}(\mathbf{k}) = \frac{1}{N}\sum_{ss'}\sum_{jj'} C_s^{f*}(\mathbf{k})C_{s'}^{i}(\mathbf{k})e^{i\mathbf{k}\cdot(\mathbf{R}_{js}-\mathbf{R}_{j's'})}\mathbf{d}(\mathbf{R}_{js}-\mathbf{R}_{j's'}), \tag{2.43}$$

where

$$\mathbf{d}(\mathbf{R}) = \int d\mathbf{r}\varphi(\mathbf{r})\nabla\varphi(\mathbf{r}-\mathbf{R}), \tag{2.44}$$

is the atomic dipole vector. In Fig. 2-8(a) we show the magnitude of $\mathbf{d}(\mathbf{R})$ parameterized from density-functional theory employing the local density approximation (LDA) and using a local orbital basis set [62]. Calculated result of $M_{\rm op}^{\rm cv}(\mathbf{k})$ using $\hbar\omega_+ = 1\,\text{eV}$ is presented in Fig. 2-8(b) and (c). Electronic wave vector $\mathbf{k}$ is selected from an equi–energy line with a condition $E_{\mathbf{k}}^{\rm c} - E_{\mathbf{k}}^{\rm v} = \hbar\omega_+$ near the K point. From the equi–energy line we define an angle θ measured from the $\mathbf{k}_x$– axis [inset of Fig. 2-8(b)]. In Fig. 2-8(b), for $\mathbf{P}_x$ polarization parallel to $\mathbf{k}_x$ (solid line), imaginary part of $M_{\rm op}^{\rm cv}(\mathbf{k})$ shows similar behavior with $\sin\theta$, and for $\mathbf{P}_y$, $M_{\rm op}^{\rm cv}(\mathbf{k})$ is proportional to $\cos\theta$. Real part of $M_{\rm op}^{\rm cv}(\mathbf{k})$ vanishes, therefore is not shown. The maximum amplitude of $|M_{\rm op}^{\rm cv}(\mathbf{k})|$ is slightly larger for $\mathbf{P}_x$ polarization compared with that for $\mathbf{P}_y$ (see Fig. 2-8(c)].

Fig. 2-8: fig/ch2-elop.eps

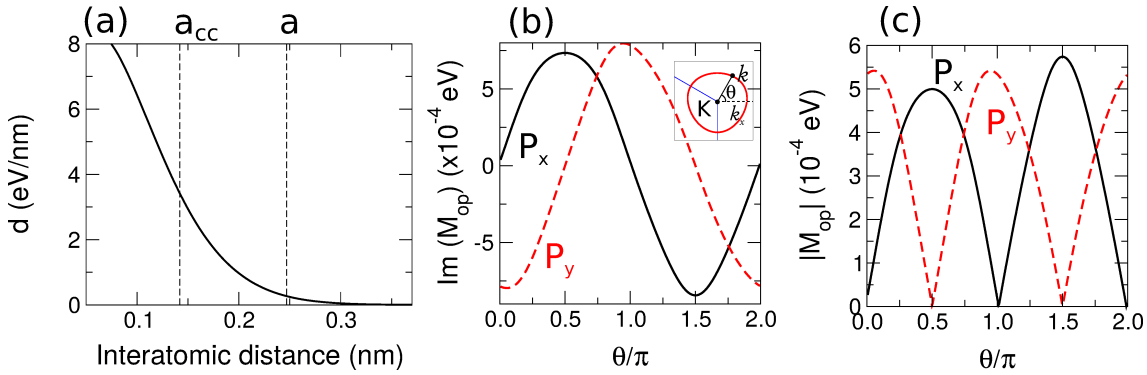

Figure 2-8: (a) magnitude of atomic dipole vector $|\mathbf{d}|$ as a function of interatomic distance. Nearest carbon-carbon distance $a_{\rm cc} = 0.142\,\text{nm}$ and second nearest neighbor which is equal to $a = 0.246\,\text{nm}$ are indicated in the figure. (b) Imaginary parts of electron-photon matrix element as a function of angle θ measured from $\mathbf{k}_x$-axis for the $\mathbf{P}_x$ ($\parallel \mathbf{k}_x$) polarization (solid line) and $\mathbf{P}_y$ ($\perp \mathbf{k}_x$) polarization (dashed line). Inset: equi–energy line for $E^{\rm c}_{\mathbf{k}} - E^{\rm v}_{\mathbf{k}} = 1\,\text{eV}$ near the K point and definition of θ and $\mathbf{k}_x$. (c) Magnitude of electron photon interaction as a function of θ for the $\mathbf{P}_x$ polarization (solid line) and $\mathbf{P}_y$ polarization (dashed line).

2.4 Electron-Phonon Interaction

Due to the presence of ν mode of vibration, atomic position at j–th unit cell and s–th atomic site ($\mathbf{R}_{js}$) is displaced by:

$$\mathbf{u}^{\nu}_{js} = \sum_{\mathbf{q}} \sqrt{\frac{\hbar(n^{\nu}(\mathbf{q})+1)}{2Nm\omega^{\nu}(\mathbf{q})}}\, \boldsymbol{\varepsilon}^{\nu}_{s}(\mathbf{q}) e^{i(\mathbf{q}\cdot\mathbf{R}_{js} - \omega^{\nu}\mathbf{q}t)} \quad , \tag{2.45}$$

similar to Eq. (2.30) but we write explicitly the phonon amplitude $A^{\nu}(\mathbf{q})$ expressed in the second quantization and only consider phonon emission (Stokes) process. Here $n^{\nu}(\mathbf{q})$ is phonon occupation number and in thermal equilibrium is expressed by the Bose-Einstein distribution function:

$$n^{\nu}(\mathbf{q}) = \frac{1}{e^{\hbar\omega^{\nu}(\mathbf{q})/k_{\rm B}T} - 1} \quad , \tag{2.46}$$

where $k_{\rm B}$ is the Boltzmann constant. Displacement $\mathbf{u}^{\nu}_{js}$ deforms the interatomic potential

$$V(\mathbf{r} - \mathbf{R}_{js} - \mathbf{u}^{\nu}_{js}) \approx V(\mathbf{r} - \mathbf{R}_{js}) - \sum_{js} \mathbf{u}^{\nu}_{js} \cdot \nabla V(\mathbf{r} - \mathbf{R}_{js}) + \mathcal{O}({\mathbf{u}^{\nu}_{js}}^2). \tag{2.47}$$

The first term of Eq. (2.47) is the unperturbed interatomic potential and has been taken into account in determining the tight binding parameters of electron dispersion relations (Sec. 2.1). The second term is the deformation potential due to ν phonon emission process. In Eq. (2.47), we have used a rigid ion approximation in which the deformation potential due to atomic motion $\nabla_{\mathbf{R}} V(\mathbf{r}-\mathbf{R})$ is approximately to be the same as $\nabla V(\mathbf{r}-\mathbf{R})$ recalling $\mathbf{R}$ is the atomic coordinate and $\mathbf{r}$ is the electron coordinate. The rigid ion approximation assumes that electron can always follow the atomic motion. This approximation is valid for non-polar atomic structure such as carbon materials [68].

The electron-phonon interaction accounts the transition of an electron from band i and momentum $\mathbf{k}$ to band f and momentum $\mathbf{k}'$ by emitting a ν phonon with momentum $\mathbf{q}$. The magnitude of electron-phonon matrix element is given by

$$M_{\mathrm{ep}}^{fi\nu}(\mathbf{k},\mathbf{k}') = -\sum_{js} \left\langle \psi^f(\mathbf{k}',\mathbf{r}) \left| \mathbf{u}_{js}^{\nu} \cdot \nabla V(\mathbf{r}-\mathbf{R}_{js}) \right| \psi^i(\mathbf{k},\mathbf{r}) \right\rangle . \tag{2.48}$$

We recall $\psi^i(\mathbf{k},\mathbf{r})$ from Eq. (2.4), $\mathbf{u}_{js}^{\nu}$ from Eq. (2.45) to get:

$$\begin{aligned} M_{\mathrm{ep}}^{fi\nu}(\mathbf{k},\mathbf{k}') = \; & -\sum_{\mathbf{q}} \sum_{u,u1,u2} \sqrt{\frac{\hbar(n^{\nu}(\mathbf{q})+1)}{2N^3 m\omega^{\nu}(\mathbf{q})}} e^{-i(\mathbf{k}'\cdot\mathbf{R}_{u1}-\mathbf{q}\cdot\mathbf{R}_u-\mathbf{k}\cdot\mathbf{R}_{u2})} C_{s1}^{f*} C_{s2}^{i} \\ & \times \left\langle \varphi_{s1}(\mathbf{r}-\mathbf{R}_{u1}) \left| \nabla V(\mathbf{r}-\mathbf{R}_u) \right| \varphi_{s2}(\mathbf{r}-\mathbf{R}_{u2} \right\rangle \cdot \boldsymbol{\varepsilon}_s^{\nu}(\mathbf{q}) \end{aligned} \tag{2.49}$$

where we have used a simplified index $u = \{j, s\}$. Furthermore, we have dropped the time dependent from Eq. (2.45) because we have assumed conservation of energy $\delta(E_{\mathbf{k}'}^{f} - \hbar\omega^{\nu}(\mathbf{q}) - E_{\mathbf{k}}^{i})$ through the Fermi golden rule. Summation over $u, u1, u2$ in Eq. (2.49) can be split into three parts by considering (1)$u = u1$, (2) $u = u2$, and (3) $u1 = u2$. For the case (1) we obtain:

$$\begin{aligned} M_{\mathrm{ep}}^{fi\nu(\mathrm{I})}(\mathbf{k},\mathbf{k}') = \; & -\sum_{\mathbf{q}} \sum_{u,u2} \sqrt{\frac{\hbar(n^{\nu}(\mathbf{q})+1)}{2N^3 m\omega^{\nu}(\mathbf{q})}} e^{-i(\mathbf{k}'-\mathbf{q}-\mathbf{k})\cdot\mathbf{R}_u} e^{i\mathbf{k}\cdot(\mathbf{R}_{u2}-\mathbf{R}_u)} C_{s}^{f*} C_{s2}^{i} \\ & \times \left\langle \varphi_{s}(\mathbf{r}) \left| \nabla V(\mathbf{r}) \right| \varphi_{s2}(\mathbf{r}-\mathbf{R}_{u2}-\mathbf{R}_u) \right\rangle \cdot \boldsymbol{\varepsilon}_s^{\nu}(\mathbf{q}). \end{aligned} \tag{2.50}$$

Since $\sum_u e^{-i(\mathbf{k}'-\mathbf{q}-\mathbf{k})\cdot\mathbf{R}_u} = N\delta(\mathbf{k}'-\mathbf{q}-\mathbf{k})$ representing a conservation of momentum during phonon emission, Eq. (2.50) is now simplified as:

$$\begin{aligned} M_{\rm ep}^{fi\nu({\rm I})}(\mathbf{k},\mathbf{k}') = & -\sqrt{\frac{\hbar(n^\nu(\mathbf{q})+1)}{2Nm\omega^\nu(\mathbf{q})}}\sum_{s,s',j,j'} e^{i\mathbf{k}\cdot(\mathbf{R}_{j's'}-\mathbf{R}_{js})} C_s^{f*} C_{s'}^i \\ & \times \boldsymbol{\beta}(\mathbf{R}_{j's'}-\mathbf{R}_{js})\cdot\boldsymbol{\varepsilon}_s^\nu(\mathbf{q}), \end{aligned} \tag{2.51}$$

where

$$\boldsymbol{\beta}(\mathbf{R}) = \int d\mathbf{r}\varphi(\mathbf{r})\nabla V(\mathbf{r})\varphi(\mathbf{r}-\mathbf{R}). \tag{2.52}$$

In a similar fashion, for the case (2) and (3) we can obtain:

$$\begin{aligned} M_{\rm ep}^{fi\nu({\rm II})}(\mathbf{k},\mathbf{k}') &= -\sqrt{\frac{\hbar(n^\nu(\mathbf{q})+1)}{2Nm\omega^\nu(\mathbf{q})}}\sum_{s,s',j,j'} e^{i\mathbf{k}'\cdot(\mathbf{R}_{j's'}-\mathbf{R}_{js})} C_s^{f*} C_{s'}^i \\ &\quad \times \boldsymbol{\alpha}(\mathbf{R}_{j's'}-\mathbf{R}_{js})\cdot\boldsymbol{\varepsilon}_s^\nu(\mathbf{q}), \end{aligned} \tag{2.53}$$

$$\begin{aligned} M_{\rm ep}^{fi\nu({\rm III})}(\mathbf{k},\mathbf{k}') &= -\sqrt{\frac{\hbar(n^\nu(\mathbf{q})+1)}{2Nm\omega^\nu(\mathbf{q})}}\sum_{s,s',j,j'} e^{i\mathbf{q}\cdot(\mathbf{R}_{j's'}-\mathbf{R}_{js})} C_s^{f*} C_{s'}^i \\ &\quad \times \boldsymbol{\lambda}(\mathbf{R}_{j's'}-\mathbf{R}_{js})\cdot\boldsymbol{\varepsilon}_s^\nu(\mathbf{q}), \end{aligned} \tag{2.54}$$

where

$$\boldsymbol{\alpha}(\mathbf{R}) = \int d\mathbf{r}\varphi(\mathbf{r})\nabla V(\mathbf{r}-\mathbf{R})\varphi(\mathbf{r}-\mathbf{R}), \tag{2.55}$$

$$\boldsymbol{\lambda}(\mathbf{R}) = \int d\mathbf{r}\varphi(\mathbf{r})\nabla V(\mathbf{r}-\mathbf{R})\varphi(\mathbf{r}). \tag{2.56}$$

From results in Eqs. (2.51), (2.53), (2.54) electron-phonon matrix element in Eq. (2.49) is

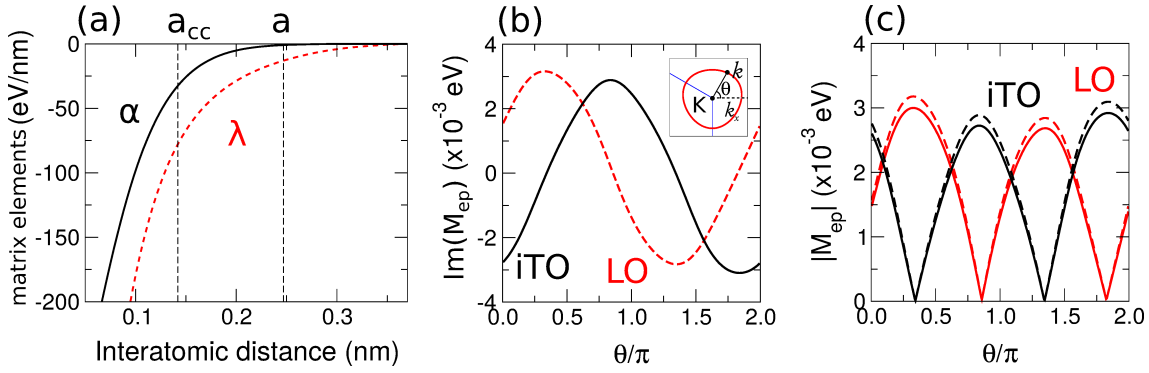

Figure 2-9: (a) Magnitude of off-site deformation potential α and on-site deformation potential λ as a function of interatomic distance. Nearest carbon-carbon distance $a_{cc} = 0.142\,\text{nm}$ and second nearest neighbor which is equal to $a = 0.246\,\text{nm}$ are indicated in the figure. (b) Imaginary parts of electron-phonon matrix element $M_{ep}^{cc\nu}(\mathbf{k},\mathbf{k})$ for $\nu =$ iTO (solid line) and $\nu =$ LO (dashed line). Inset: equi–energy line for $E_{\mathbf{k}}^{c} - E_{\mathbf{k}}^{v} = 1\,\text{eV}$ near the K point and definition of θ and $\mathbf{k}_x$. (c) Magnitude of $|M_{ep}^{vv\nu}(\mathbf{k},\mathbf{k})|$ (solid lines) and $|M_{ep}^{cc\nu}(\mathbf{k},\mathbf{k})|$ (dashed lines) for $\nu =$ iTO (black lines) and $\nu =$ LO (red lines).

written as:

$$
\begin{aligned}
M_{ep}^{fi\nu}(\mathbf{k},\mathbf{k}') \;=\; & -\sqrt{\frac{\hbar(n^{\nu}(\mathbf{q})+1)}{2Nm\omega^{\nu}(\mathbf{q})}} \sum_{s,s',j,j'} C_{s}^{f*} C_{s'}^{i} \\
& \Big\{ e^{i\mathbf{k}'\cdot(\mathbf{R}_{j's'}-\mathbf{R}_{js})} \boldsymbol{\alpha}(\mathbf{R}_{j's'}-\mathbf{R}_{js}) \cdot \boldsymbol{\varepsilon}_{s}^{\nu}(\mathbf{q}) \\
& + e^{i\mathbf{k}\cdot(\mathbf{R}_{j's'}-\mathbf{R}_{js})} \boldsymbol{\beta}(\mathbf{R}_{j's'}-\mathbf{R}_{js}) \cdot \boldsymbol{\varepsilon}_{s}^{\nu}(\mathbf{q}) \\
& + e^{i\mathbf{q}\cdot(\mathbf{R}_{j's'}-\mathbf{R}_{js})} \boldsymbol{\lambda}(\mathbf{R}_{j's'}-\mathbf{R}_{js}) \cdot \boldsymbol{\varepsilon}_{s}^{\nu}(\mathbf{q}) \Big\}.
\end{aligned}
\tag{2.57}
$$

Comparing Eq. (2.52) with Eq. (2.55), we get a relationship $\boldsymbol{\alpha}(\mathbf{R}) = -\boldsymbol{\beta}(\mathbf{R})$. Therefore, the electron-phonon matrix element in Eq. (2.57) only depends on two atomic deformation potential, namely on-site deformation potential $\boldsymbol{\lambda}(\mathbf{R})$ and off-site deformation potential $\boldsymbol{\alpha}(\mathbf{R})$. Figure 2-9(a) shows magnitude of off-site deformation potential α and on-site deformation potential λ as a function of interatomic distance. Values of $\alpha(\mathbf{R})$ and $\lambda(\mathbf{R})$ are parameterized from density-functional theory employing the local density approximation (LDA) and using a local orbital basis set [62]. After obtaining α and λ, we can plot electron-

Fig. 2-9: fig/ch2-elph.eps

phonon matrix element from Eq. (2.57). Figure 2-9(b) shows imaginary parts of $M_{\rm ep}^{\rm cc\nu}(\mathbf{k},\mathbf{k})$ for ν = iTO (solid line) and ν = LO (dashed line). Electronic wave vector $\mathbf{k}$ is selected from an equi–energy line with a condition $E_{\mathbf{k}}^{\rm c} - E_{\mathbf{k}}^{\rm v} = \hbar\omega_+$ near the K point. From the equi–energy line we define an angle θ measured from the $\mathbf{k}_x$– axis [inset of Fig. 2-8(b)]. In this case we set phonon wave vector $\mathbf{q} = 0$. In Eq. (2.57), by setting $\mathbf{q} = 0$, the terms containing $\boldsymbol{\alpha}$ and $\boldsymbol{\beta}$ cancel to each other and the phase factor $e^{i\mathbf{q}\cdot(\mathbf{R}_{j's'}-\mathbf{R}_{js})}$ equals unity. Therefore the phase of $M_{\rm ep}^{\rm cc\nu}(\mathbf{k},\mathbf{k})$ is only determined by product of wave function coefficients with $\boldsymbol{\lambda}(\mathbf{R}_{j's'} - \mathbf{R}_{js}) \cdot \boldsymbol{\varepsilon}_s^{\nu}(\mathbf{q})$. As a result, the imaginary parts of $M_{\rm ep}^{\rm cc\nu}$ behave like a $\sin(\theta - \delta)$ function for ν = LO and a $\cos(\theta - \delta)$ function for ν = iTO with a phase parameter $\delta \approx 0.25\pi$. δ originates from taking into account long range interatomic interaction in the ETB method. This can be the case because in the previous STB calculations, $\delta \approx 0$ was obtained [42, 69]. The real parts of $M_{\rm ep}^{\rm cc\nu}(\mathbf{k},\mathbf{k})$ vanish, therefore are not shown. It is noted that at $\mathbf{q} = 0$, four other phonon modes give zero electron-phonon matrix element. In Fig. 2-9(c) we compare the magnitude of $M_{\rm ep}^{\rm vv\nu}(\mathbf{k},\mathbf{k})$ shown in solid lines with that of $M_{\rm ep}^{\rm cc\nu}(\mathbf{k},\mathbf{k})$ shown in dashed lines for ν = iTO (black lines) and ν = LO (red lines). Maximum values of $M_{\rm ep}^{\rm cc\nu}(\mathbf{k},\mathbf{k})$ are slightly larger compared with that of $M_{\rm ep}^{\rm vv\nu}(\mathbf{k},\mathbf{k})$ for both LO and iTO matrix elements. The difference between $M_{\rm ep}^{\rm cc\nu}(\mathbf{k},\mathbf{k})$ and $M_{\rm ep}^{\rm vv\nu}(\mathbf{k},\mathbf{k})$ comes from electron-hole asymmetry in the band structure of graphene because we consider non-orthonormal basis with a finite overlap integral s in Eq. (2.17). Results in Fig. 2-9(b) and (c) will be shown to be essential when we discuss the quantum interference effect of Raman spectra in Sec. 3.3 and Sec. 4.3.

Chapter 3

Fermi energy dependence of first-order Raman spectra

In this chapter we present the calculation results of the Fermi energy dependence of the first-order Raman spectra. The first order Raman intensity is calculated based on a perturbation theory. The Kohn anomaly (KA) effect is manifested by the change of the G band peak position and its linewidth as a function of the Fermi energy. The phonon renormalization due to electron-hole pair excitation is modeled by second-order perturbation. The calculated results will be compared with experimental results [33] and the previous theoretical works [38, 69]. Next, we calculate the G band intensity as a function of the Fermi energy. We investigate the origin of the quantum interference effect in the G band indicated by the change of the G band intensity as a function of the Fermi energy. Finally, the origin of the Breit-Wigner-Fano (BWF) lineshape in the G band of graphene is discussed due to the presence of continuous electronic Raman spectrum (ERS) at energy range much broader than the G band spectral width. As a result, interference between the ERS and G band spectra give the BWF lineshape. In the ERS intensity calculation we consider the electron-electron interaction between photo-excited carrier with electrons near the Fermi energy. The electron-electron matrix element is given in Sec. 3.4.1.

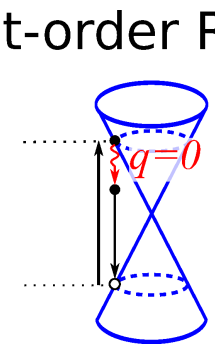

Figure 3-1: (Color online) A schematic of the first-order Raman process. Optical transitions are indicated with straight lines, the electron-phonon interaction is indicated with a wiggly line.

3.1 First-order Raman Spectra

The first-order Raman process as shown in Fig. 3-1 consists of (1) excitation of an electron-hole pair by the electron-photon interaction, (2) phonon emission by means of the electron-phonon interaction, and (3) electron-hole recombination and photoemission by the electron-photon interaction. Based on the three sub-processes, the Raman intensity formula for the first-order Raman process is given by

$$I^{(1)} = \sum_{\nu} \left| \sum_{\mathbf{k}} \frac{M_{\rm op}^{\rm vc}(\mathbf{k}) M_{\rm ep}^{{\rm eh}\nu}(\mathbf{k},\mathbf{k}) M_{\rm op}^{\rm cv}(\mathbf{k}) \left[f(E_{\mathbf{k}}^{\rm v}) - f(E_{\mathbf{k}}^{\rm c}) \right]}{(E_{\rm L} - E_{\mathbf{k}}^{\rm cv} - i\gamma)(E_{\rm L} - E_{\mathbf{k}}^{\rm cv} - \omega_0^{\nu} - i\gamma)} \right|^2 \times \delta(E_{\rm L} - \omega_0^{\nu} - E_{\rm s}), \qquad (3.1)$$

where $E_{\rm L}$ is the laser excitation energy, $E_{\rm s}$ is the scattered photon energy, $E_{\mathbf{k}}^{\rm cv} = E_{\mathbf{k}}^{\rm c} - E_{\mathbf{k}}^{\rm v}$ is the electron energy difference between the conduction (c) and the valence (v) bands at a wave vector $\mathbf{k}$. Energy bands of graphene have been obtained from the extended tight binding method which is discussed in Sec. 2.1. The carrier scattering rate as a function of $E_{\rm L}$ is given by $\gamma = (37.6E_{\rm L} + 13.6E_{\rm L}^2) \times 10^{-3}$ eV according to the calculated results by Venezuela et al. [70] considering the electron-phonon interaction. $f(E)$ is the Fermi distribution function, given by:

$$f(E) = \frac{1}{e^{E/k_{\rm B}T} + 1} \quad , \qquad (3.2)$$

Fig. 3-1: fig/ch3-1st.eps

where k_{B} is the Boltzmann constant and T is absolute temperature. $M_{\mathrm{op}}^{\mathrm{cv}}(\mathbf{k})$ is the electron-photon matrix element accounting for the optical transition of an electron in a state $\mathbf{k}$ from a valence band to a conduction band. We have considered that photon wavelength $\lambda \approx 500\,\mathrm{nm}$ is much larger compared to graphene's lattice constant $\approx 0.2\,\mathrm{nm}$ so that the photon momentum can be neglected and the optical transition occurs vertically (does not change the electron momentum $\mathbf{k}$) [see Sec. 2.3]. $M_{\mathrm{ep}}^{\mathrm{eh}\nu}(\mathbf{q},\mathbf{p}) = M_{\mathrm{ep}}^{\mathrm{cc}\nu}(\mathbf{q},\mathbf{p}) - M_{\mathrm{ep}}^{\mathrm{vv}\nu}(\mathbf{q},\mathbf{p})$ is the carrier-phonon interaction considering an electron (e) in a conduction band or a hole (h) in a valence band making a transition from a state $\mathbf{p}$ to a state $\mathbf{q}$ by emitting a phonon with momentum $\mathbf{q}-\mathbf{p}$, mode ν, and frequency $\omega_{\mathbf{q}-\mathbf{p}}^{\nu}$ [see Sec. 2.4]. Calculation of phonon dispersion relation $\omega_{\mathbf{q}}^{\nu}$ has been performed in Sec. 2.2. Since the optical transition occurs vertically, only phonon with zero momentum is possible in the first-order Raman process so that the electron and hole can recombine. Hereafter, $\hbar = 1$ is used, so that $\omega_{\mathbf{q}}^{\nu}$ has units of energy. The summation over $\mathbf{k}$ in Eq. (3.1) is taken to occur in a uniform square mesh, with a mesh spacing $\Delta k = \gamma/2v$, and $v = 6.46$ eVÅ is the slope of the electron energy dispersion of graphene and $(\Delta k)^2$ is the weight of the integration. It is important to note that both the numerator and denominator of Eq. (3.1) are complex numbers, thus the summation of $\mathbf{k}$ before taking the square plays an important role in the quantum interference effect [71, 31].

3.2 Kohn anomaly effect of first-order Raman spectra

In metal, phonons can excite electrons near the Fermi energy from the valence band to the conduction band [29]. This electronic excitation leads to the change of phonon energy, given by:

$$\omega_{\mathbf{q}}^{\nu} = \omega_{\mathbf{q}}^{(0),\nu} + \omega_{\mathbf{q}}^{(2),\nu}, \tag{3.3}$$

where $\omega_{\mathbf{q}}^{(0),\nu}$ is the unperturbed phonon energy obtained from the phonon dispersion relation shown in Sec. 2.2. Here, $\omega_{\mathbf{q}}^{(2),\nu}$ is the correction term taken from the second-order perturbation of the electron-phonon interaction by the excitation and recombination of an electron-hole

Fig. 3-2: fig/ch3-KA1.eps

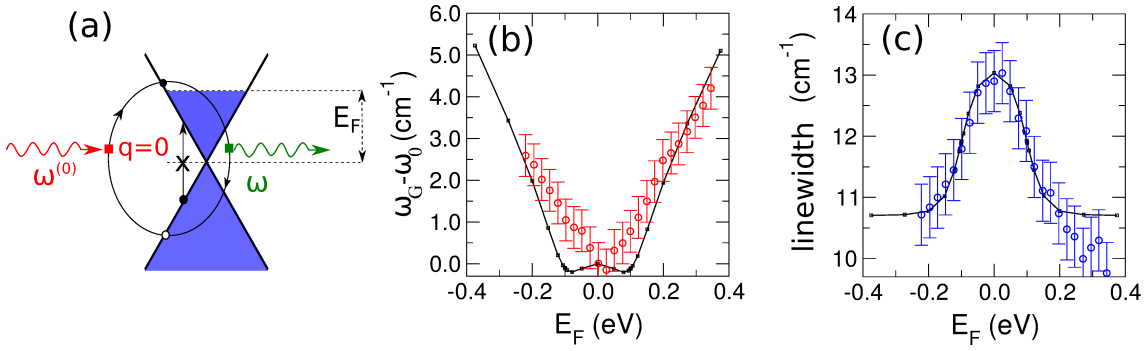

Figure 3-2: (Color online) (a) A schematic of the $\mathbf{q} = 0$ Kohn anomaly process. A phonon with zero wave vector ($\mathbf{q} = 0$) and energy $\omega^{(0)}$ vertically excites an electron-hole pair via the electron-phonon interaction. The electron-hole pair then recombines by emitting a phonon with energy ω. (b,c) The calculated (dotted line) and experimental (open circles) results for the G band peak shift (b) and the G band linewidth (c) as a function of the Fermi energy, respectively, for $T = 300$ K.

pair [Fig. 3-2(a)]:

$$\omega_{\mathbf{q}}^{(2),\nu} = 2\sum_{s,s'}^{\mathrm{c,v}}\sum_{\mathbf{k}} \frac{|M_{\mathrm{ep}}^{ss'\nu}(\mathbf{k},\mathbf{k}+\mathbf{q})|^2 \left[f(E_{\mathbf{k}}^{s}) - f(E_{\mathbf{k}+\mathbf{q}}^{s'})\right]}{\omega_{\mathbf{q}}^{(0),\nu} - E_{\mathbf{k}+\mathbf{q}}^{s'} + E_{\mathbf{k}}^{s} + i\eta}, \tag{3.4}$$

where the prefactor 2 in Eq. (3.4) accounts for the spin degeneracy, while the valley degeneracy is considered in the summation over $\mathbf{k}$ in the first Brillouin zone. The value of $\omega_{\mathbf{q}}^{(2),\nu}$ is a complex number, in which $\mathrm{Re}(\omega_{\mathbf{q}}^{(2),\nu})$ [$-\mathrm{Im}(\omega_{\mathbf{q}}^{(2),\nu})$] gives the phonon energy shift [phonon linewidth]. In Eq. (3.4), the contribution of the interband (intraband) electron-hole pair appears at $s \neq s'$ ($s = s'$).

In a conventional 2D electron gas, the KA effect occurs at $\mathbf{q} = 2\mathbf{k}_{\mathrm{F}}$, where $\mathbf{k}_{\mathrm{F}}$ is the Fermi wave vector. In graphene, due to its unique linear energy bands, the KA occurs at $\mathbf{q} \approx \Gamma$ and $\mathbf{q} \approx \mathrm{K}$. The KA at the Γ (K) point is relevant for the first-order (second-order) Raman spectra. In this section we discuss only the KA effect at the Γ point while the KA effect at the K point will be discussed in Sec. 4.2. The schematic picture of the KA process for $\mathbf{q} = 0$ is shown in Fig. 3-2(a). In the $\mathbf{q} = 0$ KA, a phonon with energy $\omega^{(0)}$ vertically in the $\mathbf{k}-$space excites an electron-hole pair via the electron-phonon interaction [Fig. 3-2(a)]. The electron-hole pair then recombines by emitting a phonon with energy ω.

Employing Eq. (3.4) at $\mathbf{q} = 0$, we can obtain the energy shift [Fig. 3-2(b)] and phonon linewidth [Fig. 3-2(c)] for the G band as a function of the Fermi energy at $T = 300$ K. In Fig. 3-2 we show the calculated (dotted line) and experimental (open circles) results [33] of the G band peak shift and linewidth as a function of the Fermi energy, respectively. The calculated results are in good agreement with the experimental results. In Fig. 3-2(b), we see dips when $2|E_{\rm F}| = \omega_0 \approx 0.2$ eV for the calculation, while the experimental results do not show such dips. These dips are originated from the logarithmic singularities of $\mathrm{Re}(\omega_{\mathbf{q}}^{(2)})$ at $T = 0$ K and are related to interband resonances [52, 69, 53]. For $2|E_{\rm F}| > \omega_0$, the G band energy increases linearly as a function of the Fermi energy. At 0 K, the phonon linewidth shows a step function $\theta(\omega_0 - 2|E_{\rm F}|)$. The step function indicates that when $2|E_{\rm F}| > \omega_0$, the phonon linewidth from the KA effect becomes zero since no excited electron-hole pair meets the resonance condition of Eq. (3.4). At finite T, on the other hand, the Fermi distribution function becomes a smooth function and that is why we get a smooth function of the linewidth as a function of $E_{\rm F}$. It is noted that we add an extrinsic broadening of 10.3 cm^{-1} in our calculations in order to fit with experimental results [33] in Fig. 3-2(c).

3.3 Quantum interference effect of first-order Raman spectra

Next, we calculate the $E_{\rm F}$ dependence of the G band intensity. The G band consists of both the $\mathbf{q} = 0$ longitudinal optic (LO) and in-plane-tangential optic (iTO) modes. From Eq. (3.1), the Raman scattering amplitude of the G band as a function of $\mathbf{k}$ can be written as

$$A_{\mathbf{k}}^{\nu} = \frac{M_{\rm op}^{\rm vc}(\mathbf{k}) M_{\rm ep}^{{\rm eh}\nu}(\mathbf{k},\mathbf{k}) M_{\rm op}^{\rm cv}(\mathbf{k}) \left[f(E_{\mathbf{k}}^{\rm v}) - f(E_{\mathbf{k}}^{\rm c})\right]}{(E_{\rm L} - E_{\mathbf{k}}^{\rm cv} - i\gamma)(E_{\rm L} - E_{\mathbf{k}}^{\rm cv} - \omega_0^{\nu} - i\gamma)}, \quad \nu = \mathrm{iTO},\ \mathrm{LO}. \tag{3.5}$$

In order to understand iTO and LO contributions to the Raman scattering amplitudes $A_{\mathbf{k}}^{\nu}$ at each $\mathbf{k}$ point, we plot the real and imaginary parts of $A_{\mathbf{k}}^{\nu}$ in Eq. (3.5) for the LO and iTO

Fig. 3-3: fig/ch3-Rphase.eps

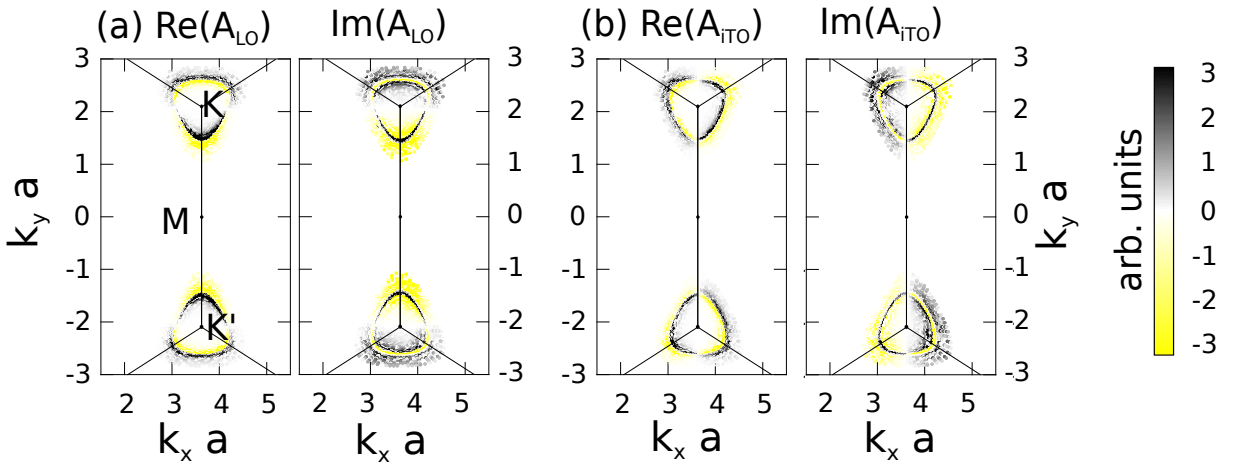

Figure 3-3: (Color online) Calculated results of the real and imaginary parts of the first-order (a) LO and (b) iTO Raman amplitudes in a two dimensional Brillouin zone near the K and K′ points with $E_{\rm L} = 2.33$ eV.

phonons in Fig. 3-3(a) and (b), respectively. Here we use $E_{\rm L} = 2.33$ eV and take a cutoff energy $E_{\rm cut} = 3.5\,$eV so as to reduce the total points of integration for saving computational time. It will be clear that neglecting the contributions from energies above $E_{\rm cut}$ in the integration is reasonable since the Raman intensity is quickly decreasing when $2|E_{\rm F}| > E_{\rm cut}$ [Fig. 3-4(a)]. In Fig. 3-3, deformed triangles near the K and the K′ points indicate equi-energy lines that match the resonant conditions. The inner (outer) circles corresponds to the scattered (incident) resonance when $E^{\rm cv}_{\mathbf{k}} = E_{\rm L} - \omega_G$ ($E^{\rm cv}_{\mathbf{k}} = E_{\rm L}$) which makes one of denominators in Eq. (3.5) becomes $i\gamma$. We see changes in the sign for both the real and imaginary parts of the LO and iTO Raman amplitudes in both the radial and azimuthal directions. The change of sign at the radial direction is related to an opposite phase of $A_{\mathbf{k}}$ between the scattered resonance and the incident resonance. Meanwhile, the change of sign in the azimuthal direction is related to the sign of the electron-phonon matrix element as has been discussed in Sec. 2.4.

In order to analyze the opposite phase between the scattered resonance and the incident resonance, we calculate the phase of the Raman spectra from Eq. (3.5) and setting the matrix

Fig. 3-4: fig/ch3-QI.eps

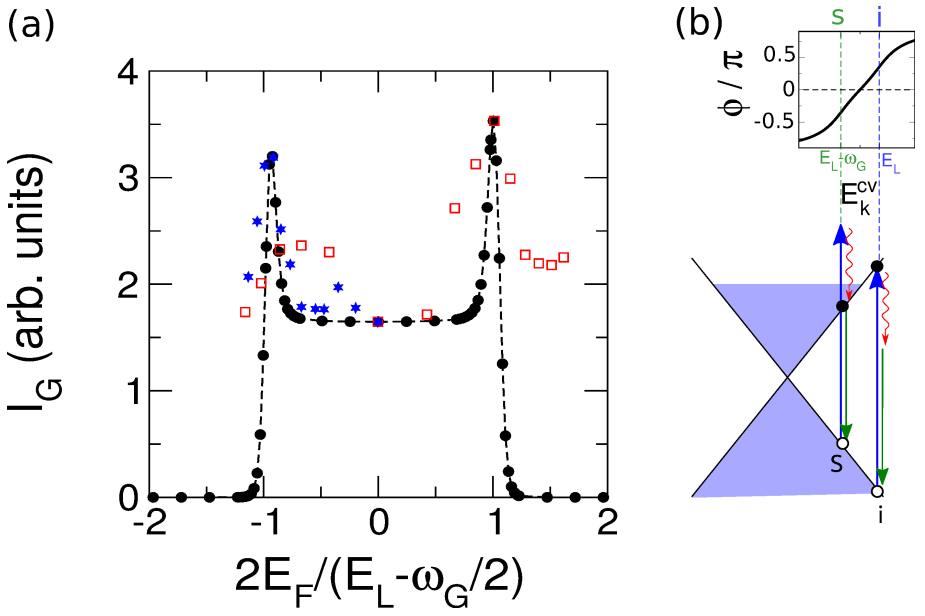

Figure 3-4: (Color online) (a) Calculated results (dots) and experimental results (stars from Ref. [41] and squares from Ref. [72]) of the G band Raman intensity as a function of the reduced Fermi energy. (b) Schematic diagram showing an opposite phase between the incident (i) and scattered (s) resonances. When $2|E_{\rm F}| = E_{\rm L} - \omega_G/2$, the scattered resonance is suppressed, and therefore, the Raman intensity gives a maximum value.

elements equal unity:

$$\phi^{\nu}(E^{\rm cv}_{\mathbf{k}}) = \arg\left(\frac{1}{(E_{\rm L} - E^{\rm cv}_{\mathbf{k}} - i\gamma)(E_{\rm L} - E^{\rm cv}_{\mathbf{k}} - \omega^{\nu}_0 - i\gamma)}\right), \tag{3.6}$$

where $\arg(z) = \tan^{-1}[{\rm Im}(z)/{\rm Re}(z)]$. Because $\omega^{\rm iTO}_0$ and $\omega^{\rm LO}_0$ are degenerated, $\phi^{\rm iTO} = \phi^{\rm LO} = \phi$. The calculated results of ϕ as a function of $E^{\rm cv}_{\mathbf{k}}$ is shown in Fig. (3-4)(b). The Raman phases ϕ of incident and scattered resonances are shown to be opposite to each other. We must pointed out that $\phi = 0$ when $E^{\rm cv}_{\mathbf{k}} = E_{\rm L} - \omega_{\rm G}/2$. The opposite phase of the scattered resonance to the incident resonance is essential insofar as both terms give destructive interference to each other. Therefore, only taking the resonant term for calculating the G band intensity would not give the correct result. We need to at least consider up to $E^{\rm cv}_{\mathbf{k}} \approx E_{\rm L} + \omega_{\rm G}$ to get a realistic intensity. Moreover if we plot the Raman intensity as a function of the Fermi energy as shown in Fig. 3-4(a), it becomes clear that destructive interference between the scattered

resonance and the incident resonance can be suppressed when we set the Fermi energy close to the laser excitation energy. When $2|E_{\mathrm{F}}| = E_{\mathrm{L}} - \omega_{\mathrm{G}}/2$, the scattered resonance cannot occur due to the Pauli blocking effect [Fig. 3-4(b)]. Therefore, in Fig. 3-4(a) we see the largest G band intensity at $2|E_{\mathrm{F}}| = E_{\mathrm{L}} - \omega_{\mathrm{G}}/2$ as pointed out by Chen *et al* [41]. The difference of the intensity at positive and negative E_{F} which comes from the electron-hole asymmetry has been confirmed by Liu *et al* [72] and been discussed in Sec. 2.4. Anisotropy in the azimuthal direction due to the electron-phonon matrix element should give destructive interference, but the effect is negligible in the first-order Raman spectra. We shall see the importance of this effect in the second-order Raman spectra in Sec. 4.3.

3.4 Breit-Wigner-Fano lineshape of first-order Raman spectra

Apart from scattering by phonon in a conventional Raman process, the photoexcited electron (PE) in metallic systems is also scattered by an electron-hole pair excitation by means of the Coulomb interaction. The Raman spectra originate from the electron-hole pair excitation by the Coulomb interaction are called electronic Raman spectra (ERS) [50]. Interference of the continuous ERS and discrete phonon G band gives asymmetric lineshape of the G band spectra which is known as the Breit-Wigner-Fano (BWF) lineshape [50, 51]. The BWF are observed in graphite intercalation compounds [46], metallic nanotubes (m-SWNTs) [47], and graphene [28].

The G Raman scattering and the ERS process are shown in Fig. 3-5. The ERS consist of either intravalley (A) or intervalley (E) interaction, either intravalley (a) or intervalley (e) scattering and either zero momentum transfer ($\mathbf{q} = 0$ first-order) or non-zero momentum transfer ($\mathbf{q} \neq 0$ second-order) processes [51]. When a photon with the laser excitation energy E_{L} is introduced to the graphene sample, the photon excites an electron from a valence band to a conduction band. The photoexcited electron (PE) is then scattered to another

Fig. 3-5: fig/ch3-Fig1.eps

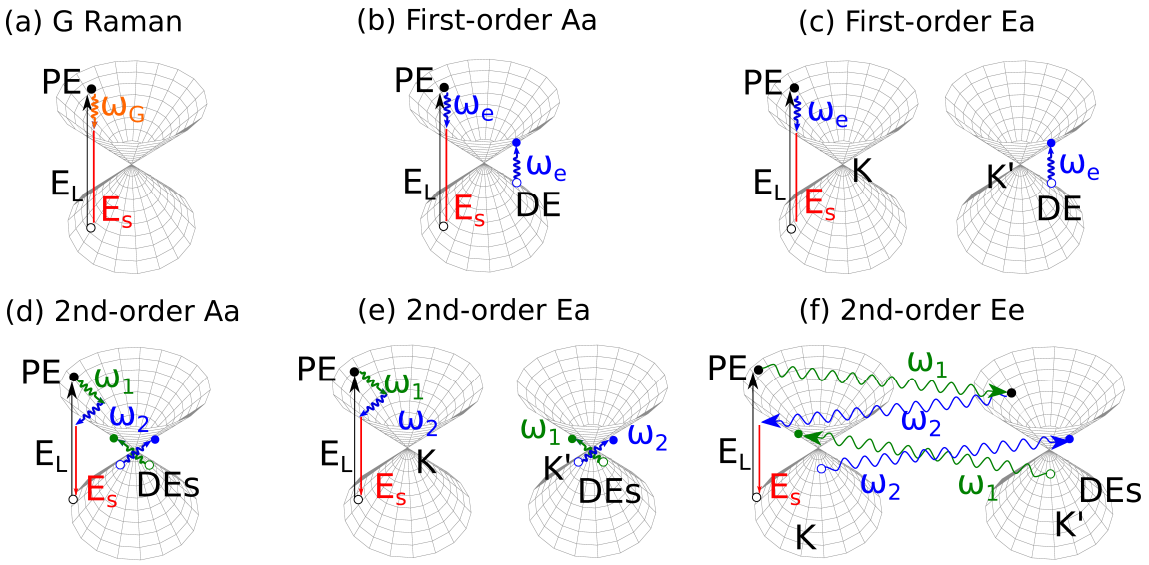

Figure 3-5: (Color online) All possible Raman scattering considered in Eq. (3.7): (a) the G Raman scattering with the Raman shift $\omega_{\rm s} = \omega_G$, (b)-(f) the electronic Raman scattering (ERS) processes. The ERS processes include the Coulomb interactions between a photoexcited electron (PE) and electrons on the Dirac cone (DEs): (b) a first-order intravalley interaction and intravalley scattering (Aa), (c) a first-order intervalley interaction and intravalley scattering (Ea), (d) a second-order intravalley interaction and intravalley scattering (Aa), (e) a second order intervalley interaction and intravalley scattering (Ea), and (f) a second order intervalley interaction and intervalley scattering (Ee). Capital (small) letters A {a} and E {e} label the intravalley and the intervalley interactions {scatterings}. Here $E_{\rm L}$ and E_S are the laser excitation energy and scattered photon energy, respectively. The Raman shift for the first(second)-order processes are $\omega_{\rm s} = \omega_{\rm e} (\omega_{\rm s} = \omega_1 + \omega_2)$.

intermediate state either by the electron-phonon interaction (phonon Raman scattering) or by the Coulomb interaction (ERS) which excites the Dirac electrons (DEs) on the Dirac cone and the electron finally recombines with a hole by emitting a scattered photon energy E_S as shown in Fig. 3-5. Both the phonon Raman scattering and ERS processes share the same initial and final states. Since the phonon Raman process for the G band has been discussed in Sec. 3.1, now we focus on the ERS process.

In the ERS, the Coulomb interaction between the PE and the DEs causes the PE to reduce its energy and changes the PE's momentum while the DEs are being excited. The number of DEs to be excited for each process depends on the number of the scattering order. In the first-order process, only one DE is excited and this process requires a zero momentum

transfer ($\mathbf{q} = 0$) since the PE momentum ($\mathbf{k}$) should be the same as its hole momentum in order to emit a scattered photon with energy E_S by the electron-hole recombination process. In the second-order process, on the other hand, the PE is scattered twice ($\mathbf{k} \to \mathbf{k} - \mathbf{q}$) and ($\mathbf{k} - \mathbf{q} \to \mathbf{k}$) and the PE excites two DEs with relative non-zero electron-hole momenta $-\mathbf{q}$ and $\mathbf{q}$. Due to the degeneracy of the Dirac cone at the K and K′ points of the graphene Brillouin zone (BZ), both the first-order processes and the second-order processes may occur either in the intravalley (A) interactions or in the intervalley (E) interactions.

In the A interactions, the DEs are excited on the same Dirac cone as the PE, while in the E interactions, the DEs are excited on the other Dirac cone. In the case of the E interaction, the initial and final states of the PE and DEs can be in the same (different) valley which is defined by intravalley (intervalley) scattering labeled by a small letter "a" ("e"). The e scattering is not possible in the A interaction because the $+\mathbf{q}$ and $-\mathbf{q}$ scattering are pointing to two different directions at the high symmetry points of graphene; one is pointing to the $\overline{\mathrm{KK'}}$ direction while the other is pointing to the $\overline{\mathrm{K\Gamma}}$ direction. Thus the Ae interaction does not conserve energy during the scattering processes. Combining all possible A and E interactions with the a and e scatterings we have: an Aa [Fig. 3-5(b)] and an Ea [Fig. 3-5(c)] in the first-order processes; and an Aa [Fig. 3-5(d)], an Ea [Fig. 3-5(e)], and an Ee [Fig. 3-5(f)] in the second-order processes.

The BWF asymmetry comes from the interference effect between the phonon spectra with the ERS because both spectra have the same initial and final states for a single PE (Fig. 3-5). Thus in order to calculate the Raman intensity, we first sum up all possible scattering amplitudes for given initial and final states, and then we take the square of the sum of amplitudes [73, 74]

$$I(E_{\mathrm{s}}) = \left[A_{\mathrm{G}}(E_{\mathrm{s}}) + A_{\mathrm{ERS}}(E_{\mathrm{s}})\right]^2, \tag{3.7}$$

where A_{G} and A_{ERS} are the G Raman scattering amplitude and the ERS scattering amplitude, respectively and E_{s} is the scattered photon energy. It is important to mention that the G band intensity in Eq. (3.1) consider the energy conservation in $\delta(E_{\mathrm{L}} - \omega_0^{\mathrm{G}} - E_{\mathrm{s}})$. However, because of the Kohn anomaly effect in Sec. 3.2, delta-function-like spectra of the G band

should not be realistic and we must take into account the G band linewidth for a realistic calculation. Here we define the scattering amplitude of the G phonon as:

$$A_{\rm G}(E_{\rm s}) = \frac{1}{\pi}\sum_{\mathbf{k}} \frac{M_{\rm op}^{\rm vc}(\mathbf{k}) M_{\rm ep}^{\rm ehG}(\mathbf{k},\mathbf{k}) M_{\rm op}^{\rm cv}(\mathbf{k}) \left[f(E_{\mathbf{k}}^{\rm v}) - f(E_{\mathbf{k}}^{\rm c})\right]}{[E_{\rm L} - E_{\mathbf{k}}^{\rm cv} - i\gamma][E_{\rm L} - E_{\mathbf{k}}^{\rm cv} - \omega_0^{\rm G} - i(\gamma + \Gamma_{\rm G})][E_{\rm L} - \omega_0^{\rm G} - E_{\rm s} - i\Gamma_{\rm G}]}, \quad (3.8)$$

where linewidth of the G band $\Gamma_{\rm G}$ is obtained from $-{\rm Im}\left[\omega_0^{(2),{\rm G}}\right]$ in Eq. (3.4) and shown in Fig. 3-2(c). We recall that upon changing $E_{\rm F}$, the G band energy change as $\omega_0^{\rm G} = \omega_0^{(0),{\rm G}} + {\rm Re}\left[\omega_0^{(2),G}\right]$ according to Eq. (3.4) where we strictly constraint $\omega_0^{\rm G}$ to be of a real value for clarity.

The ERS amplitude $A_{\rm ERS}$ is the summation of the amplitude from the first-order $A_{\rm ERS}^{(1)}$ and second-order $A_{\rm ERS}^{(2)}$ processes. The amplitude of the first-order ERS process is given by

$$A_{\rm ERS}^{(1)}(E_{\rm s}) = \frac{1}{\pi}\sum_{\mathbf{k}}\sum_{\mathbf{k}'} \frac{M_{\rm op}^{\rm vc}(\mathbf{k}) K_{\mathbf{k}{\rm c},\mathbf{k}'{\rm v},\mathbf{k}{\rm c},\mathbf{k}'{\rm c}}(0) M_{\rm op}^{\rm cv}(\mathbf{k}) \left[f(E_{\mathbf{k}}^{\rm v}) - f(E_{\mathbf{k}}^{\rm c})\right]}{[E_{\rm L} - E_{\mathbf{k}}^{\rm cv} - i\gamma][E_{\rm L} - E_{\mathbf{k}}^{\rm cv} - \omega_{\mathbf{k}'}^{\rm e} - i(\gamma + \Gamma_{\rm e})][E_{\rm L} - \omega_{\mathbf{k}'}^{\rm e} - E_{\rm s} - i\Gamma_{\rm e}]}, \quad (3.9)$$

where $\omega_{\mathbf{k}'}^{\rm e}$ and $\Gamma_{\rm e} = 30$ meV are, respectively, the energy of the excited DE electron and the inverse life time of the electron-electron interaction. The electron-electron interaction $K_{1,2,3,4}(\mathbf{q})$ defines the scattering of the PE [DE] from an initial state (1) [(2)] to a final state (3) [(4)] which consists of direct ($K^{\rm d}$) and exchange ($K^{\rm x}$) interaction terms as shown in Fig. 3-7(a),

$$K_{1,2,3,4}(\mathbf{q}) = K_{1,2,3,4}^{\rm d}(\mathbf{q}) + K_{1,2,3,4}^{\rm x}(\mathbf{q}), \quad (3.10)$$

for a spin singlet state where $[1,2,3,4] = [\mathbf{k}{\rm c}, \mathbf{k}'{\rm v}, (\mathbf{k}-\mathbf{q}){\rm c}, (\mathbf{k}'+\mathbf{q}){\rm c}]$ in the case of ERS in undoped-graphene ($E_{\rm F} = 0$) [Fig. 3-6(a)]. In the electron doped ($E_{\rm F} > 0$) and the hole doped ($E_{\rm F} < 0$) cases, we add possible intraband transitions $[2,4] = [\mathbf{k}'{\rm c}, (\mathbf{k}'+\mathbf{q}){\rm c}]$ and $[2,4] = [\mathbf{k}'{\rm v}, (\mathbf{k}'+\mathbf{q}){\rm v}]$, respectively, as long as state (2) is occupied and state (4) is unoccupied. We do not consider spin triplet states for simplicity due to the fact that the exchange interaction is sufficiently small compared with the direct Coulomb interaction [51, 75]. The direct $K_{1,2,3,4}^{\rm d}(\mathbf{q})$ and exchange $K_{1,2,3,4}^{\rm x}(\mathbf{q})$ Coulomb interactions between two electrons in the

tight binding approximation are given in Appendix B by

$$K^{\mathrm{d}}_{1,2,3,4}(\mathbf{q}) = \sum_{ss'=\mathrm{A,B}} C^1_s C^2_{s'} C^{*3}_s C^{*4}_{s'} \ \mathrm{Re}\left[v_{ss'}\left(\mathbf{q}\right)\right], \tag{3.11}$$

$$K^{\mathrm{x}}_{1,2,3,4}(\mathbf{q}) = \sum_{ss'=\mathrm{A,B}} C^1_s C^2_{s'} C^{*3}_{s'} C^{*4}_{s} \ \mathrm{Re}\left[v_{ss'}\left(\mathbf{k}'-\mathbf{k}-\mathbf{q}\right)\right], \tag{3.12}$$

C^j_s is a tight binding coefficient for an atomic site $s = \mathrm{A},\ \mathrm{B}$ and a state j. [43] The Fourier transform of the Coulomb potential $v_{ss'}\left(\mathbf{q}\right)$ is defined by

$$v_{ss'}\left(\mathbf{q}\right) = \frac{1}{N}\sum_{u'} e^{i\mathbf{q}\cdot\left(\mathbf{R}_{u's'}-\mathbf{R}_{0s}\right)} v\left(\mathbf{R}_{0s},\mathbf{R}_{u's'}\right), \tag{3.13}$$

where $v(\mathbf{R},\mathbf{R}')$ is the effective Coulomb potential for the π electron system modeled by the Ohno potential [76, 75]

$$v\left(\mathbf{R},\mathbf{R}'\right) = \frac{U_0}{\sqrt{\left(\dfrac{4\pi\epsilon_0}{e^2}U_0\left|\mathbf{R}-\mathbf{R}'\right|\right)^2+1}}, \tag{3.14}$$

in which U_0 is the on-site Coulomb potential for two π electrons at the same site $\mathbf{R} = \mathbf{R}'$, defined by

$$U_0 = \int d\mathbf{r}d\mathbf{r}'\frac{e^2}{|\mathbf{r}-\mathbf{r}'|}\varphi^2(\mathbf{r})\varphi^2(\mathbf{r}') = 11.3 \text{ eV}. \tag{3.15}$$

The amplitude of the second-order ERS process is given by

$$\begin{aligned} A^{(2)}_{\mathrm{ERS}}(E_{\mathrm{s}}) =& \frac{1}{\pi}\sum_{\mathbf{k}}\sum_{\mathbf{k}'\mathbf{k}''\mathbf{q}} \frac{M^{\mathrm{vc}}_{\mathrm{op}}(\mathbf{k})K_{(\mathbf{k}-\mathbf{q})\mathrm{c},(\mathbf{k}''+\mathbf{q})\mathrm{v},\mathbf{k}\mathrm{c},\mathbf{k}''\mathrm{c}}(-\mathbf{q})}{[E_{\mathrm{L}}-E^{\mathrm{cv}}_{\mathbf{k}}-i\gamma][E_{\mathrm{L}}-E^{\mathrm{cv}}_{\mathbf{k}}-\omega^1_{\mathbf{k}'}-\omega^2_{\mathbf{k}''}-i(\gamma+2\Gamma_{\mathrm{e}})]} \\ &\times \frac{K_{\mathbf{k}\mathrm{c},\mathbf{k}'\mathrm{v},(\mathbf{k}-\mathbf{q})\mathrm{c},(\mathbf{k}'+\mathbf{q})\mathrm{c}}(\mathbf{q})M^{\mathrm{cv}}_{\mathrm{op}}(\mathbf{k})\left[f(E^{\mathrm{v}}_{\mathbf{k}})-f(E^{\mathrm{c}}_{\mathbf{k}})\right]}{[E_{\mathrm{L}}-\omega^1_{\mathbf{k}'}-E_{\mathrm{s}}-i\Gamma_{\mathrm{e}}][E_{\mathrm{L}}-\omega^1_{\mathbf{k}'}-\omega^2_{\mathbf{k}''}-E_{\mathrm{s}}-i2\Gamma_{\mathrm{e}}]}, \end{aligned} \tag{3.16}$$

where $\omega^1_{\mathbf{k}'}$ and $\omega^2_{\mathbf{k}''}$ are the energies of the DEs emitted for the electron-electron interaction in the second-order ERS process.

Fig. 3-6: fig/ch3-ee.eps
Fig. 3-7: fig/ch3-ersef.eps

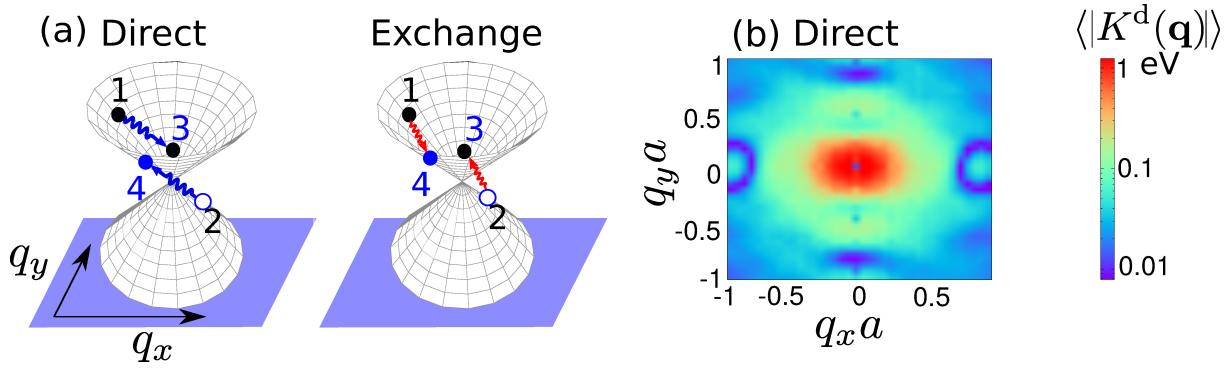

Figure 3-6: (Color online) (a) Illustration of the direct and exchange Coulomb interaction. (b) The averaged absolute value of the direct Coulomb interaction matrix element $K^{\rm d}$ as a function of momentum transfer $\mathbf{q}$. The corresponding results for the exchange interaction is not shown in the figure.

3.4.1 Electronic Raman Spectra and the BWF asymmetry

Since the electron-electron interaction depends on initial states $(1,2)$ of PE and DE and also on a momentum transfer $(\mathbf{q})$, we consider the averaged absolute value of the matrix elements over the initial states in order to visualize the strength of the electron-electron interaction in a simple manner. In Fig. 3-6(b), we show the averaged absolute value of $K^{\rm d}_{1,2,3,4}(\mathbf{q})$ over the initial states $(1,2)$

$$\langle|K^{\rm d}(\mathbf{q})|\rangle = \frac{1}{N_1 N_2}\sum_{(1,2)}|K^{\rm d}_{1,2,3,4}(\mathbf{q})|, \tag{3.17}$$

where $N_1 = N_2 = N_{\mathbf{k}}$ is number of $\mathbf{k}$-points in the first Brillouin zone. As shown in Fig. 3-6(b), $K^{\rm d}$ disappears at $\mathbf{q} = 0$, indicated by a small black dot at $\mathbf{q} = (0,0)$, due to the symmetry of the A and B sublattice wavefunctions in the graphene unit cell which cancel in the summation of $K^{\rm d}$ in Eq. (3.11) [51]. Detailed calculation on the absence of the direct Coulomb interaction at $\mathbf{q} = 0$ is presented in Appendix B. The absence of a direct Coulomb interaction suggests that the ERS should not come from the first-order but from the second order $\mathbf{q} \neq 0$ electron-electron interaction, similar to what has been found in m-SWNTs [51]. The first-order ERS can only be possible by means of the exchange Coulomb interaction. Although we take into account the exchange Coulomb interaction, the Raman intensity from the first-order process is still six-orders of magnitude smaller than that of the second order

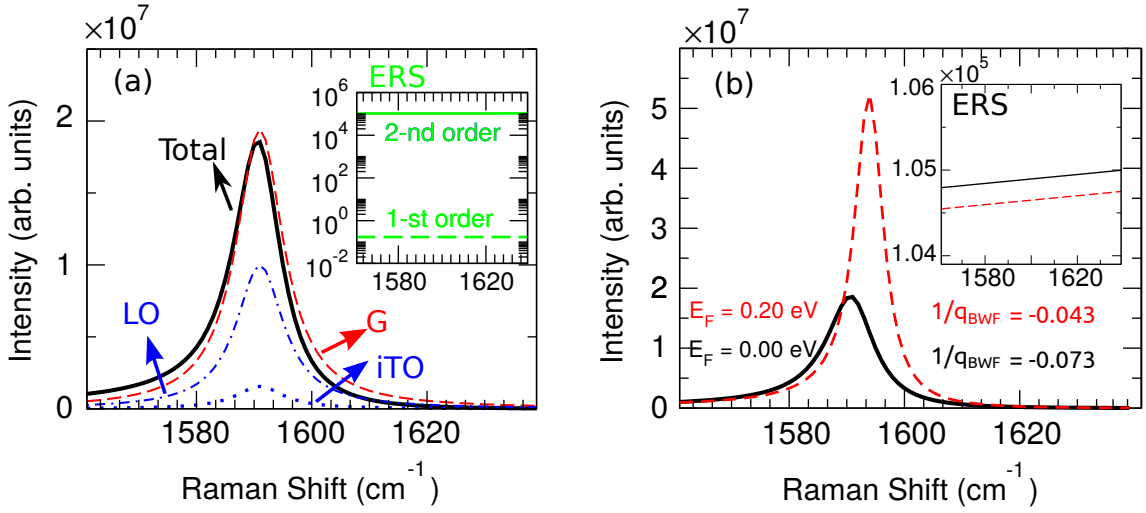

Figure 3-7: (Color online) (a) Calculated Raman intensity according to Eq. (3.7) for $E_{\rm F} = 0.00$ eV (solid line) compared with the Lorentzian G mode intensity by taking the square of A_G in Eq. (3.8) (dashed line). The G mode constituents, i.e. iTO and LO, are indicated by a dotted line and a dot-dashed line, respectively. An asymmetric lineshape (solid line) appears due to the interference effect between the G mode with the ERS. The inset shows calculated results of the first-order (dashed line) and the second-order (solid line) ERS spectra, indicating that the second-order processes have an intensity value six-orders of magnitude greater than that of the first-order processes. (b) Calculated Raman intensity for $E_{\rm F} = 0.00$ eV (solid line) and $E_{\rm F} = 0.20$ eV (dashed line). The BWF asymmetric factor $1/q_{\rm BWF}$ decreases by increasing the absolute value of $|E_{\rm F}|$ away from the Dirac point because the ERS intensity also decreases by increasing $|E_{\rm F}|$ (inset).

process [see inset of Fig. 3-7(a)]. Therefore, we can safely neglect the first-order processes.

In Fig. 3-7 we present results for the Raman intensity calculation $I(\omega_{\rm s})$ of Eq. (3.7). The solid curve in Fig. 3-7(a) shows the total Raman intensity after considering the interference of the G mode spectra with the ERS spectra, while the dashed red line shows the Lorentzian G phonon spectra by taking the square of its probability amplitudes $A_{\rm G}(\omega_{\rm s})$ [Eq. (3.8)]. The phonon modes for the G band, i.e. the iTO and LO modes, are indicated by a blue dotted line and a blue dot-dashed line, respectively. The calculated results show that LO phonon gives a dominant contribution to the G band intensity. It is clear from Fig. 3-7(a) that the total Raman spectra (the solid line) shows asymmetry around the peak position at 1590 cm^{-1}. In order to understand the results in Fig. 3-7, one can simplify the phonon spectra and the ERS into the following considerations. The G band lineshape is a Lorentzian

function

$$A_{\mathrm{G}}(\omega_{\mathrm{s}}) = \frac{A_0}{i+s} \tag{3.18}$$

where $s = (\omega_{\mathrm{s}} - \omega_{\mathrm{G}})/\Gamma_{\mathrm{G}}$, ω_{s} is the Raman shift, and A_0 is the normalized G band amplitude. Since $A_{\mathrm{ERS}} \ll A_{\mathrm{G}}$, we can consider the ERS lineshape as a constant function $A_{\mathrm{ERS}}(\omega_{\mathrm{s}}) = \eta A_0$ around $\hbar\omega_{\mathrm{G}} - \Gamma_{\mathrm{G}} < \hbar\omega_{\mathrm{s}} < \hbar\omega_{\mathrm{G}} + \Gamma_{\mathrm{G}}$. If we put the definition of A_{G} and A_{s} above into Eq. (3.7), we can get the BWF formula:

$$\begin{aligned} I_{\mathrm{BWF}}(\omega_{\mathrm{s}}) =& A_0^2 \frac{(1 + s/q_{\mathrm{BWF}})^2}{1+s^2} \\ =& A_0^2 \left[\frac{1}{q_{\mathrm{BWF}}^2} + \frac{1 - 1/q_{\mathrm{BWF}}^2}{1+s^2} + \frac{2s/q_{\mathrm{BWF}}}{1+s^2} \right], \end{aligned} \tag{3.19}$$

with the asymmetric factor $1/q_{\mathrm{BWF}} = \eta$ for $|1/q_{\mathrm{BWF}}| \ll 1$. The three terms of Eq. (3.19) correspond to $|A_{\mathrm{ERS}}|^2$, $|A_G|^2$ with assumption $|1/q_{\mathrm{BWF}}| \ll 1$, and an interference term, respectively. The BWF asymmetry appears in the total Raman intensity because the interference term gives a positive (negative) value when s is negative (positive) for a negative $1/q_{\mathrm{BWF}}$. The negative value of the $1/q_{\mathrm{BWF}}$ comes from the sign of electron-phonon matrix element in Eq. (3.8).

By fitting the calculated result to Eq. (3.19), we obtain the fitted values of $1/q_{\mathrm{BWF}}$, which have the same negative sign as the experimental data [28]. For a negative $1/q_{\mathrm{BWF}}$, when ω_{s} is smaller (greater) than ω_{G}, $I(\omega_{\mathrm{s}})$ is greater (smaller) than $|A_G(\omega_{\mathrm{s}})|^2$, indicating that the interference between the G mode and the ERS spectra is constructive (destructive) below (above) the resonance condition $\omega_{\mathrm{s}} = \omega_{\mathrm{G}}$.

By decreasing (increasing) E_{F} further from the Dirac cone, transitions from (to) the unoccupied (occupied) states are suppressed due to the Pauli principle. Thus we expect that the asymmetric factor $|1/q_{\mathrm{BWF}}|$ decreases as we change the E_{F} from the Dirac point $E_{\mathrm{F}} = 0.00$ eV to $E_{\mathrm{F}} = 0.20$ eV as shown in Fig. 3-7(b). The solid line is the intensity of the spectrum with $1/q_{\mathrm{BWF}} = -0.073$ when $E_{\mathrm{F}} = 0.00$ eV, while the blue dashed line is the corresponding curve with $1/q_{\mathrm{BWF}} = -0.043$ when $E_{\mathrm{F}} = 0.20$ eV. The Raman intensity and peak position at $E_{\mathrm{F}} = 0.20$ eV are larger than that at $E_{\mathrm{F}} = 0.00$ eV due to the Kohn

anomaly effect. [32]

Unlike the ERS spectra in m-SWNTs which are Lorentzian functions, [50, 51] the ERS intensity in graphene is a linear function of $\omega_{\rm s}$ [inset of Fig. 3-7(b)]. The positive gradient of the ERS intensity is due to the greater scattering path available to excite DEs in the second-order processes as $\omega_{\rm s}$ increases. The ERS intensity will increase monotonically and will get saturated at $\omega_{\rm s} \geq E_{\rm L}/2$. The absence of the ERS peak intensity in graphene is related to the absence of van-Hove singularities in the energy region from the G mode energy ~ 0.2 eV to $E_{\rm L} = 2.4$ eV. The absence of the ERS peak also becomes the reason why the $1/q_{\rm BWF}$ values of the G mode in graphene are one-order of magnitude smaller compared with that in m-SWNTs. The ERS intensity is about two-orders of magnitude smaller than that of the G mode, and by increasing the $E_{\rm F}$ the ERS intensity decreases only less than 1%; nevertheless the change of the $1/q_{\rm BWF}$ is significant [Fig. 3-7(b)]. Thus, this BWF feature is very sensitive to the presence or absence of the continuum spectra.

In Figs. 3-8(a) and (b), we respectively show our calculated result and the corresponding experimental results (Ref. [28]) for the G band Raman intensity as a function of the Raman shift, which is plotted for various values of $E_{\rm F}$ in the range $-0.20 \leq E_{\rm F} \leq 0.40$ eV. In the experimental results [28], Fig. 3-8(b) was given as a function of gate voltage V_G. For our present purpose of comparing the calculated results and experimental results, we here convert V_G to $E_{\rm F}$ using the relation $E_{\rm F} = {\rm sign}(V_G - V_0)\hbar v_F \sqrt{\alpha\pi|V_G - V_0|}$ where the Fermi velocity $v_F = 10^8$ cm/s, the constant voltage adjusted to the Dirac point $V_0 = -57.5$ V, and the capacitance $\alpha = 7.2 \times 10^{10}$ cm^{-2}V^{-1} for the SiO_2 dielectric medium with a thickness 300 nm [1, 9, 28]. At the charge neutrality point $E_{\rm F} = 0.00$ eV, the G band spectrum is broadened and its frequency is softened due to the Kohn anomaly effect.

Comparison of the BWF asymmetric factor $1/q_{\rm BWF}$ between the theory (square) and experiment (circle) shows a reasonable agreement, as can be seen in Fig. 3-8(c), except for $E_{\rm F} \geq 0.20$ eV when the experimental results deviate from the calculated results. We suppose that the deviation is related to the difficulties of observing the BWF asymmetry

Fig. 3-8: fig/ch3-Fig4.eps

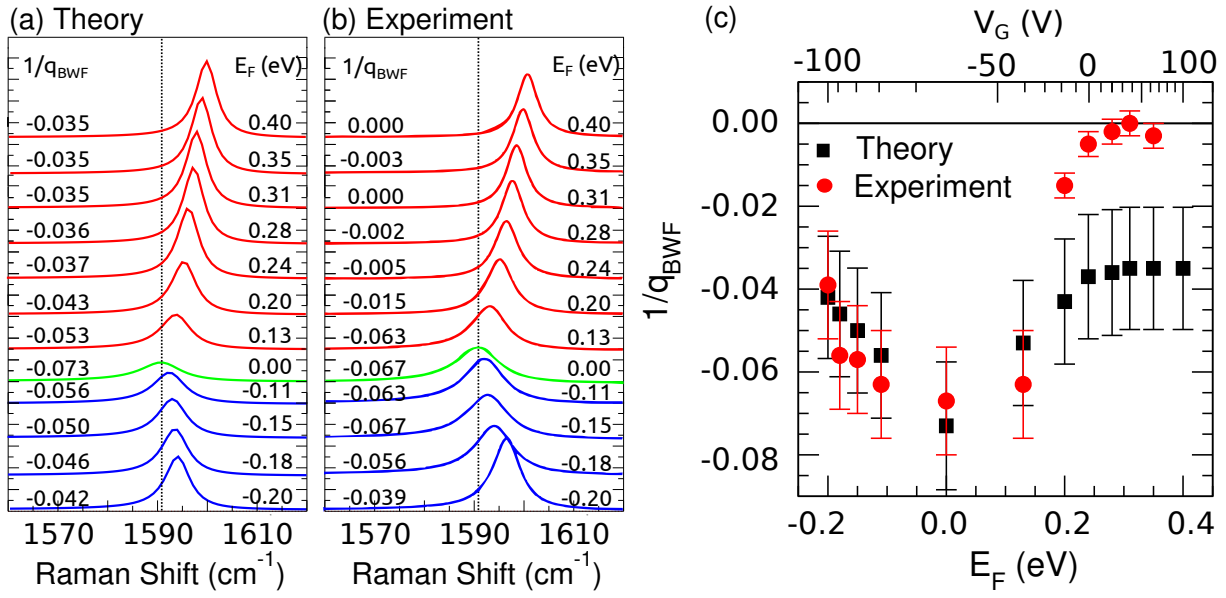

Figure 3-8: (Color online) Comparison between (a) the calculated results (this work) and (b) the experimental results taken from Ref. [28] for the G band Raman intensity as a function of the Raman shift, which is plotted for various values of $E_{\rm F}$ in the range $-0.20 \leq E_{\rm F} \leq 0.40$ eV. The values of $1/q_{\rm BWF}$ obtained from the calculation and the experiment are also given on each plot. (c) Comparison of the BWF asymmetric factor $1/q_{\rm BWF}$ as a function of $E_{\rm F}$ and gate voltage V_G between theory (squares) and experiment (circles). Both the linewidth and the phonon peak frequency-shift are due to the Kohn anomaly effect.

at $E_{\rm F} > 0.20$ eV in the experiment because the continuum ERS intensity is about two or three-orders of magnitude smaller compared with the G band intensity. Such weak ERS spectra might couple strongly with the background spectra in the experiment which make the ERS contribution difficult to observe. The calculated asymmetric factor $1/q_{\rm BWF}$ has a "V"-shaped curve structure as a function of $E_{\rm F}$ with the dip position at $E_F = 0.00$ eV. The decrease of $1/q_{\rm BWF}$ corresponds to the decrease of the ERS intensity due to the suppression of electron-hole pair excitations on the Dirac cone upon doping.

The present agreement between experiment and the theory also reconfirms that plasmons do not contribute to the continuum spectra. When $|E_{\rm F}| > 0$, collective excitations (plasmons) are expected to be generated, and consequently the ERS spectra should be enhanced [77]. However, what we obtain in the present study is that the ERS spectra are in fact suppressed if we increase $|E_{\rm F}|$. Therefore, we rule out the contribution of plasmons in the ERS spectra

and we conclude that only single-particle electron-hole pair excitations are important.

Chapter 4

Fermi energy dependence of second-order Raman spectra

In this chapter we will present the calculation results of the Fermi energy dependence of the second-order Raman spectra. The second-order Raman intensity is calculated based on a perturbation theory including photo-absorption, two-phonon emission, and photo-emission processes. The Kohn anomaly (KA) effect is calculated from Eq. (3.4) described in Chapter 3. We contrast the different of the $\mathbf{q} = 0$ KA process to the $\mathbf{q} \approx$ K KA process. From this different mechanism, two opposite KA effects between the G$'$ band and the G band are compared and are in a good agreement with experimental results by Araujo et al. [33]. We confirm the reliability of the calculation methods by performing the E_{L} dependence of the second-order Raman spectra. Finally, from the E_{F} dependence of Raman intensity, we discuss different quantum interference effect between overtone and combination phonon modes in the second-order Raman spectra.

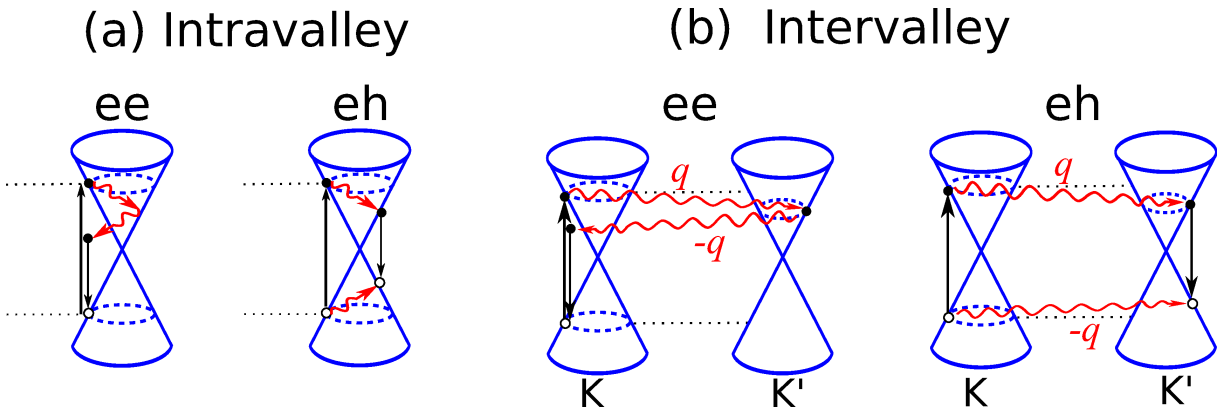

Figure 4-1: (Color online) Schematics of the second-order Raman processes for (a) intravalley and (b) intervalley transitions. The label "ee" describes a scattering process with two consequtive electron-phonon interactions while the label "eh" indicates the electron-phonon interaction followed by the hole-phonon interaction. Optical transitions are indicated with straight lines, the electron-phonon interactions are indicated with wiggly lines.

4.1 Second-order Raman spectra

The second-order Raman processes as shown in Fig. 4-1, consist of (1) excitation of an electron-hole pair by the electron-photon interaction, (2) two-phonon emission by means of the electron-phonon interaction, and (3) electron-hole recombination and photoemission by the electron-photon interaction. The emitted two phonons with modes ν and μ have momenta $\mathbf{q}$ and $-\mathbf{q}$, respectively. Because the optical transition occurs at either the K or K$'$ valleys, the phonon momentum $\mathbf{q}$ can be either $\mathbf{q} \approx \Gamma$ or $\mathbf{q} \approx \mathrm{K}$. In case of $\mathbf{q} \approx \Gamma$ [$\mathbf{q} \approx \mathrm{K}$], an electron moves to the same [different] valley, known as the intravalley [intervalley] transition of the electron-phonon interaction as shown in Fig. 4-1(a) [Fig. 4-1(b)]. It is noted that the distance between the K and K$'$ points equals $|\overline{\Gamma\mathrm{K}}|$ and simply refer to as $\mathbf{q} = \mathrm{K}$. In this thesis, we do not discuss the intravalley transition of the second-order Raman spectra because its Raman intensity is much smaller compared with that of the intervalley transition [37].

Depending on the carriers taking part in the scattering event, the Raman intensity for-

Fig. 4-1: fig/ch4-2nd.eps

mula is given by:

$$I^{(2)} = \sum_{\mathbf{q}\nu\mu} \left| A^{\rm ee}_{\mathbf{q}\nu\mu} + A^{\rm hh}_{\mathbf{q}\nu\mu} + A^{\rm he}_{\mathbf{q}\nu\mu} + A^{\rm eh}_{\mathbf{q}\nu\mu} + A^{\rm ee}_{-\mathbf{q}\mu\nu} + A^{\rm hh}_{-\mathbf{q}\mu\nu} + A^{\rm he}_{-\mathbf{q}\mu\nu} + A^{\rm eh}_{-\mathbf{q}\mu\nu} \right|^2 \times \delta(E_{\rm L} - \omega_\nu - \omega_\mu - E_{\rm s}), \tag{4.1}$$

where $A^{\rm eh}_{\mathbf{q}\nu\mu}$ is a Raman amplitude for each process: (1) an electron (e), first, emits a ν phonon with momentum $\mathbf{q}$ and, (2) a hole (h) emits the μ phonon with momentum $-\mathbf{q}$. Here, $A^{\rm eh}_{\mathbf{q}\nu\mu}$ and $A^{\rm eh}_{-\mathbf{q}\mu\nu}$ are not equivalent to each other due to the different time order of the two phonon emission. $A^{\rm ee}_{\mathbf{q}\mu\nu}$ and $A^{\rm ee}_{\mathbf{q}\mu\nu}$ for the intervalley transition are shown in Fig. 4-1(b). Next, we show examples of the Raman amplitude formula for $A^{\rm ee}_{\mathbf{q}\nu\mu}$ and $A^{\rm eh}_{\mathbf{q}\nu\mu}$:

$$A^{\rm ee}_{\mathbf{q}\nu\mu} = \sum_k \frac{M^{\rm vc}_{\rm op}(\mathbf{k}) M^{{\rm cc}\mu}_{\rm ep}(\mathbf{k}, \mathbf{k}+\mathbf{q}) M^{{\rm cc}\nu}_{\rm ep}(\mathbf{k}+\mathbf{q}, \mathbf{k}) M^{\rm cv}_{\rm op}(\mathbf{k}) \left[f(E^{\rm v}_{\mathbf{k}}) - f(E^{\rm c}_{\mathbf{k}}) \right]}{(E_{\rm L} - E^{\rm cv}_{\mathbf{k}} - i\gamma)(E_{\rm L} - E^{\rm c}_{\mathbf{k}+\mathbf{q}} + E^{\rm v}_{\mathbf{k}} - \omega^\nu_{-\mathbf{q}} - i\gamma)(E_{\rm L} - E^{\rm cv}_{\mathbf{k}} - \omega^\nu_{-\mathbf{q}} - \omega^\mu_{\mathbf{q}} - i\gamma)}, \tag{4.2}$$

$$A^{\rm eh}_{\mathbf{q}\nu\mu} = -\sum_k \frac{M^{\rm vc}_{\rm op}(\mathbf{k}+\mathbf{q}) M^{{\rm vv}\mu}_{\rm ep}(\mathbf{k}+\mathbf{q}, \mathbf{k}) M^{{\rm cc}\nu}_{\rm ep}(\mathbf{k}+\mathbf{q}, \mathbf{k}) M^{\rm cv}_{\rm op}(\mathbf{k}) \left[f(E^{\rm v}_{\mathbf{k}}) - f(E^{\rm c}_{\mathbf{k}}) \right]}{(E_{\rm L} - E^{\rm cv}_{\mathbf{k}} - i\gamma)(E_{\rm L} - E^{\rm c}_{\mathbf{k}+\mathbf{q}} + E^{\rm v}_{\mathbf{k}} - \omega^\nu_{-\mathbf{q}} - i\gamma)(E_{\rm L} - E^{\rm cv}_{\mathbf{k}+\mathbf{q}} - \omega^\nu_{-\mathbf{q}} - \omega^\mu_{\mathbf{q}} - i\gamma)}. \tag{4.3}$$

The minus sign in Eq. (4.3) corresponds to the opposite charge of the hole from the electron in the hole-phonon matrix elements [78].

4.2 Kohn anomaly effect of second-order Raman spectra

In Sec. 3.2 we discussed the $\mathbf{q} = 0$ Kohn anomaly process which leads to phonon renormalization of the G band. In this section, we compare the KA process for $\mathbf{q} = 0$ and $\mathbf{q} \approx$ K as shown in Figs. 4-2(a) and (b), respectively. In the $\mathbf{q} = 0$ KA, a phonon with energy $\omega^{(0)}$

Fig. 4-2: fig/ch4-KA2.eps

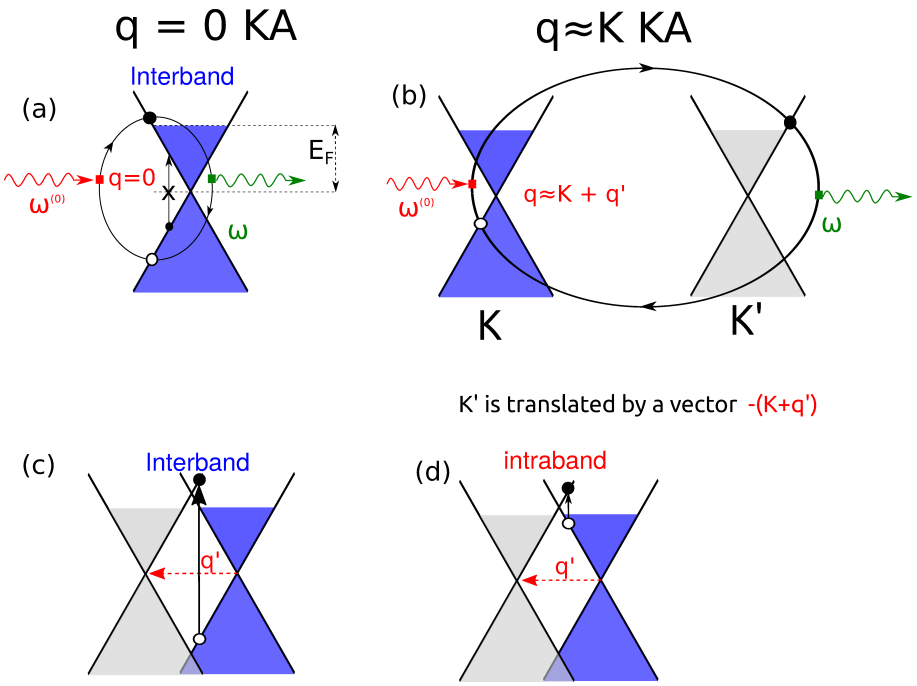

Figure 4-2: (Color online) (a) A schematic of the $\mathbf{q} = 0$ Kohn anomaly process. A phonon with zero wave vector ($\mathbf{q} = 0$) and energy $\omega^{(0)}$ vertically excites an electron-hole pair via the electron-phonon interaction. The electron-hole pair then recombines by emitting a phonon with energy ω. (b) A schematic of the $\mathbf{q} \approx$ K Kohn anomaly process. An electron exists at the K′ point leaving a hole behind at the K point with a distance in reciprocal space of $\mathbf{q} = \mathrm{K} + \mathbf{q}'$. If the K′ point is then translated by a vector $-(\mathbf{K} + \mathbf{q}')$, we can then imagine a virtual vertical transition of electron and hole. When $E_\mathrm{F} \neq 0$, both interband (c) and intraband (d) transitions are expected.

vertically excites an electron-hole pair via the electron-phonon interaction [Fig. 4-2(a)]. The electron-hole pair then recombines by emitting a phonon with energy ω. In this process, only interband electron-hole pair excitation is allowed at verticall transition ($\mathbf{q} = 0$). In the $\mathbf{q} \approx$ K KA, on the other hand, an electron exists at the K′ point, leaving a hole behind at the K point with a distance in reciprocal space $\mathbf{q} = \mathrm{K} + \mathbf{q}'$ [Fig. 4-2(b)]. If the K′ point is translated by a vector $-(\mathbf{K} + \mathbf{q}')$, we can imagine a virtually vertical excitation of an electron-hole pair as shown in Fig. 4-2(c) and (d). When $E_\mathrm{F} \neq 0$, both the interband [Fig. 4-2(c)] and intraband [Fig. 4-2(d)] transitions are expected.

In Fig. 4-3, we show the calculated results of the $\mathbf{q} \neq 0$ KA effect from Eq. (3.4). First, let

Fig. 4-3: fig/ch4-KAef.eps

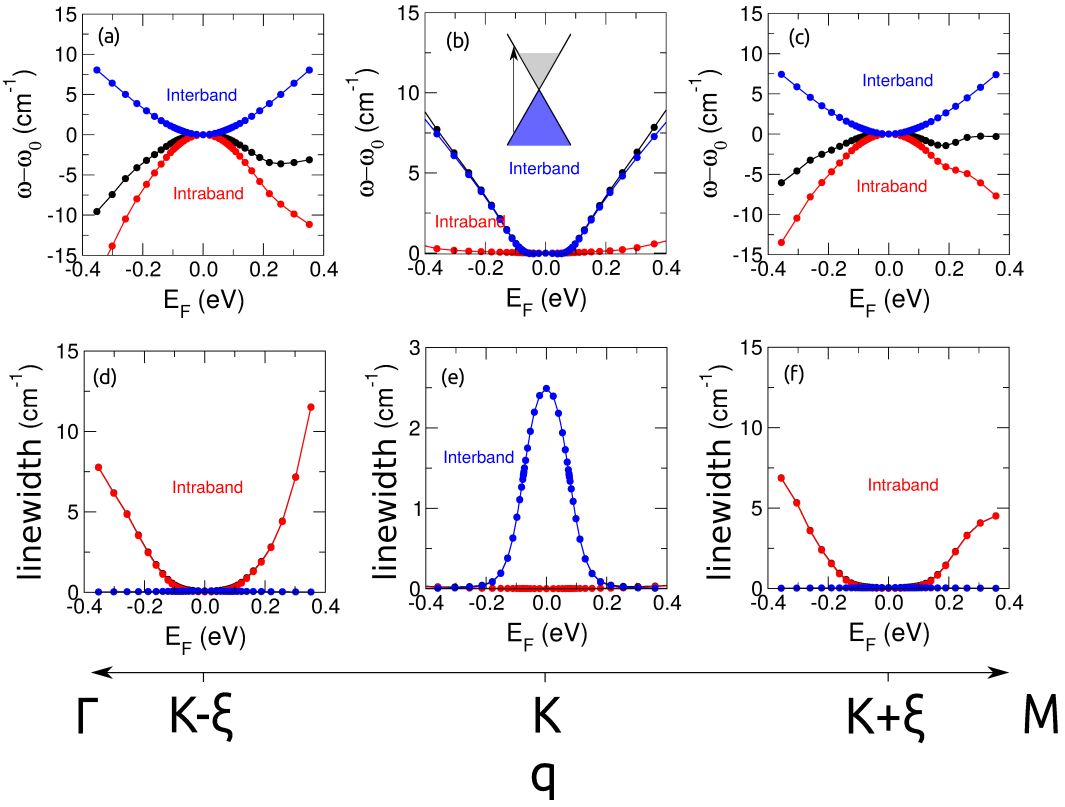

Figure 4-3: (Color online) The iTO phonon energy shift and linewidth as a function of the Fermi energy $E_{\rm F}$ for (a), (d) $\mathbf{q} = \mathrm{K} - \xi$; (b), (e) $\mathbf{q} = \mathrm{K}$; and (c), (f) $\mathbf{q} = \mathrm{K} + \xi$, with $\xi = 0.14$ Å^{-1}. We use $T = 300$ K.

us consider the case of $\mathbf{q} = \mathrm{K}$ in Figs. 4-3(b) and (e). If we compare respectively Figs. 4-3(b) and (e) with Figs. 3-2(b) and (c), both the frequency shift and phonon linewidth show the same trends as that of $\mathbf{q} = 0$ KA because both $\mathbf{q} = 0$ and $\mathbf{q} = \mathrm{K}$ are dominated by the interband electron-hole excitation. The reason why the interband excitation is dominant at $\mathbf{q} = \mathrm{K}$, is that the K and K$'$ points coincide upon translation of the K$'$ point by a vector $-\mathrm{K}$ [$\mathbf{q}' = 0$ in Fig. 4-2(c)]. Therefore, at the $\mathbf{q} = \mathrm{K}$ KA, only virtually vertical interband excitation, the same as at $\mathbf{q} = 0$ KA, is possible [79]. The previous work did not consider the interband contribution, therefore assigning the $\mathbf{q} = \mathrm{K}$ phonon frequency shift to be dispersionless as a function of $E_{\rm F}$ [33].

Next, if we shift by $\xi = 0.14$ Å^{-1} from $\mathbf{q} = \mathrm{K}$, competition between the intraband and interband excitations take place as shown in Figs. 4-3(a), (c), (d), and (f). According to the

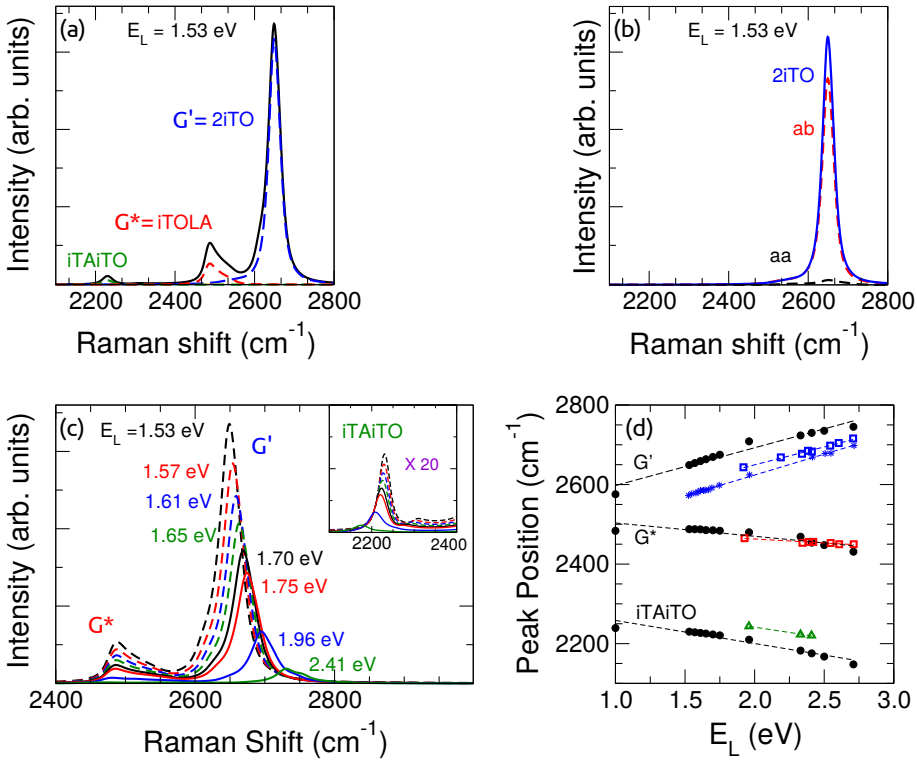

Figure 4-4: (Color online) (a) The calculated results of the second-order Raman intensity for a laser energy 1.53 eV showing three significant peaks identified with the iTA+iTO band ($\sim$ 2200 cm^{-1}), iTO+LA or G* band ($\sim$ 2500 cm^{-1}), and 2iTO or 2D or G$'$ band ($\sim$ 2800 cm^{-1}). (b) The constituents of the G$'$ band contribution from (a): $ab = (A^{\rm eh} + A^{\rm he})$ (blue dashed line) and $aa = (A^{\rm ee} + A^{\rm hh})$ (red dashed line). (c) The calculated results of the $E_{\rm L}$ dependence of the G$'$, G*, and iTA + iTO bands (inset) for $1.53\,{\rm eV} \le E_{\rm L} \le 2.41\,{\rm eV}$. (d) The G$'$, G*, and iTA + iTO bands peak position as a function of $E_{\rm L}$. Black dots are the calculated results (this work), blue and red open squares are from Ref. [21], blue asterisks are from Ref. [80], and green triangles are from Ref. [81].

analytical formula [79], the intraband contribution to the frequency shift is proportional to $-\sin^{-1}|2E_{\rm F}/vq|$ by assuming $\omega_0 \ll vq$, where v is the slope of the linear energy dispersion of graphene which is ~ 6.46 eVÅ. The phonon linewidth is increasing linearly with $|E_{\rm F}|$ in the case of the intraband excitation [Figs. 4-3(d) and (f)] because the electron-phonon scattering rate is proportional to the carrier concentration. The asymmetry at positive and negative $E_{\rm F}$ is related to electron-hole band asymmetry considered in the tight binding calculation.

After considering the KA effect on the $\mathbf{q} \neq 0$ phonon, in Fig 4-4 we show the calculated

Fig. 4-4: fig/ch4-elgp.eps

Table 4.1: Summary of the second-order Raman peak position as a function of $E_{\rm L}$.

Mode	Peak[a] ($\rm cm^{-1}$) this work	Peak[a] ($\rm cm^{-1}$) expermients	$\Delta\omega/\Delta E_{\rm L}$($\rm cm^{-1}/\,eV$) this work	$\Delta\omega/\Delta E_{\rm L}$($\rm cm^{-1}/\,eV$) experiments
G′	2730	2683 [21], 2668 [80]	95	90 [21], 104 [80]
G*	2456	2456 [21]	-33	-20 [21]
iTA+iTO	2176	2220 [81]	-58	-56 [81]

[a] Data are taken at $E_{\rm L} = 2.41\,\rm eV$

Raman spectra from Eq. (4.1). Figure 4-4(a) shows three bands, respectively, assigned as the G′ $\sim 2700\ \rm cm^{-1}$, G* $\sim 2500\ \rm cm^{-1}$, and iTA + iTO $\sim 2240\ \rm cm^{-1}$ for $E_{\rm L} = 1.53\,\rm eV$. We confirm the origin of the G′ bands from the overtone of the iTO (2iTO) modes while the G* bands come from a combination of iTO and LA modes. The major contributions to the G′ intensity come from the $A^{\rm eh}$ and $A^{\rm he}$ terms as shown by $ab = (A^{\rm eh} + A^{\rm he})$ in Fig. 4-4(b). This confirms the previous calculation that the $A^{\rm ee}$ and $A^{\rm hh}$ terms are negligible [$aa = (A^{\rm ee} + A^{\rm hh})$ in Fig. 4-4(b)] because of the quantum interference effect during the **k** integration [70].

Figure 4-4(c) shows the second-order Raman intensities for $1.53\,\rm eV \le E_{\rm L} \le 2.41\,eV$. The intensities of all these Raman bands are inversely proportional to $E_{\rm L}$ because of the increase of the electron-phonon scattering rate γ as a function of $E_{\rm L}$ [70, 20]. Assuming that each band can be represented by a single peak, the peak positions of the G′, G*, and iTA + iTO bands as a function of $E_{\rm L}$ are shown in Fig. 4-4(d). The results Fig. 4-4(d) are summarized in the Table 4.1. Good agreement between theory and experiment in the slope of the $E_{\rm L}$ dispersion indicates the reliability of our phonon dispersion used in the calculation. However, discrepancies with the experiments for the peak position of the G′ and iTA + iTO bands of about 50 $\rm cm^{-1}$ show that the calculated electronic energy dispersion underestimates the experimenal results. This can be seen insofar as the G′ and iTA + iTO peaks at $E_{\rm L} = 1.5\,\rm eV$ in theory give relatively the same value for $E_{\rm L} = 2.0\,\rm eV$ in the experiment, thus the present electronic energy dispersion near $E_{\rm L}$ underestimate the real value by $\sim 0.5\,\rm eV$. This might be because we neglect the many body and exciton effects in the band calculations [see Fig. 2-4]. Nevertheless, the overal agreement is sufficient for us to proceed and consider the $E_{\rm F}$

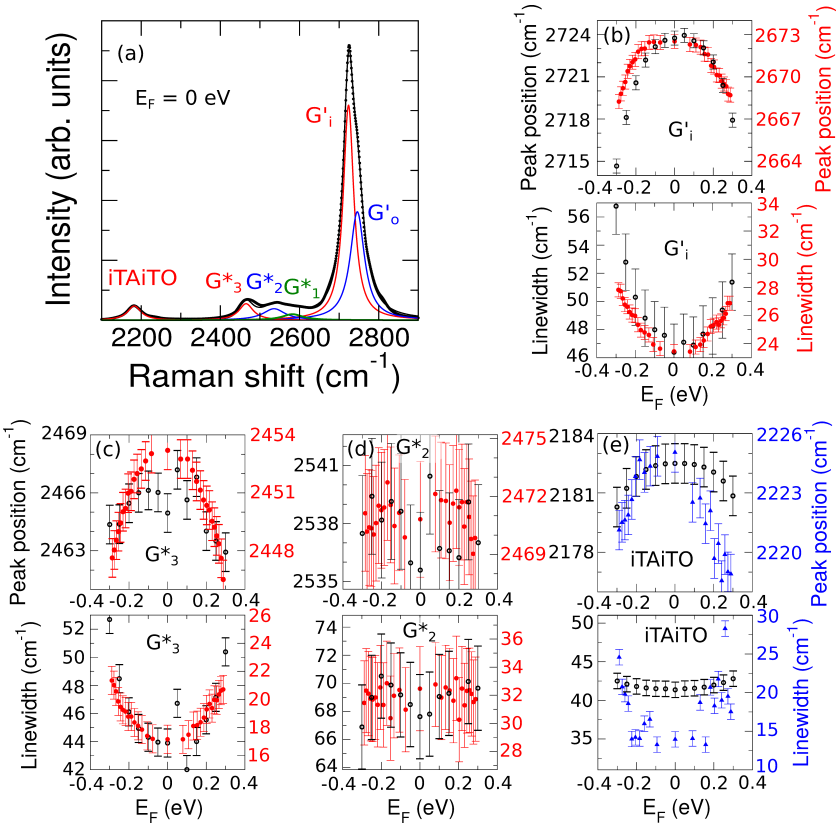

Figure 4-5: (Color online) (a) Fitting of the second order Raman spectra obtained in Fig. 4-6(a) at $E_{\rm F} = 0\,{\rm eV}$ and $E_{\rm L} = 2.33\,{\rm eV}$. The dotted line is the calculated Raman intensity fitted by six Lorentzians labelled by G'_o (blue), G'_i (red), G^*_1 (green), G^*_2 (blue), G^*_3 (red), and iTA + iTO bands. We show the peak shift and the spectral linewidth as a function of $E_{\rm F}$ for (b) the G'_i, (c) G^*_3, (d) G^*_2, and (e) iTA + iTO bands. Black open circles are the results in this work, red closed circles are experimental results from Ref. [33], and blue triangles are experimental results from Ref. [37].

dependence of the Raman intensity for a particular $E_{\rm L}$.

Figure 4-5(a) shows the Lorentzian fitting results on the second order Raman spectra for $E_{\rm F} = 0$. The dotted line is the calculated Raman intensity fitted by six Lorentzians. We fit the G′ bands with two Lorentzians labelled by G'_o (blue) and G'_i (red) which reffer to G′ bands from outer (**q** in KM direction) and inner (**q** in KΓ direction) scattering processes, respectively [70, 80]. Three Lorentzians are needed to fit the G* band, labelled by G^*_1 (green), G^*_2 (blue), and G^*_3 (red). Finally one Lorentzian is used to fit the iTA + iTO band.

Fig. 4-5: fig/ch4-KAexp.eps

After Lorentzian fitting, we compare both the peak shift and the spectral linewidth as a function of $E_{\rm F}$ as shown in Figs. 4-5(b)-(e). We do not show the $\mathrm{G'}_o$ and G_1^* for simplicity because there is no experimental data available for comparison. The calculated results in Fig. 4-5(b)-(e) cannot fit the experimental value of both the peak position and the linewidth due to the underestimation of the electronic energy dispersion as previously discussed in the $E_{\rm L}$ dependence of the second-order Raman spectra [see Fig. 4-4(d)]. But we can discuss the change of both quantities as a function of $E_{\rm F}$, where the KA effect takes place. In Figs. 4-5(b)-(e), both the spectral peak position and the linewidth as a function of $E_{\rm F}$ are plotted in the same range, comparing the theory and experiments. Reasonable agreements between experiments and theory are achieved. The three major peaks, i.e., the $\mathrm{G'}_i$, G_3^*, and iTA + iTO bands show "Λ" ("V") shapes of the Raman peak shift (spectral linewidth) as a function of $E_{\rm F}$. These behaviors exist because of the intraband electron-hole excitation renormalization of phonons as shown in Fig. 4-3. The G_2^* band in Fig. 4-5(d) is relatively dispersionless in $E_{\rm F}$ because it is located in the shoulder of the G$'$ band where 2iTO $\mathbf{q} = \mathrm{K}$ exists. Therefore, for these bands, the competition between interband and intraband electron-hole excitations are expected. The calculated results overestimate the experimental spectral linewidths of all bands, which is related to the choice of $\Delta\mathbf{k}$ in the $\mathbf{k}$ integration. We can tackle this issue by reducing the value of $\Delta\mathbf{k}$ by $\Delta\mathbf{k}/n$; however, the computational burden becomes e^n times larger.

4.3 Quantum interference effect of second-order Raman spectra

Figure 4-6(a) shows the evolution of the second-order Raman spectra for several values of $E_{\rm F}$. We use the same $E_{\rm L} = 2.33\,\mathrm{eV}$ as Araujo *et al* [33]. In Figs. 4-6(b) and (c) the intensities have been multiplied by two times as indicated. Figures 4-6(a) and (d) show the decrease of the G$'$ peak intensity as $|E_{\rm F}|$ increases. In Fig. 4-6(d), the calculated results shown circles

Fig. 4-6: fig/ch4-QI.eps

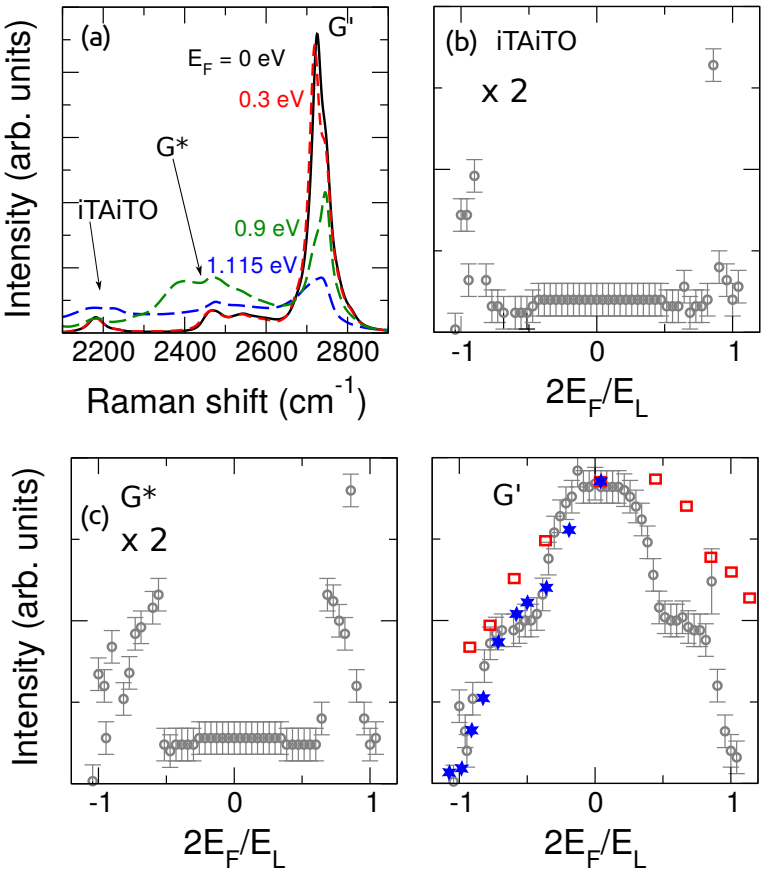

Figure 4-6: (Color online) (a) The second-order Raman spectra for several E_{F}. (b) The iTA + iTO, (c) the G*, and (d) the G$'$ band intensities as a function of $2E_{\mathrm{F}}/E_{\mathrm{L}}$, where $E_{\mathrm{L}} = 2.33\,\mathrm{eV}$. In panels (b) and (c) the intensities have been multiplied by two times as indicated in the figures. In panel (d), calculated results are represented by circles, while experimental results are denoted by stars (from Ref. [41]) and squares (from Ref. [72]).

and the experimental results (stars from Ref. [41] and squares from Ref. [72]) reasonably agree with each other. However, the Raman intensity of the iTA + iTO and G* bands dramatically increase at certain values of E_{F} as shown in Fig. 4-6(b) and (c), respectively. We find that the intensity increase of the combination phonon modes (iTA + iTO and G* bands) originates from the electron-phonon matrix elements effect to the phase of Raman spectra.

In Fig. 4-7(a), we plot $M_{\mathrm{ep}}^{\mathrm{vv\ LA}}(\mathbf{k}+\mathbf{q},\mathbf{k})M_{\mathrm{ep}}^{\mathrm{cc\ iTO}}(\mathbf{k}+\mathbf{q},\mathbf{k})$ for $\mathbf{k}$ is given on a equi–energy line $E_{\mathbf{k}}^{\mathrm{c}} - E_{\mathbf{k}}^{\mathrm{v}} = 1\,\mathrm{eV}$ near the K point and $\mathbf{q} = \mathrm{K}$. We can see that both real and imaginary

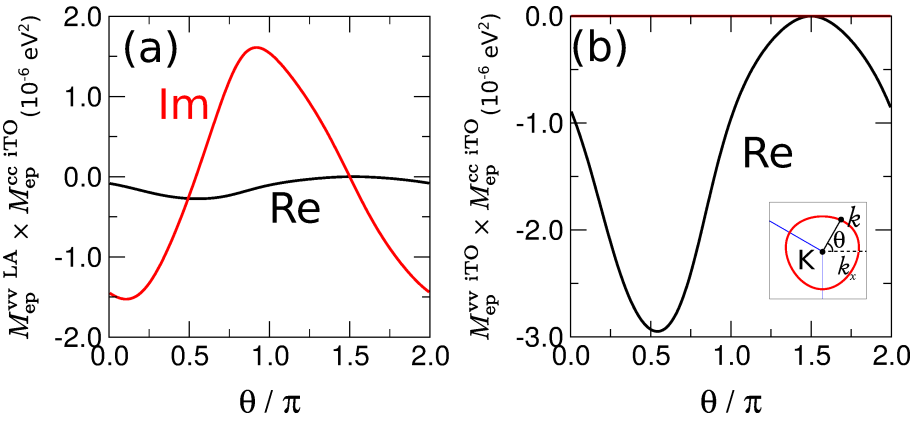

Figure 4-7: (Color online) Product of electron-phonon matrix elements (a) $M_{\rm ep}^{\rm vv\ LA}(\mathbf{k}+\mathbf{q},\mathbf{k})M_{\rm ep}^{\rm cciTO}(\mathbf{k}+\mathbf{q},\mathbf{k})$ and (b)$M_{\rm ep}^{\rm vv\ iTO}(\mathbf{k}+\mathbf{q},\mathbf{k})M_{\rm ep}^{\rm cciTO}(\mathbf{k}+\mathbf{q},\mathbf{k})$ with $\mathbf{q}=$ K as a function of angle θ measured from $\mathbf{k}_x$-axis. Inset: equi–energy line for $E_{\mathbf{k}}^{\rm c}-E_{\mathbf{k}}^{\rm v}=1\,$eV near the K point and definition of θ and $\mathbf{k}_x$.

parts of the product of matrix elements exist indicating the change of phase as a function of $\mathbf{k}$. At a finite $E_{\rm F}$, some of these destructive phases are suppressed due to the Pauli exclusion principle, as a result the Raman intensity for the combination phonon modes are enhanced. On the other hand, the overtone mode does not provide such a destructive phase because μ and ν are the same thus two matrix elements are related by a complex conjugation and the product of the two values gives only a real value as shown in Fig. 4-7(b).

These results give clues about how the Raman phase governed by the electron-phonon matrix elements distinguishes between the $E_{\rm F}$ dependence of the Raman intensity of the combination modes from that of the overtone modes [72, 82]. Although $E_{\rm F}\approx 1\,$eV is too high for experiments on graphene, one can reduce the $E_{\rm L}$ to become $\approx 1\,$eV to satisfy the condition of $2E_{\rm F}\approx E_{\rm L}$ to get proper conditions for observing the quantum interference effect.

Fig. 4-7: fig/ch4-mepmep.eps

Chapter 5

Conclusion

In conclusion, we calculated the first- and second-order Raman spectra of graphene as a function of the Fermi energy (E_{F}). The calculation of Raman spectra of graphene requires knowledge of electronic energy dispersion, phonon energy dispersion, the electron-photon, electron-phonon, and electron-electron interactions. The calculation results of the E_{F} dependence of Raman spectra are used to explain three phenomena observed in the gate modulated Raman experiments: (1) the Kohn anomaly effect, (2) the quantum interference effect, and (3) the asymmetric Breit-Wigner-Fano lineshape of Raman spectra.

Kohn anomaly effect

The Kohn anomaly (KA) effect of the first-order Raman spectra comes from renormalization of phonon energy by the interband electron-hole excitation. In contrast to the KA effect of the first-order Raman spectra, the intraband electron-hole excitation dominates over the KA effect of the second-order Raman spectra. Because of these two different effects arising from the interband and intraband excitations, the opposite Kohn anomaly effect, in terms of phonon frequency and linewidth as a function of E_{F}, between the first- and second-order Raman spectra was observed by Araujo et al. [33] and has been confimed by the present calculation. We reproduce the slopes of both phonon frequency and linewidth as a function of E_{F} for both the first- and second-order Raman spectra. In particular, from the present

calculation, the $\mathbf{q} = 0$ and $\mathbf{q} = \mathrm{K}$ phonons are found to have the same KA effect [Fig. 4-3] but Araujo et al. assign that the G_2^* band which is non-dispersive in E_F comes from the $\mathbf{q} = \mathrm{K}$ phonon [33]. We argue that the origin of non-dispersive G_2^* band comes from mixture of many $\mathbf{q}$ phonons in which the competition between interband and intraband excitations are balanced in the KA effect.

Quantum interference effect

We also discussed the quantum interference effect observed in the change of the Raman intensity as a function of E_F. Both the first- and the second-order Raman spectra exhibit an impact of the quantum interference effect, especially when $2|E_\mathrm{F}| \approx E_\mathrm{L}$. The first-order Raman spectra are found to have destructive interference between the incident and scattered resonance. When $2E_\mathrm{F}$ is very close to E_L, the scattered resonant condition can be suppressed while keeping the incident resonance, the G band intensity enhancement can be achieved. Present calculated results found that not only the resonance conditions are important, but also the explicit consideration of the electron-phonon matrix elements are essential to determine the E_F dependence of the Raman spectral lineshape. In the first-order Raman spectra, different peak intensity between hole and electron doping observed by Liu et al. [72] has been reproduced by the present calculation because we consider electron-hole asymmetry in graphene electronic energy dispersion [Fig. 3-4]. In the second-order Raman spectra, the appearance of two electron-phonon matrix elements gives two different quantum interference effect for the overtone and combination modes. The overtone mode (G' band) gives monotonically decreasing intensity while the intensities of combination modes (G^* and iTA + iTO bands) are enhanced by two times when $2E_\mathrm{F} \approx E_\mathrm{L}$ (Fig. 4-6). The present calculated results have never been observed systematically in experiments thus require confirmations.

Breit-Wigner-Fano lineshape

We have shown that the origin of the Breit-Wigner-Fano (BWF) spectra in the G band of graphene comes from the continuous ERS spectra interfering with the discrete G band

phonon spectra. By calculating the Raman amplitudes of the ERS and phonon spectra, we found that the interference effect between the ERS and phonon spectra gives a drastic change in the constructive-destructive interference near the phonon frequency, leading to an asymmetry of the phonon lineshape when fitted to the BWF lineshape. In this calculation we found that the first-order ERS process has smaller probability compared with the second-order one because the direct Coulomb interaction vanishes at $\mathbf{q} = 0$ due to the symmetry of electron wavefunctions in the A and B sites of graphene unit cell. Considering the second-order Raman process for the ERS spectra, we were able to reproduce the E_{F} dependence of the asymmetric BWF factor $1/q_{\mathrm{BWF}}$ [Fig. 3-8]. We expect that the asymmetric BWF feature appears generally in the phonon Raman spectra of all Dirac cone systems.

Appendix A

Determination of Force Constant Parameters

In this section we review Samsonidze's Ph.D. thesis for determining the force constant parameters for the extended interatomic potential up to the 20–th nearest neighbor [58]. First we discuss the basic force constant (BFC) model by taking into account the contribution up to the fourth nearest neighbor. Since the BFC model is not sufficient to reproduce experimental results, we improve the BFC by considering up to the 20–th nearest neighbor in the advanced force constant (AFC) model with the force constant parameters are obtained from the first-principles calculation [63].

A.1 Basic force-constant model

The lattice dynamics of the graphene sheet is described by the equation of motion, Eq. (2.29), with the dynamical matrix of Eq. (2.35) expressed through the interatomic force constants, $\mathcal{K}^{js\alpha}_{j's'\alpha'}$. The interatomic force constants $\mathcal{K}^{js\alpha}_{j's'\alpha'}$ are written in the form of the 3×3 force constant matrix $\Phi_{j's'js}$ over the coordinates α', α defined by $(\Phi_{j's'js})_{\alpha'\alpha} = \mathcal{K}^{js\alpha}_{j's'\alpha'}$ for each pair $j's'js$ of carbon atoms. We first construct the force constant matrices using the normal coordinates $\alpha', \alpha = ir, it, ot$, corresponding to the in-plane radial, in-plane tangential, and

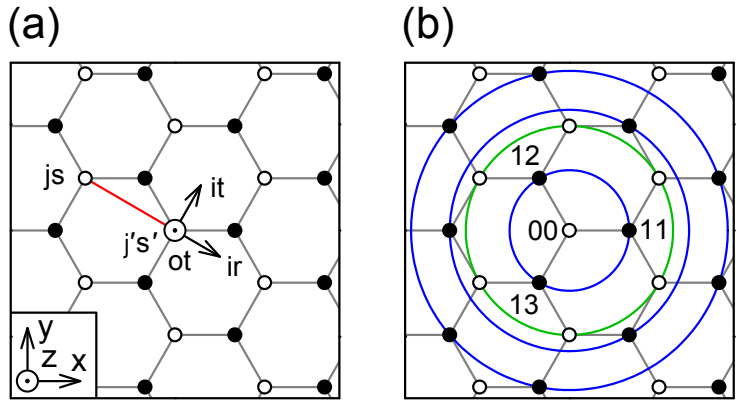

Figure A-1: A single graphene sheet where the open and solid dots indicate the A and B sublattices, respectively. (a) The normal coordinates (ir, it, ot) for a pair of js and $j's'$ atoms are connected by the red line. The dotted points represent the vectors ot and z pointing out of the image plane. (b) The four shells of the nearest neighbors of the central A atom are shown by circles. The shells that consist of the A and B atoms are shown in green and blue, respectively. The central A atom and the three B atoms from the first shell are labeled by indices $\imath\jmath = 00$ and $\imath\jmath = 11, 12, 13$, respectively.

out-of-plane tangential displacements of carbon atoms, as shown in Fig. A-1 (a). Then we transform the force constant matrices from $\Phi^{\rm norm}_{j's'js}$ in the normal coordinates to $\Phi^{\rm cart}_{j's'js}$ in the Cartesian coordinates by means of rotation matrices.

We consider the force constants up to the fourth nearest neighbor within the basic force-constant (BFC) model [83]. The inclusion of the fourth nearest neighbor is essential in order to describe the twisted motion of carbon atoms [83]. Within the BFC framework, we further neglect off-diagonal elements of the force constant matrices in the normal coordinates [83].

The four shells of the nearest neighbors of atom A are shown by the circles in Fig. A-1 (b). Note that the first, third, and fourth shells consist of atoms B of the opposite type than the central A atom, while the same A atoms appear in the second shell. Each atom within the four shells is labeled by a pair of indices, $\imath\jmath$ instead of js, where $\imath = 1, \ldots, 4$ indicates the shell number and $\jmath$ numerates the atoms in each shell counterclockwise looking down the z-axis. The first atom $\jmath = 1$ within each shell $\imath$ appears in the positive direction of the x-axis. The indices $\imath\jmath = 11, 12, 13$ for the first shell $\imath = 1$ are shown in Fig. A-1 (b). The central A

Fig. A-1: fig/ap1-4th.eps

atom is referred by $\imath\jmath = 00$ instead of $j's'$. The indices $\imath\jmath = 00$ for the central atom are shown in Fig. A-1 (b). In this notation, the force constant matrices $\Phi_{j's'js}$ and the force constants $\mathcal{K}^{js\alpha}_{j's'\alpha'}$ are written as $\Phi_{00\imath\jmath}$ and $\mathcal{K}^{\imath\jmath\alpha}_{00}$, respectively. In the normal coordinates $\alpha = ir, it, ot$, the force constants $\mathcal{K}^{\imath\jmath\alpha}_{00}$ within each shell $\imath$ are equivalent. Thus, $\mathcal{K}^{\imath\jmath\alpha}_{00}$ is independent of index $\jmath$, and so does $\Phi^{\rm norm}_{00\imath\jmath}$. Hence, we label $\mathcal{K}^{\imath\jmath\alpha}_{00}$ as $\mathcal{K}^{(\imath)}_{\alpha}$, assuming $\alpha = ir, it, ot$.

For the pairs of atoms $00\imath\jmath$, the normal coordinate system is rotated by the angles $\phi_{00\imath\jmath}$ from the Cartesian coordinate system around the common axis $ot = z$, as one can see in Fig. A-1 (a). The force constant matrices in the normal coordinates:

$$\Phi^{\rm norm}_{00\imath\jmath} = \begin{pmatrix} \mathcal{K}^{(\imath)}_{ir} & 0 & 0 \\ 0 & \mathcal{K}^{(\imath)}_{it} & 0 \\ 0 & 0 & \mathcal{K}^{(\imath)}_{ot} \end{pmatrix} \tag{A.1}$$

are then transformed to Cartesian coordinates by means of the rotation matrix $R^z\left(\phi_{00\imath\jmath}\right)$ given by

$$R^z(\phi_{00js}) = \begin{pmatrix} \cos\phi_{00js} & \sin\phi_{00js} & 0 \\ -\sin\phi_{00js} & \cos\phi_{00js} & 0 \\ 0 & 0 & 1 \end{pmatrix} . \tag{A.2}$$

and its transpose ${R^z}^{\rm T}(\phi_{00\imath\jmath})$:

$$\Phi^{\rm cart}_{00\imath\jmath} = {R^z}^{\rm T}(\phi_{00\imath\jmath})\Phi^{\rm norm}_{00\imath\jmath}R^z(\phi_{00\imath\jmath})\,. \tag{A.3}$$

Upon substituting Eq. (A.2) into Eq. (A.3), we obtain the force constant matrices in Cartesian coordinates:

$$\Phi^{\rm cart}_{00\imath\jmath} = \begin{pmatrix} \mathcal{K}^{(\imath)}_{ir}\cos^2\phi_{00\imath\jmath} + \mathcal{K}^{(\imath)}_{it}\sin^2\phi_{00\imath\jmath} & \left(\mathcal{K}^{(\imath)}_{ir} - \mathcal{K}^{(\imath)}_{it}\right)\cos\phi_{00\imath\jmath}\sin\phi_{00\imath\jmath} & 0 \\ \left(\mathcal{K}^{(\imath)}_{ir} - \mathcal{K}^{(\imath)}_{it}\right)\cos\phi_{00\imath\jmath}\sin\phi_{00\imath\jmath} & \mathcal{K}^{(\imath)}_{ir}\sin^2\phi_{00\imath\jmath} + \mathcal{K}^{(\imath)}_{it}\cos^2\phi_{00\imath\jmath} & 0 \\ 0 & 0 & \mathcal{K}^{(\imath)}_{ot} \end{pmatrix} . \tag{A.4}$$

For the first shell of the nearest neighbors $\imath\jmath = 11, 12, 13$, the rotation angles are given

by $\phi_{0011} = \pi$, $\phi_{0012} = -\pi/3$, and $\phi_{0013} = \pi/3$, according to Fig. A-1 (b). Upon substituting these angles into Eq. (A.4), we obtain the force constant matrices in Cartesian coordinates:

$$\Phi_{0011}^{\text{cart}} = \begin{pmatrix} \mathcal{K}_{ir}^{(\imath)} & 0 & 0 \\ 0 & \mathcal{K}_{it}^{(\imath)} & 0 \\ 0 & 0 & \mathcal{K}_{ot}^{(\imath)} \end{pmatrix}, \tag{A.5}$$

$$\Phi_{0012}^{\text{cart}} = \begin{pmatrix} \frac{1}{4}\mathcal{K}_{ir}^{(1)} + \frac{3}{4}\mathcal{K}_{it}^{(1)} & -\frac{\sqrt{3}}{4}\left(\mathcal{K}_{ir}^{(1)} - \mathcal{K}_{it}^{(1)}\right) & 0 \\ -\frac{\sqrt{3}}{4}\left(\mathcal{K}_{ir}^{(1)} - \mathcal{K}_{it}^{(1)}\right) & \frac{3}{4}\mathcal{K}_{ir}^{(1)} + \frac{1}{4}\mathcal{K}_{it}^{(1)} & 0 \\ 0 & 0 & \mathcal{K}_{ot}^{(1)} \end{pmatrix}, \tag{A.6}$$

$$\Phi_{0013}^{\text{cart}} = \begin{pmatrix} \frac{1}{4}\mathcal{K}_{ir}^{(1)} + \frac{3}{4}\mathcal{K}_{it}^{(1)} & \frac{\sqrt{3}}{4}\left(\mathcal{K}_{ir}^{(1)} - \mathcal{K}_{it}^{(1)}\right) & 0 \\ \frac{\sqrt{3}}{4}\left(\mathcal{K}_{ir}^{(1)} - \mathcal{K}_{it}^{(1)}\right) & \frac{3}{4}\mathcal{K}_{ir}^{(1)} + \frac{1}{4}\mathcal{K}_{it}^{(1)} & 0 \\ 0 & 0 & \mathcal{K}_{ot}^{(1)} \end{pmatrix}. \tag{A.7}$$

In a similar fashion, the force constant matrices for the shells $\imath = 2, 3, 4$ and those for the central B atom are transformed to Cartesian coordinates using Eq. (A.4). The resulting force constant matrices multiplied by the appropriate phase factors build up the dynamical matrix, according to Eq. (2.35). Thus, the dynamical matrix within the BFC model is determined by 12 force constant parameters $\mathcal{K}_{\alpha}^{(\imath)}$ with $\imath = 1, \ldots, 4$ and $\alpha = ir, it, ot$.

A.2 Advanced force-constant model

The BFC model is not sufficient to accurately reproduce the phonon dispersion curves of the graphene sheet observed experimentally. The advanced force-constant (AFC) model is thus introduced. The AFC model involves twenty shells of nearest neighbors and off-diagonal matrix elements of the force constant matrices. The twenty shells and off-diagonal elements are essential in order to reproduce the phonon dispersion relations of the graphene sheet obtained from first-principles calculations on the basis of density-functional theory (DFT) employing the local-density approximation (LDA) for the exchange-correlation potential with a plane-

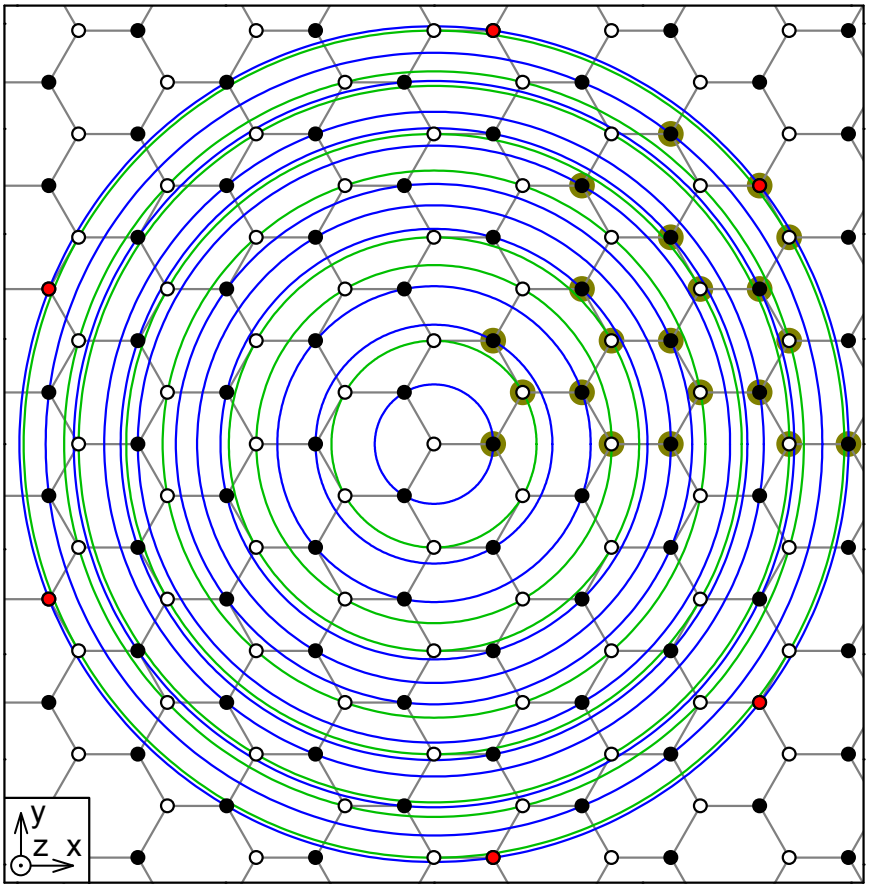

Figure A-2: The twenty shells of the nearest neighbors of the central A atom are shown by the circles. The shells that consist of the A and B atoms are shown in green and blue, respectively. The B atoms that form the shell 20′ are shown by red dots. The atoms in each shell are numbered counterclockwise looking down the z-axis. The first atom within each shell is highlighted by a yellow background.

wave expansion of the wavefunctions and using pseudo-potentials for the core electrons [63].

The twenty shells of the nearest neighbors of atom A are shown by circles in Fig. A-2, where the first four shells coincide with those in Fig. A-1 (b). The shells 1, 3, 4, 7, 8, 9, 11, 13, 14, 16, 18, 20 consist of atoms B of the opposite type than the central A atom, while the shells 2, 5, 6, 10, 12, 15, 17, 19 contain atoms A of the same type. Note that there are two different types of atoms in shell 20, which we refer to as 20 and 20′, shown by black and

Fig. A-2: fig/ngb20.eps

red dots in Fig. A-2, respectively. By analogy with the BFC model discussed in Section A.1, each atom within the twenty shells is labeled by a pair of indices $\imath\jmath$, where $\imath = 1, \ldots, 20$ indicates the shell number and $\jmath$ numerates the atoms in each shell counterclockwise looking down the z-axis. The first atom $\jmath = 1$ within each shell $\imath$ appears in the positive direction of the x-axis. These atoms are highlighted by a yellow background in Fig. A-2. The central A atom is referred by $\imath\jmath = 00$.

Let us construct the force constant matrices in the normal coordinates $\Phi^{\mathrm{norm}}_{00\imath\jmath}$. The diagonal matrix elements of $\Phi^{\mathrm{norm}}_{00\imath\jmath}$ are given by $\mathcal{K}^{(\imath)}_{ir}$, $\mathcal{K}^{(\imath)}_{it}$, and $\mathcal{K}^{(\imath)}_{ot}$, similar to Eq. (A.1) for the BFC model. The out-of-plane off-diagonal matrix elements of $\Phi^{\mathrm{norm}}_{00\imath\jmath}$ are zero. The in-plane off-diagonal matrix elements of $\Phi^{\mathrm{norm}}_{00\imath\jmath}$, on the other hand, are determined by the symmetry of the pairs of atoms shown in Fig. A-2. For the shells $\imath = 1, 3, 5, 8, 11, 15, 20$, the in-plane off-diagonal matrix elements of $\Phi^{\mathrm{norm}}_{00\imath\jmath}$ vanish. For the shells $\imath = 2, 4, 6, 7, 9, 12, 13, 14, 16, 18, 19, 20'$, there is one independent in-plane off-diagonal matrix element of $\Phi^{\mathrm{norm}}_{00\imath\jmath}$, which we refer to as $\mathcal{K}^{(\imath)}_{i1}$. For the shells $\imath = 10, 17$, there are two independent in-plane off-diagonal matrix elements of $\Phi^{\mathrm{norm}}_{00\imath\jmath}$, which we refer to as $\mathcal{K}^{(\imath)}_{i1}$ and $\mathcal{K}^{(\imath)}_{i2}$. The in-plane diagonal blocks of the force constant matrices $\Phi^{\mathrm{norm}}_{00\imath\jmath}$ are then written in the following form:

$$
\begin{cases}
\left(\Phi^{\mathrm{norm}}_{00\imath\jmath}\right)_{ii} = \begin{pmatrix} +\mathcal{K}^{(\imath)}_{ir} & 0 \\ 0 & +\mathcal{K}^{(\imath)}_{it} \end{pmatrix} & \text{for} \quad \begin{cases} \imath = 1,3,8,11,20, \\ \jmath = 1,2,3, \end{cases} \\
\left(\Phi^{\mathrm{norm}}_{00\imath\jmath}\right)_{ii} = \begin{pmatrix} +\mathcal{K}^{(\imath)}_{ir} & 0 \\ 0 & +\mathcal{K}^{(\imath)}_{it} \end{pmatrix} & \text{for} \quad \begin{cases} \imath = 5,15, \\ \jmath = 1,2,3,4,5,6, \end{cases} \\
\left(\Phi^{\mathrm{norm}}_{00\imath\jmath}\right)_{ii} = \begin{pmatrix} +\mathcal{K}^{(\imath)}_{ir} & +\mathcal{K}^{(\imath)}_{i1} \\ -\mathcal{K}^{(\imath)}_{i1} & +\mathcal{K}^{(\imath)}_{it} \end{pmatrix} & \text{for} \quad \begin{cases} \imath = 2,6,12,19, \\ \jmath = 1,3,5, \end{cases} \\
\left(\Phi^{\mathrm{norm}}_{00\imath\jmath}\right)_{ii} = \begin{pmatrix} +\mathcal{K}^{(\imath)}_{ir} & -\mathcal{K}^{(\imath)}_{i1} \\ +\mathcal{K}^{(\imath)}_{i1} & +\mathcal{K}^{(\imath)}_{it} \end{pmatrix} & \text{for} \quad \begin{cases} \imath = 2,6,12,19, \\ \jmath = 2,4,6, \end{cases} \\
\left(\Phi^{\mathrm{norm}}_{00\imath\jmath}\right)_{ii} = \begin{pmatrix} +\mathcal{K}^{(\imath)}_{ir} & +\mathcal{K}^{(\imath)}_{i1} \\ +\mathcal{K}^{(\imath)}_{i1} & +\mathcal{K}^{(\imath)}_{it} \end{pmatrix} & \text{for} \quad \begin{cases} \imath = 4,7,9,13,14,16,18,20', \\ \jmath = 1,3,5, \end{cases} \\
\left(\Phi^{\mathrm{norm}}_{00\imath\jmath}\right)_{ii} = \begin{pmatrix} +\mathcal{K}^{(\imath)}_{ir} & -\mathcal{K}^{(\imath)}_{i1} \\ -\mathcal{K}^{(\imath)}_{i1} & +\mathcal{K}^{(\imath)}_{it} \end{pmatrix} & \text{for} \quad \begin{cases} \imath = 4,7,9,13,14,16,18,20', \\ \jmath = 2,4,6, \end{cases} \\
\left(\Phi^{\mathrm{norm}}_{00\imath\jmath}\right)_{ii} = \begin{pmatrix} +\mathcal{K}^{(\imath)}_{ir} & +\mathcal{K}^{(\imath)}_{i1} \\ +\mathcal{K}^{(\imath)}_{i2} & +\mathcal{K}^{(\imath)}_{it} \end{pmatrix} & \text{for} \quad \begin{cases} \imath = 10,17, \\ \jmath = 1,5,9, \end{cases} \\
\left(\Phi^{\mathrm{norm}}_{00\imath\jmath}\right)_{ii} = \begin{pmatrix} +\mathcal{K}^{(\imath)}_{ir} & -\mathcal{K}^{(\imath)}_{i1} \\ -\mathcal{K}^{(\imath)}_{i2} & +\mathcal{K}^{(\imath)}_{it} \end{pmatrix} & \text{for} \quad \begin{cases} \imath = 10,17, \\ \jmath = 4,8,12, \end{cases} \\
\left(\Phi^{\mathrm{norm}}_{00\imath\jmath}\right)_{ii} = \begin{pmatrix} +\mathcal{K}^{(\imath)}_{ir} & +\mathcal{K}^{(\imath)}_{i2} \\ +\mathcal{K}^{(\imath)}_{i1} & +\mathcal{K}^{(\imath)}_{it} \end{pmatrix} & \text{for} \quad \begin{cases} \imath = 10,17, \\ \jmath = 3,7,11, \end{cases} \\
\left(\Phi^{\mathrm{norm}}_{00\imath\jmath}\right)_{ii} = \begin{pmatrix} +\mathcal{K}^{(\imath)}_{ir} & -\mathcal{K}^{(\imath)}_{i2} \\ -\mathcal{K}^{(\imath)}_{i1} & +\mathcal{K}^{(\imath)}_{it} \end{pmatrix} & \text{for} \quad \begin{cases} \imath = 10,17, \\ \jmath = 2,6,10, \end{cases}
\end{cases}
\tag{A.8}
$$

while the out-of-plane diagonal blocks are given by $\left(\Phi^{\mathrm{norm}}_{00\imath\jmath}\right)_{oo} = \mathcal{K}^{(\imath)}_{ot}$, and the off-diagonal blocks $\left(\Phi^{\mathrm{norm}}_{00\imath\jmath}\right)_{io}$ and $\left(\Phi^{\mathrm{norm}}_{00\imath\jmath}\right)_{oi}$ vanish. The force constant matrices $\Phi^{\mathrm{norm}}_{00\imath\jmath}$ given by Eq. (A.8)

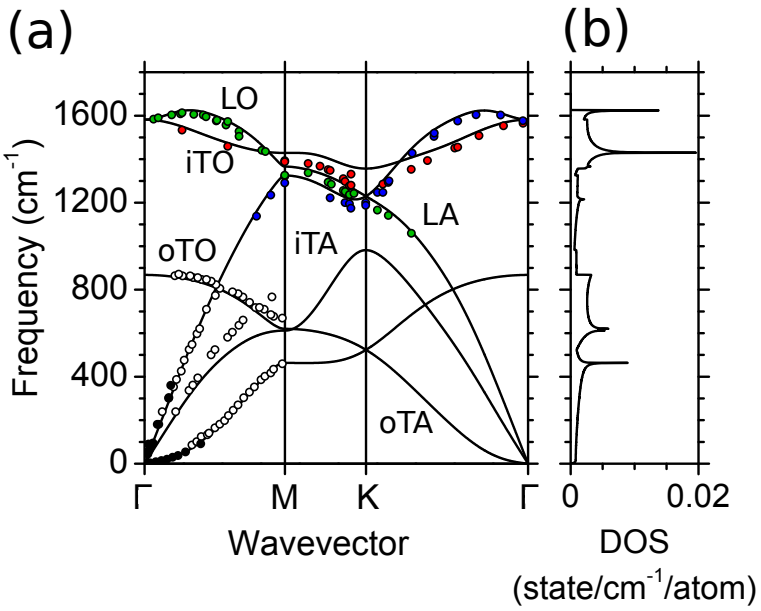

Figure A-3: (a) Phonon dispersion relations of a graphene sheet according to the AFC model with the force constants [63] given in Table A.1 along the high-symmetry directions in the first Brillouin zone. The red, green, blue, solid, and open dots are experimental data taken from Ref. [31, 30]. (b) The density of phonon states (DOS).

are then transformed from the normal coordinates to Cartesian coordinates using Eq. (A.4). The force constant matrices for the central B atom are obtained in a similar fashion. The resulting force constant matrices multiplied by the appropriate phase factors build up the dynamical matrix, according to Eq. (2.35). Thus, the dynamical matrix within the AFC model is determined by 79 force constant parameters $\mathcal{K}_{\alpha}^{(\imath)}$, where $\alpha = ir, it, ot$ for $\imath = 1, 3, 5, 8, 11, 15, 20$, $\alpha = ir, it, ot, i1$ for $\imath = 2, 4, 6, 7, 9, 12, 13, 14, 16, 18, 19, 20'$, and $\alpha = ir, it, ot, i1, i2$ for $\imath = 10, 17$. The force constant parameters within the framework of the AFC model calculated with the help of DFT-LDA [63] are summarized in Table A.1. The phonon dispersion relations of the graphene sheet calculated with the force constants from Table A.1 are shown in Fig. A-3.

Fig. A-3: fig/ldagr.eps

Table A.1: The force constants for a graphene sheet within the AFC model (in units of $10^4\,\mathrm{dyn/cm}$; $1\,\mathrm{dyn/cm} = 6.2415\,\mathrm{meV/nm^2}$) calculated with the help of DFT-LDA [63]. The in-plane and out-of-plane force constants are scaled by factors 0.9915^2 and 0.9754^2, respectively, in order to fit the Γ point optical phonon frequencies to the well-known experimental data $\omega^{E_{2g}}(\Gamma) = 1582\,\mathrm{cm}^{-1}$ and $\omega^{B_{2g}}(\Gamma) = 868\,\mathrm{cm}^{-1}$ [87]. The corresponding phonon dispersion relations are shown in Fig. A-3.

	$\mathcal{K}_{ir}$	$\mathcal{K}_{it}$	$\mathcal{K}_{ot}$	$\mathcal{K}_{i1}$	$\mathcal{K}_{i2}$
$\mathcal{K}^{(1)}$	+43.0374	+16.0741	+9.6310	—	—
$\mathcal{K}^{(2)}$	+7.3805	−4.1183	−0.7718	+0.4415	—
$\mathcal{K}^{(3)}$	−1.3043	+3.1505	+0.6341	—	—
$\mathcal{K}^{(4)}$	−0.6390	+0.3681	−0.7535	+1.0211	—
$\mathcal{K}^{(5)}$	+0.8245	+0.1673	+0.1058	—	—
$\mathcal{K}^{(6)}$	+0.1737	−0.4310	−0.0180	−0.0109	—
$\mathcal{K}^{(7)}$	−0.3062	+0.2356	−0.0127	+0.1669	—
$\mathcal{K}^{(8)}$	−0.7099	+0.0203	+0.0982	—	—
$\mathcal{K}^{(9)}$	+0.0128	+0.1167	+0.0395	−0.0512	—
$\mathcal{K}^{(10)}$	+0.1764	−0.0838	−0.0099	+0.2299	−0.0940
$\mathcal{K}^{(11)}$	−0.1364	+0.1983	+0.0029	—	—
$\mathcal{K}^{(12)}$	+0.0975	+0.0096	+0.0020	−0.0306	—
$\mathcal{K}^{(13)}$	−0.0496	−0.0335	−0.0063	+0.0356	—
$\mathcal{K}^{(14)}$	−0.1200	−0.0283	−0.0127	+0.0542	—
$\mathcal{K}^{(15)}$	+0.1428	+0.0212	+0.0020	—	—
$\mathcal{K}^{(16)}$	−0.0835	+0.0220	+0.0028	−0.0073	—
$\mathcal{K}^{(17)}$	+0.0301	−0.0203	+0.0006	+0.0246	−0.0069
$\mathcal{K}^{(18)}$	−0.0687	+0.0220	−0.0010	+0.0330	—
$\mathcal{K}^{(19)}$	+0.0426	−0.0141	+0.0002	+0.0000	—
$\mathcal{K}^{(20)}$	−0.1368	−0.0552	+0.0028	—	—
$\mathcal{K}^{(20')}$	−0.0120	+0.0104	+0.0020	+0.0033	—

Appendix B

Electron-Electron Interaction

In this section we elaborate the calculation of electron-electron interaction $K_{1,2,3,4}(\mathbf{q})$, where $[1,2,3,4] = [\mathbf{k}\mathrm{c}, \mathbf{k}'\mathrm{v}, (\mathbf{k}-\mathbf{q})\mathrm{c}, (\mathbf{k}'+\mathbf{q})\mathrm{c}]$ within tight binding (TB) approximation. An important conclusion of this section is that for the direct Coulomb interaction K^{d} between the photo-excited electron (PE) and an electron in the Dirac cone (DE) vanishes at $\mathbf{q}=0$ which give rise to the smaller amplitude of the first-order ERS process $A^{(1)}_{\mathrm{ERS}}$ when compared to the second-order $A^{(2)}_{\mathrm{ERS}}$ counterpart. This is simply due to the symmetry of the A and B sublattice in graphene unit cell. The interaction between a photoexcited electron (PE) from state 1 to state 3 in the conduction band and an electron in the Dirac cone (DE) from state 2 to state 4 is given by

$$K_{1,2,3,4}(\mathbf{q}) = \int d\mathbf{r} d\mathbf{r}' \Phi^{*(\pm)}_{34}(\mathbf{r},\mathbf{r}') v\left(\mathbf{r},\mathbf{r}'\right) \Phi^{(\pm)}_{12}(\mathbf{r},\mathbf{r}'). \tag{B.1}$$

The two-body wave function of electrons in a initial state $\Phi^{(\pm)}_{12}$ is defined as:

$$\Phi^{(\pm)}_{12}(\mathbf{r},\mathbf{r}') = \frac{1}{\sqrt{2}}\left[\psi_1\left(\mathbf{r}\right)\psi_2\left(\mathbf{r}'\right) \pm \psi_1\left(\mathbf{r}'\right)\psi_2\left(\mathbf{r}\right)\right], \tag{B.2}$$

and the final state $\Phi_{34}^{(\pm)}$ is defined as:

$$\Phi_{34}^{(\pm)}(\mathbf{r},\mathbf{r}') = \frac{1}{\sqrt{2}}\left[\psi_3(\mathbf{r})\,\psi_4(\mathbf{r}') \pm \psi_3(\mathbf{r}')\,\psi_4(\mathbf{r})\right], \tag{B.3}$$

where the $+\,(-)$ sign is taken for the spin singlet (triplet) state. Here we do not explicitly show spins functions for simplicity since the Coulomb interaction does not change the spin direction. $\psi_i(\mathbf{r})$ is the tight binding wavefunction in Eq. (2.4) specified by wave vector $\mathbf{k}_i$, subband $a_i = \mathrm{c},\ \mathrm{v}$, and position $\mathbf{r}$.

Substituting Eqs. (B.2) and (B.3) into Eq. (B.1) we obtain

$$K_{1,2,3,4}(\mathbf{q}) = K^{\mathrm{d}}_{1,2,3,4}(\mathbf{q}) \pm K^{\mathrm{x}}_{1,2,3,4}(\mathbf{q}), \tag{B.4}$$

where the direct interaction K^{d} and exchange interaction K^{x} terms are expressed by

$$K^{\mathrm{d}}_{1,2,3,4}(\mathbf{q}) = \frac{1}{2}(V_{1,2,3,4} + V_{2,1,4,3}), \tag{B.5}$$

$$K^{\mathrm{x}}_{1,2,3,4}(\mathbf{q}) = \frac{1}{2}(V_{1,2,4,3} + V_{2,1,3,4}), \tag{B.6}$$

and the Coulomb integral K is defined by

$$V_{1,2,3,4} = \int d\mathbf{r}d\mathbf{r}' v(\mathbf{r},\mathbf{r}')\,\psi_4^*(\mathbf{r}')\,\psi_3^*(\mathbf{r})\,\psi_2(\mathbf{r}')\,\psi_1(\mathbf{r}). \tag{B.7}$$

Substituting Eq. (2.4) into Eq. (B.7), we get

$$\begin{aligned} V_{1,2,3,4} =& \frac{1}{N^2}\sum_{s_1u_1,s_2u_2}\Bigg[\sum_{s_1'u_1',s_2'u_2'} C^{a_1*}_{s_1}(\mathbf{k}_1)\,e^{-i\mathbf{k_1}.\mathbf{R}_{u_1s_1}} C^{a_2*}_{s_1'}(\mathbf{k}_2)\,e^{-i\mathbf{k_2}.\mathbf{R}_{u_1's_1'}} \\ &\times C^{a_3}_{s_2}(\mathbf{k}_3)\,e^{i\mathbf{k_3}.\mathbf{R}_{u_2s_2}} C^{a_4}_{s_2'}(\mathbf{k}_4)\,e^{i\mathbf{k_4}.\mathbf{R}_{u_2's_2'}} \\ &\times \int d\mathbf{r}d\mathbf{r}' v(\mathbf{r},\mathbf{r}')\,\varphi(\mathbf{r}-\mathbf{R}_{u_1s_1})\,\varphi\left(\mathbf{r}'-\mathbf{R}_{u_1's_1'}\right)\varphi(\mathbf{r}-\mathbf{R}_{u_2s_2})\,\varphi\left(\mathbf{r}'-\mathbf{R}_{u_2's_2'}\right)\Bigg]. \end{aligned} \tag{B.8}$$

The largest contribution from the integrand comes from $(u_1s_1) = (u_2s_2) \equiv (us)$ and $(u_1's_1') =$

$(u'_2 s'_2) \equiv (u's')$. Thus Eq. (B.8) becomes

$$\begin{aligned} V_{1,2,3,4} &\cong \frac{1}{N^2}\sum_{su}\sum_{s'u'} C_s^{a_1 *}(\mathbf{k}_1) C_{s'}^{a_2 *}(\mathbf{k}_2) C_s^{a_3}(\mathbf{k}_3) C_{s'}^{a_4}(\mathbf{k}_4) \\ &\quad \times e^{-i\mathbf{k_1}.\mathbf{R}_{us}} e^{-i\mathbf{k_2}.\mathbf{R}_{u's'}} e^{i\mathbf{k_3}.\mathbf{R}_{us}} e^{i\mathbf{k_4}.\mathbf{R}_{u's'}} \\ &\quad \times \int d\mathbf{r} d\mathbf{r}' v(\mathbf{r},\mathbf{r}') \left|\varphi(\mathbf{r}-\mathbf{R}_{us})\right|^2 \left|\varphi(\mathbf{r}'-\mathbf{R}_{u's'})\right|^2 \\ &= \frac{1}{N^2}\sum_{su}\sum_{s'u'} C_s^{a_1 *}(\mathbf{k}_1) C_{s'}^{a_2 *}(\mathbf{k}_2) C_s^{a_3}(\mathbf{k}_3) C_{s'}^{a_4}(\mathbf{k}_4) \\ &\quad \times e^{i(\mathbf{k_3}-\mathbf{k_1}).\mathbf{R}_{us}} e^{i(\mathbf{k_4}-\mathbf{k_2}).\mathbf{R}_{u's'}} \\ &\quad \times \int d\mathbf{r} d\mathbf{r}' v(\mathbf{r},\mathbf{r}') \left|\varphi(\mathbf{r}-\mathbf{R}_{us})\right|^2 \left|\varphi(\mathbf{r}'-\mathbf{R}_{u's'})\right|^2 \\ &= \frac{1}{N^2}\sum_{su}\sum_{s'u'} C_s^{a_1 *}(\mathbf{k}_1) C_{s'}^{a_2 *}(\mathbf{k}_2) C_s^{a_3}(\mathbf{k}_3) C_{s'}^{a_4}(\mathbf{k}_4) \\ &\quad e^{i(\mathbf{k_3}-\mathbf{k_1}+\mathbf{k_4}-\mathbf{k_2}).\mathbf{R}_{us}} e^{i(\mathbf{k_4}-\mathbf{k_2}).(\mathbf{R}_{u's'}-\mathbf{R}_{us})} \\ &\quad \times \int d\mathbf{r} d\mathbf{r}' v(\mathbf{r},\mathbf{r}') \left|\varphi(\mathbf{r}-\mathbf{R}_{us})\right|^2 \left|\varphi(\mathbf{r}'-\mathbf{R}_{u's'})\right|^2 . \end{aligned}$$

By using the fact that $\sum_{u,s} e^{i(\mathbf{k_3}-\mathbf{k_1}+\mathbf{k_4}-\mathbf{k_2}).\mathbf{R}_{us}} = N\delta(\mathbf{k_3}+\mathbf{k_4},\mathbf{k_1}+\mathbf{k_2})$, we get

$$\begin{aligned} V_{1,2,3,4} &= \sum_{ss'} C_s^{a_1 *}(\mathbf{k}_1) C_{s'}^{a_2 *}(\mathbf{k}_2) C_s^{a_3}(\mathbf{k}_3) C_{s'}^{a_4}(\mathbf{k}_4) v_{ss'}(\mathbf{k_4}-\mathbf{k_2}) \\ &\quad \times\delta(\mathbf{k_3}+\mathbf{k_4},\mathbf{k_1}+\mathbf{k_2}), \end{aligned} \tag{B.9}$$

where

$$v_{ss'}(\mathbf{q}) = \frac{1}{N}\sum_{u'} e^{i\mathbf{q}.(\mathbf{R}_{u's'}-\mathbf{R}_{0s})} \int d\mathbf{r} d\mathbf{r}' v(\mathbf{r},\mathbf{r}') \left|\varphi(\mathbf{r}-\mathbf{R}_{0s})\right|^2 \left|\varphi(\mathbf{r}'-\mathbf{R}_{u's'})\right|^2, \tag{B.10}$$

is the Fourier transform of the Coulomb integral. When we define the integration of Eq. (B.10) as $v(\mathbf{R}_{0s},\mathbf{R}_{u's'})$,

$$v_{ss'}(\mathbf{q}) = \frac{1}{N}\sum_{u'} e^{i\mathbf{q}.(\mathbf{R}_{u's'}-\mathbf{R}_{0s})} v(\mathbf{R}_{0s},\mathbf{R}_{u's'}), \tag{B.11}$$

we can show that $v_{\mathrm{AA}}(\mathbf{q}) = v_{\mathrm{BB}}(\mathbf{q})$ and $v_{\mathrm{AB}}(\mathbf{q}) = v^{*}_{\mathrm{BA}}(\mathbf{q})$ because of the symmetry between the A and B sublattices. The Coulomb potential $v(\mathbf{R}, \mathbf{R}')$ for the π electron system is modeled by the Ohno potential [75, 76, 38]:

$$v(\mathbf{R}, \mathbf{R}') = \frac{U_0}{\sqrt{\left(\frac{4\pi\epsilon_0}{e^2} U_0 \left|\mathbf{R} - \mathbf{R}'\right|\right)^2 + 1}}. \tag{B.12}$$

where U_0 the on-site Coulomb potential for two π electrons at the same site $\mathbf{R} = \mathbf{R}'$, which is defined by

$$U_0 = \int d\mathbf{r} d\mathbf{r}' \varphi^2(\mathbf{r}) \varphi^2(\mathbf{r}') \frac{e^2}{\mathbf{r} - \mathbf{r}'} = 11.3 \text{ eV} \tag{B.13}$$

The corresponding direct and exchange terms from Eqs. (B.5) and (B.6) are now expressed by

$$K^{d}_{1,2,3,4}(\mathbf{q}) = \sum_{ss'=\mathrm{A,B}} C^{1}_{s} C^{2}_{s'} C^{*3}_{s} C^{*4}_{s'} \operatorname{Re}\left[v_{ss'}(\mathbf{q})\right], \tag{B.14}$$

$$K^{x}_{1,2,3,4}(\mathbf{q}) = \sum_{ss'=\mathrm{A,B}} C^{1}_{s} C^{2}_{s'} C^{*3}_{s'} C^{*4}_{s} \operatorname{Re}\left[v_{ss'}\left(\mathbf{k}' - \mathbf{k} - \mathbf{q}\right)\right]. \tag{B.15}$$

The TB coefficient C^{i}_{s} has been derived in Eq. (2.21), and choosing the phase factor ($\phi_{\mathrm{c}} = \phi_{\mathrm{v}} = -\theta(\mathbf{k})/2$) so as to get

$$\begin{aligned} C^{c}_{A}(\mathbf{K} + \mathbf{k}) &= \frac{1}{\sqrt{2}} e^{-i\theta(\mathbf{k})/2}, \quad C^{c}_{B}(\mathbf{K} + \mathbf{k}) = \frac{1}{\sqrt{2}} e^{+i\theta(\mathbf{k})/2}, \\ C^{v}_{A}(\mathbf{K} + \mathbf{k}) &= \frac{1}{\sqrt{2}} e^{-i\theta(\mathbf{k})/2}, \quad C^{v}_{B}(\mathbf{K} + \mathbf{k}) = -\frac{1}{\sqrt{2}} e^{+i\theta(\mathbf{k})/2}, \end{aligned} \tag{B.16}$$

where the phase θ in Eq. (B.16) is defined by the angle between $\mathbf{k}$ and $\mathbf{k}_{x}-$ axis measured from the K (or K') point (see Fig.B-1, vectors corresponding to the K and K$'$ points are denoted $\mathbf{K}$ and $\mathbf{K}'$, respectively) [88]. In Eq. (B.16), we have set the overlap integral $s = 0$ (Eq. (2.21)). The TB coefficient near K$'$ point can be obtain by taking complex conjugate of corresponding coefficient near K point.

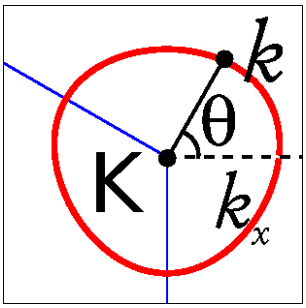

Figure B-1: The phase θ in Eq. (B.16) is defined by the angle between $\mathbf{k}$ and $\mathbf{k}_x$– axis measured from the K (or K') point.

Inserting Eqs. (B.16) and (B.11) to Eqs. (B.14) and (B.15), at $\mathbf{q} = 0$, the direct interaction term becomes

$$K^{\mathrm{d}}_{1,2,3,4}(0) = \frac{1}{4}\left(\tilde{v}_{\mathrm{AA}}\left(0\right) - \tilde{v}_{\mathrm{A}B}\left(0\right) + \tilde{v}_{\mathrm{BA}}\left(0\right) - \tilde{v}_{\mathrm{BB}}\left(0\right)\right) = 0, \tag{B.17}$$

and the exchange term becomes

$$K^{\mathrm{x}}_{1,2,3,4}(0) = \frac{i}{2}\sin\left(\theta' - \theta\right)\ \mathrm{Re}v_{\mathrm{AB}}\left(\mathbf{k}' - \mathbf{k}\right). \tag{B.18}$$

Equation (B.17) proves that the direct terms K^{d} in the first-order process at $\mathbf{q} = 0$ vanish, and only the exchange terms K^{x} in Eq. (B.18) survive. Therefore, the first-order electron-electron scattering give a very small contribution to the ERS spectra and then we must consider the second-order process.

Fig. B-1: ch2-angle.eps

Appendix C

Phase of Second-Order Raman Amplitudes

In this section, we analyze the phase of the second-order Raman amplitudes. It has been shown in Fig. 4-4(b) that the $ab = (A^{\rm eh} + A^{\rm he})$ processes are more dominant than the $aa = (A^{\rm ee} + A^{\rm hh})$ processes, thus we focus on Eq. (4.3) for evaluating the phase of the second-order Raman amplitudes. The phase of numerator of Eq. (4.3) comes from the products of electron-phonon matrix elements and has been shown in Fig. 4-7. Here, we focus on analyzing the phase of denominator of Eq. (4.3) following Chen et al. [41].

We recall the denominator of Eq. (4.3) for a given $\mathbf{k}$ as:

$$R_{\mathbf{k}} = \frac{1}{(E_{\rm L} - E_{\mathbf{k}} - i\gamma)(E_{\rm L} - E_{\mathbf{k}'} - \omega - i\gamma)(E_{\rm L} - E_{\mathbf{k}''} - 2\omega - i\gamma)}, \tag{C.1}$$

where we have used short-hand notations: $E_{\mathbf{k}} = E^{\rm cv}_{\mathbf{k}}$, $E_{\mathbf{k}'} = E^{\rm c}_{\mathbf{k+q}} - E^{\rm v}_{\mathbf{k}}$, $E_{\mathbf{k}''} = E^{\rm cv}_{\mathbf{k+q}}$, and we approximate $\omega^{\nu}_{-\mathbf{q}} = \omega^{\mu}_{\mathbf{q}} = \omega$ to simplify the analysis. From Fig. C-1, we obtain the following

Fig. C-1: ap3-gprime.eps

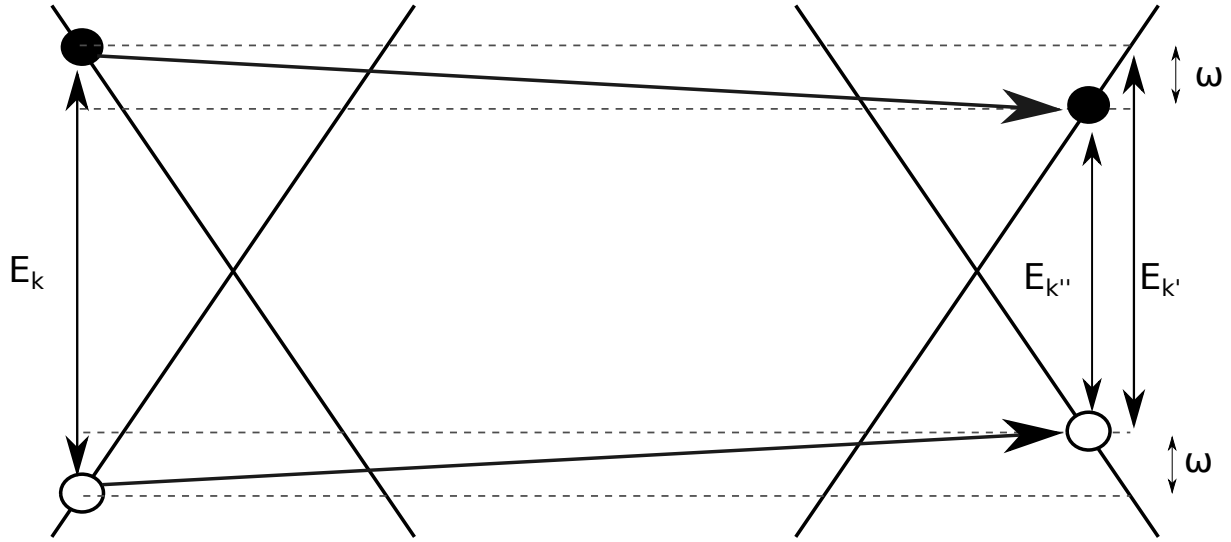

Figure C-1: Schematic of the second-order Raman process described in Eq. (4.3). We define short-hand notations: $E_{\mathbf{k}} = E^{\mathrm{cv}}_{\mathbf{k}}$, $E_{\mathbf{k}'} = E^{\mathrm{c}}_{\mathbf{k}+\mathbf{q}} - E^{\mathrm{v}}_{\mathbf{k}}$, $E_{\mathbf{k}''} = E^{\mathrm{cv}}_{\mathbf{k}+\mathbf{q}}$, and $\omega^{\nu}_{-\mathbf{q}} = \omega^{\mu}_{\mathbf{q}} = \omega$.

relationships:

$$E_{\mathbf{k}'} = E_{\mathbf{k}} - \omega, \tag{C.2}$$

$$E_{\mathbf{k}''} = E_{\mathbf{k}} - 2\omega. \tag{C.3}$$

From Eqs. (C.2) and (C.3) we shall obtain,

$$E_{\mathbf{k}''} + E_{\mathbf{k}} = 2E_{\mathbf{k}'}. \tag{C.4}$$

Substituting Eq. (C.4) into Eq. (C.1) we obtain $R_{\mathbf{k}}$ as a function of $E_{\mathbf{k}}$ and $E_{\mathbf{k}'}$:

$$R_{\mathbf{k}} = \frac{1}{(E_{\mathrm{L}} - E_{\mathbf{k}} - i\gamma)(E_{\mathrm{L}} - E_{\mathbf{k}'} - \omega - i\gamma)(E_{\mathrm{L}} - 2E_{\mathbf{k}'} + E_{\mathbf{k}} - 2\omega - i\gamma)}. \tag{C.5}$$

The dominant contribution to the Raman amplitude is obtain when one of the denominator

is minimum, namely $E_{\mathbf{k}'} = E_{\mathrm{L}} - \omega$. With this condition, Eq. (C.5) becomes:

$$R_{\mathbf{k}} = \frac{1}{(E_{\mathrm{L}} - E_{\mathbf{k}} - i\gamma)(-i\gamma)(-E_{\mathrm{L}} + E_{\mathbf{k}} - i\gamma)},$$
$$R_{\mathbf{k}} \propto \frac{1}{(E_{\mathrm{L}} - E_{\mathbf{k}})^2 - \gamma^2}. \tag{C.6}$$

From Eq. (C.6), it is clear that the denominator of Eq. (4.3) does not change the phase when $E_{\mathbf{k}}$ or E_{F} changes. This is the reason why the G′ band intensity in Figs. 4-6(a) and (d) is monotonically decreasing by increasing E_{F}.

Appendix: calculation program

There are three main programs to calculate the $E_{\rm F}$ dependence of the first-order Raman spectra, the Kohn anomaly effect, and the second-order Raman spectra. All the necessary programs can be found under the following directory in `FLEX` workstation:

`~hasdeo/for/karaman/`

Hereafter, this directory will simply be referred to as `ROOT/` directory. More detail explanations about how to use the programs are given in the `00README` file in each subdirectory of `ROOT`.

First-order Raman Spectra

Main program: `ROOT/gband/mesh-gband.f90`

Inputs: 1. input file: "nparameter.dat": provides values of $E_{\rm F}$ and $E_{\rm L}$

G band amplitudes

Subroutine: `ROOT/gband/gampli.f90` Calculate the G band amplitudes

Inputs: 1. `efermi REAL(8)` The Fermi energy

2. `kx, ky REAL(8)` Values of k_x and k_y of electron wave vector

Outputs: 1. `amplito, amplilo COMPLEX(8)` LO and iTO Raman amplitudes

Kohn anomaly effect

Program: `ROOT/kagrap/efkagrap.f90` Calculate the Kohn anomaly as a function of the Fermi energy

Outputs: 1. `selfen COMPLEX(8)` phonon self energy

Second-order Raman spectra

Main Program: `ROOT/gpband/kk-gpband.f90` Calculate the second order Raman spectra as a function of the Fermi energy

Inputs: 1. input file "nparameter.dat": provides values of E_{F} and E_{L}

Outputs: 1. output file ./data-efgband/gpintensity-$\langle E_{\mathrm{L}}\rangle$-$\langle E_{\mathrm{F}}\rangle$.dat

Publication list

Papers related to Thesis

1. **E. H. Hasdeo**, A. R. T. Nugraha, K. Sato, M. S. Dresselhaus, and R. Saito: "Electronic Raman scattering and the Fano resonance in metallic carbon nanotubes", Phys. Rev. B 88, 115107 (2013).

2. **E. H. Hasdeo**, A. R. T. Nugraha, M. S. Dresselhaus, and R. Saito: "Breit-Wigner-Fano lineshapes in Raman spectra of graphene", Phys. Rev. B 90, 245140 (2014).

3. **E. H. Hasdeo**, A. R. T. Nugraha, M. S. Dresselhaus, and R. Saito: " Fermi energy dependence of first-and second-order Raman spectra in graphene: Kohn anomaly and quantum interference effect", Phys. Rev. B 94, 075104 (2016).

Other Papers

1. **E. H. Hasdeo**, M. Nurhuda, Abdurrouf: "The Optical Low-Pass Filter Gain of a Ring Cavity", IJBAS-IJENS 01, 63-68 (2012).

2. A. R. T. Nugraha, E. Rosenthal, **E. H. Hasdeo**, G. D. Sanders C. J. Stanton, M. S. Dresselhaus, R. Saito: "Excitonic effects on coherent phonon dynamics in single wall carbon nanotubes", Phys. Rev. B 88, 075440 (2013)

3. R. Saito, A. R. T. Nugraha, **E. H. Hasdeo**, S. Siregar, H. Guo, T. Yang: "Ultraviolet

Raman spectroscopy of graphene and transition-metal dichalcogenides", Phys. Status Solidi B 252, 2363 (2015).

4. H.-L. Liu, S. Siregar, **E. H. Hasdeo**, Y. Kumamoto, C.-C. Shen, C.-C. Cheng, L.-J. Li, R. Saito, S. Kawata: "Deep-ultraviolet Raman scattering studies of monolayer graphene thin films", Carbon 81, 807-813 (2015).

5. A. R. T. Nugraha, **E. H. Hasdeo**, G. D. Sanders, C. J. Stanton, R. Saito: "Origin of coherent G-band phonon spectra in single wall carbon nanotubes", Phys. Rev. B 91, 045406 (2015).

6. M. S. Ukhtary, **E. H. Hasdeo**, A. R. T. Nugraha, R. Saito: "Fermi energy-dependence of electromagnetic wave absorption in graphene", APEX 8, 055102 -1-4, (2015).

7. N. T. Hung, A. R. T. Nugraha, **E. H. Hasdeo**, M. S. Dresselhaus, R. Saito: "Diameter dependence of thermoelectric power of semiconducting carbon nanotubes", Phys. Rev. B 92, 165426 (2015).

8. X. Ling, S. Huang, **E. H. Hasdeo**, L. Liang, W. M. Parkin, Y. Tatsumi, A. R. T. Nugraha, A. A. Puretzky, P. M. Das, B. G. Sumpter, D. B. Geohegan, J. Kong, R. Saito, M. Drndic, V. Meunier, M. S. Dresselhaus: "Anisotropic Electron-Photon and Electron-Phonon Interactions in Black Phosphorus", Nano Lett., 16 , 2260–2267 (2016).

9. P. Ayria, A. R. T. Nugraha, **E. H. Hasdeo**, T. R. Czank, S. Tanaka, R. Saito: "Photon energy dependence of angle-resolved photoemission spectroscopy in graphene", Phys. Rev. B 92, 195148 (2015).

10. D. Zhang, J. Yang, **E. H. Hasdeo**, C. Liu, K. Liu, R. Saito, Y. Li: "Multiple Electronic Raman Scatterings in a Single Metallic Carbon Nanotube", Phys. Rev. B 93, 245428 (2016).

11. N. T. Hung, **E. H. Hasdeo**, A. R. T. Nugraha, M. Dresselhaus, R. Saito: "Quantum effects on thermoelectric power factor of low-dimensional semiconductors", Phys. Rev. Lett. 117, 036602 (2016).

12. A. R. T. Nugraha, **E. H. Hasdeo**, R. Saito: "Selective coherent phonon mode generation in single wall carbon nanotubes", *submitted*.

13. M. S. Ukhtary, A. R. T. Nugraha, **E. H. Hasdeo**, R. Saito: "Broadband Transverse Electric Surface Wave in Silicene", Appl. Phys. Lett. 109, 063103 (2016).

Conferences

Oral presentations

1. A. R. T. Nugraha, **E. H. Hasdeo**, R. Saito: "Exciton effects on coherent phonon spectroscopy of carbon nanotubes", The 44th Fullerenes-Nanotubes-Graphene General Symposium, The University of Tokyo, (2013.03.11-13).

2. R. Saito, A. R. T. Nugraha, **E. H. Hasdeo**, K. Sato: "Raman spectroscopy of metallic single wall nanotubes and doped graphene (invited)", 4th A3 Symposium on Emerging Materials: Nanomaterials for Energy and Electronics, Daemyung Resort, Jeju, Korea, (2013.11.10-14).

3. R. Saito, K. Sato, **E. H. Hasdeo**, A. R. T. Nugraha: "Coherent phonon and Raman spectroscopy of single wall carbon nanotubes (invited)", Building blocks for carbon-based electronics: from molecules to nanotubes, University of Regensburg, (2013.4.10-12).

4. R. Saito, **E. H. Hasdeo**, A. R. T. Nugraha: "Exciton effects on coherent phonon and electronic Raman spectroscopy of single wall carbon nanotubes (invited)", 5th Workshop on Nanotube Optics and Nanospectroscopy, Eldorado Hotel, Santa Fe, NM, USA, (2013.6.16-20).

5. A. R. T. Nugraha, **E. H. Hasdeo**, R. Saito: "Coherent phonon spectra of G band in single wall carbon nanotubes", NT14: The Fifteenth International Conference on the Science and Application of Nanotubes, University of Southern California, Los Angeles, USA, (2014.06.02-06).

6. **E. H. Hasdeo**, A. R. T. Nugraha, M. S. Dresselhaus, R. Saito: "Quantum interference effect in Raman spectra of metallic nanotubes", NT14: The Fifteenth International Conference on the Science and Application of Nanotubes, University of Southern California, Los Angeles, USA, (2014.06.02-06).

7. R. Saito, **E. H. Hasdeo**, K. Sato, H. H. Guo: "Raman spectroscopy of graphene and atomic layer materials (invited)", RIEC symposium on Graphene, Tohoku University, (2014.6.11).

8. A. R. T. Nugraha, **E. H. Hasdeo**, R. Saito, G. D. Sanders, C. Stanton: "Coherent G band phonons in single wall carbon nanotubes", ATI 2014 Nano-Carbon Meeting, Yamagata-Zao, (2014.7.31-8.1).

9. **E. H. Hasdeo**, A. R. T. Nugraha, R. Saito: "Asymmetric lineshape in G band Raman spectra of graphene", ATI 2014 Nano-Carbon Meeting, Yamagata-Zao, (2014.7.31-8.1).

10. R. Saito, A. R. T. Nugraha, **E. H. Hasdeo**, S. Siregar, M. S. Ukhtary: "Raman and coherent phonon spectroscopy of carbon nanotubes and graphene (invited)", Materials Research Society of Indonesia Meeting 2014, Aston Denpasar Hotel and Convention Center, Bali, Indonesia, (2014.9.26-28).

11. A. R. T. Nugraha, **E. H. Hasdeo**, R. Saito: "Origin of coherent phonons in single wall carbon nanotubes", Materials Research Society of Indonesia Meeting 2014, Aston Denpasar Hotel and Convention Center, Bali, Indonesia, (2014.9.26-28).

12. R. Saito, **E. H. Hasdeo**, S. Siregar, H. Guo, T. Yang: "Raman spectra of Graphene and transition metal dichalcogenides (invited)", The 5th A3 Symposium on Emerging Materials, Nankai University, China, (2014.10.19-21).

13. R. Saito, **E. H. Hasdeo**, K. Sato, S. Siregaar, H. H. Guo, T. Yang: "Raman spectroscopy of graphene and transition metal dichalcogenides atomic layer (invited)", Physics and Chemistry of Atomic Films: Fundamental Science and Applications, Jawaharlal Nehru Centre for Advanced Scientific Research, Bangalore, India, (2014.11.4-8).

14. Ahmad R. T. Nugraha, **E. H. Hasdeo**, R. Saito: "Coherent and squeezed phonons in single wall carbon nanotubes", The 48th Fullerenes-Nanotubes-Graphene General Symposium, The University of Tokyo, (2015.2.21-23).

15. R. Saito, **E. H. Hasdeo**, A. R. T. Nugraha, H. Guo, T. Yang, S. Siregar: "Raman spectroscopy of graphene and transition metal dichalcogenides (invited)", 29th International Winterschool on Electronic Properties of Novel Materials: "Molecular nanostructures", Kirchberg, Austria, (2015.3.7-14).

16. **E. H. Hasdeo**, A. R. T. Nugraha, R. Saito: "Interplay of electron-phonon and electron-electron interactions in gate modulated Raman spectroscopy of graphene", CCTN15: The Tenth International Symposium on Computational Challenges and Tools for Nanotubes, Nagoya University, Japan, (2015.06.28).

17. R. Saito, M. S. Ukhtary, **E. H. Hasdeo**, A. R. T. Nugraha, C. Reynolds: "Tunable absorption of electromagnetic wave at graphene interface between two dieletcric materials (invited)", 6th RIEC-RLE meeting on research collaboration in photonics, Sendai, (2015.10.26).

18. R. Saito, Y. Tatsumi, A. R. T. Nugraha, **E. H. Hasdeo**, H. L. Liu, H. Guo, T. Yang: "Raman spectra of transition metal dichalcogenides and phosphorene (invited)", 6th A3 symposium on Emerging Materials, Kyushu University, Fukuoka, (2015.11.9-11).

19. R. Saito, M. S. Uktahry, A. R. T. Nugraha, **E. H. Hasdeo**, C. Reynolds: "Tunable absorption of electromagnetic wave of graphene (invited)", CEMS Topical meeting on Emergent 2D Materials, Riken, Wako, (2015.12.12).

Poster Presentations

1. **E. H. Hasdeo**, A. R. T. Nugraha, K. Sato, R. Saito: "Theory of electronic Raman scattering in metallic single-walled carbon nanotube", The 43th Fullerenes-Nanotubes-Graphene General Symposium, Tohoku University, Sendai, (2012.9.5-7).

2. A. R. T. Nugraha, E. Rosenthal, **E. H. Hasdeo**, R. Saito: "Exciton effects on coherent phonons in single wall carbon nanotubes", 2012 A3 Symposium of Emerging Materials: Nanomaterials for Energy and Environments - ATI International Forum, Tohoku University, Sendai, Japan, (2012.10.29-31).

3. **E. H. Hasdeo**, A. R. T. Nugraha, K. Sato, R. Saito: "Theory of electronic Raman scattering in metallic single wall carbon nanotubes", 2012 A3 Symposium of Emerging Materials: Nanomaterials for Energy and Environments - ATI International Forum, Tohoku University, Sendai, Japan, (2012.10.29-31).

4. **E. H. Hasdeo**, A. R. T. Nugraha, K. Sato, R. Saito: "Electronic Raman scattering and origin of the Fano resonance in metallic carbon nanotubes", The 44th Fullerenes-Nanotubes-Graphene General Symposium, The University of Tokyo, (2013.03.11-13).

5. R. Saito, **E. H. Hasdeo**, A. R. T. Nugraha, K. Sato, M. S. Dresselhaus: "Electronic Raman spectra and origin of Fano resonance in metallic single-wall carbon nanotubes", 14th International Conference on the Science and Applications of Nanotubes (NT13), Dipoli Congress Center, Aalto University, Espoo, Finland, (2013.6.24-28).

6. A. R. T. Nugraha, **E. H. Hasdeo**, R. Saito: "Exciton effects on coherent phonon dynamics in single wall carbon nanotubes", 4th A3 Symposium on Emerging Materials: Nanomaterials for Energy and Electronics, Daemyung Resort, Jeju, Korea, (2013.11.10-14).

7. **E. H. Hasdeo**, A. R. T. Nugraha, R. Saito: "Quantum interference effect in Raman spectra of metallic nanotubes", 4th A3 Symposium on Emerging Materials: Nanomaterials for Energy and Electronics, Daemyung Resort, Jeju, Korea, (2013.11.10-14).

8. A. R. T. Nugraha, **E. H. Hasdeo**, R. Saito: "Coherent G-band phonons in single wall carbon nanotubes", The 46th Fullerenes-Nanotubes-Graphene General Symposium, The University of Tokyo, (2014.3.3-5).

9. **E. H. Hasdeo**, A. R. T. Nugraha, R. Saito: "Quantum interference effect in Raman spectra of metallic nanotubes and graphene", The 46th Fullerenes-Nanotubes-Graphene General Symposium, The University of Tokyo, (2014.3.3-5).

10. S. Siregar, **E. H. Hasdeo**, A. R.T. Nugraha, R. Saito: "Absence of Raman G′ band By Ultraviolet Excitation in Monolayer Graphene Systems", The 47th Fullerenes-Nanotubes-Graphene General Symposium, Nagoya University, (2014.9.3-5).

11. P. Ayria, A. R.T. Nugraha, **E. H. Hasdeo**, R. Saito: "Polarization Dependence of ARPES Intensity in Graphene", The 47th Fullerenes-Nanotubes-Graphene General Symposium, Nagoya University, (2014.9.3-5).

12. M. S. Ukhtary, **E. H. Hasdeo**, A. R. T. Nugraha, R. Saito: "Propagation Properties of Graphene Surface Plasmon", The 47th Fullerenes-Nanotubes-Graphene General Symposium, Nagoya University, (2014.9.3-5).

13. A. R. T. Nugraha, **E. H. Hasdeo**, R. Saito: "Coherent G-band and RBM Phonons in Single Wall Carbon Nanotubes", The 47th Fullerenes-Nanotubes-Graphene General Symposium, Nagoya University, (2014.9.3-5).

14. Syahril Siregar, **E. H. Hasdeo**, Ahmad R.T. Nugraha, Hsiang Liu, R. Saito: "G* band Raman spectra of single layer graphene revisited", The 48th Fullerenes-Nanotubes-Graphene General Symposium, The University of Tokyo, (2015.2.21-23).

15. **E. H. Hasdeo**, Ahmad R. T. Nugraha, R. Saito: "Kohn anomaly meets Fano resonance in G and G′ bands Raman spectra ofgraphene", The 48th Fullerenes-Nanotubes-Graphene General Symposium, The University of Tokyo, (2015.2.21-23).

16. Muhammad Shoufie Ukhtary, **E. H. Hasdeo**, Ahmad R.T. Nugraha, R. Saito: "Surface plasmon excitations in graphene", The 48th Fullerenes-Nanotubes-Graphene General Symposium, The University of Tokyo , (2015.2.21-23).

17. Pourya Ayria, Ahmad R.T. Nugraha, **E. H. Hasdeo**, S. Tanaka, R. Saito: "Photon energy dependence of angle resolved photoemission spectroscopy in graphene", The 48th Fullerenes-Nanotubes-Graphene General Symposium, The University of Tokyo, (2015.2.21-23).

18. A. R. T. Nugraha, **E. H. Hasdeo**, R. Saito: "Coherent and squeezed states of phonons in single wall carbon nanotubes", 29th International Winterschool on Electronic Properties of Novel Materials: "Molecular nanostructures", Kirchberg, Austria, (2015.3.7-14).

19. **E. H. Hasdeo**, A. R. T. Nugraha, R. Saito: "Interplay of electron-phonon and electron-electron interactions in gate modulated Raman spectroscopy of graphene", NT15: The Sixteenth International Conference on the Science and Application of Nanotubes, Nagoya University, Japan, (2015.06.29-07.03).

20. P. Ayria, A. R. T. Nugraha, **E. H. Hasdeo**, S. Tanaka, R. Saito: "Photon energy dependence of ARPES in graphene", NT15: The Sixteenth International Conference on the Science and Application of Nanotubes, Nagoya University, Japan, (2015.06.29-07.03).

21. A. R. T. Nugraha, **E. H. Hasdeo**, R. Saito: "Squeezed phonons in single wall carbon nanotubes", NT15: The Sixteenth International Conference on the Science and Application of Nanotubes, Nagoya University, Japan, (2015.06.29-07.03).

22. M. S. Ukhtary, **E. H. Hasdeo**, A. R. T. Nugraha, R. Saito: "Switching of electromagnetic wave by graphene", NT15: The Sixteenth International Conference on the Science and Application of Nanotubes, Nagoya University, Japan, (2015.06.29-07.03).

23. **E. H. Hasdeo**, A. R. T. Nugraha, R. Saito: "Screening of electron-phonon coupling due to electron-electron interaction in graphene", 6th A3 symposium on Emerging Materials, Kyushu University, Fukuoka, (2015.11.9-11).

24. A. R. T. Nugraha, **E. H. Hasdeo**, R. Saito: "Coherent phonons and single phonon mode generation in carbon nanotubes", 6th A3 symposium on Emerging Materials, Kyushu University, Fukuoka, (2015.11.9-11).

25. **E. H. Hasdeo**, Ahmad R. T. Nugraha, R. Saito: "Asymmetric Kohn anomaly in G′ band of graphene", The 50th Fullerenes-Nanotubes-Graphene General Symposium, The University of Tokyo, (2016.2.20-22).

26. **E. H. Hasdeo**, Ahmad R. T. Nugraha, R. Saito: "Kohn anomaly and quantum interference of one- and two-phonon Raman spectra in graphene", NT16: The Seventeenth International Conference on the Science and Application of Nanotubes and Low-dimensional Materials, University of Vienna, Austria, (2016.8.7-13).

Bibliography

[1] K. S. Novoselov, A. K. Geim, S. V. Morozov, D. Jiang, Y. Zhang, S. V. Dubonos, I. V. Grigorieva, and A. A. Firsov, Science **306**, 666 (2004).

[2] P. R. Wallace, Phys. Rev. **71**, 622 (1947).

[3] K. S. Novoselov, Z. Jiang, Y. Zhang, S. V. Morozov, H. L. Stormer, U. Zeitler, J. C. Maan, G. S. Boebinger, P. Kim, and A. K. Geim, Science **315**, 1379 (2007).

[4] Y. Zhang, Y.-W. Tan, H. L. Stormer, and P. Kim, Nature **438**, 201 (2005).

[5] C. W. J. Beenakker, Rev. Mod. Phys. **80**, 1337 (2008).

[6] C. Popovici, O. Oliveira, W. de Paula, and T. Frederico, Phys. Rev. B **85**, 235424 (2012).

[7] K. Sengupta and G. Baskaran, Phys. Rev. B **77**, 045417 (2008).

[8] Z. Jiang, Y. Zhang, H. L. Stormer, and P. Kim, Phys. Rev. Lett. **99**, 106802 (2007).

[9] R. Saito, K. Sato, P.T. Araujo, D.L. Mafra, and M.S. Dresselhaus, Solid State Communications **175-176**, 18 (2013).

[10] H. Petroski, "The Pencil: A History of Design and Circumstance", Knopf, New York (1989).

[11] A. K. Geim and A. H. MacDonald, Physics Today **60**, 35 (2007).

[12] M. I. Katsnelson, K. S. Novoselov, and A. K. Geim, Nat Phys **2**, 620 (2006).

[13] K. S. Novoselov et al., Nature **438**, 197 (2005).

[14] O. Klein, Zeitschrift für Physik **53**, 157 (1929).

[15] V. V. Cheianov and V. I. Fal'ko, Phys. Rev. B **74**, 041403 (2006).

[16] T. Ando, T. Nakanishi, and R. Saito, J. Phys. Soc. Jpn. **67**, 2857 (1998).

[17] C. Bai and X. Zhang, Phys. Rev. B **76**, 075430 (2007).

[18] P. A. Lee and A. D. Stone, Phys. Rev. Lett. **55**, 1622 (1985).

[19] R. Saito, M. Hofmann, G. Dresselhaus, A. Jorio, and M. S. Dresselhaus, Advances in Physics **60**, 413 (2011).

[20] H.-L. Liu, S. Siregar, E. H. Hasdeo, Y. Kumamoto, C.-C. Shen, C.-C. Cheng, L.-J. Li, R. Saito, and S. Kawata, Carbon **81**, 807 (2015).

[21] D. L. Mafra, G. Samsonidze, L. M. Malard, D. C. Elias, J. C. Brant, F. Plentz, E. S. Alves, and M. A. Pimenta, Phys. Rev. B **76**, 233407 (2007).

[22] J. F. Rodriguez-Nieva, E. B. Barros, R. Saito, and M. S. Dresselhaus, Phys. Rev. B **90**, 235410 (2014).

[23] L. G. Cancado, A. Jorio, E. H. Martins Ferreira, F. Stavale, C. A. Achete, R. B. Capaz, M. V. O. Moutinho, A. Lombardo, T. S. Kulmala, and A. C. Ferrari, Nano Lett. **11** 3190 (2011).

[24] D. M. Basko, Phys. Rev. B **79**, 205428 (2009).

[25] B. Krauss, P. Nemes-Incze, V. Skakalova, L. Biro, K. von Klitzing, and J. H. Smet, Nano Letters **10**, 4544 (2010).

[26] W. Ren, R. Saito, L. Gao, F. Zheng, Z. Wu, B. Liu, M. Furukawa, J. Zhao, Z. Chen, and H.-M. Cheng, Phys. Rev. B **81**, 035412 (2010).

[27] R. Saito, M. Furukawa, G. Dresselhaus, and M. S. Dresselhaus, Journal of Physics: Condensed Matter **22**, 334203 (2010).

[28] D. Yoon, D. Jeong, H. Lee, R. Saito, Y. Son, H. Lee, and H. Cheong, Carbon **61**, 373 (2013).

[29] W. Kohn, Phys. Rev. Lett. **2**, 393 (1959).

[30] M. Mohr, J. Maultzsch, E. Dobardzic, S. Reich, I. Milosevic, M. Damnjanovic, A. Bosak, M. Krisch, and C. Thomsen, Phys. Rev. B **76**, 035439 (2007).

[31] J. Maultzsch, S. Reich, and C. Thomsen, Phys. Rev. B **70**, 155403 (2004).

[32] S. Piscanec, M. Lazzeri, F. Mauri, A. C. Ferrari, and J. Robertson, Phys. Rev. Lett. **93**, 185503 (2004).

[33] P. T. Araujo, D. L. Mafra, K. Sato, R. Saito, J. Kong, and M. S. Dresselhaus, Phys. Rev. Lett. **109**, 046801 (2012).

[34] K. Sasaki, R. Saito, K. Wakabayashi, and T. Enoki, Journal of the Physical Society of Japan **79**, 044603 (2010).

[35] J. Yan, Y. Zhang, P. Kim, and A. Pinczuk, Phys. Rev. Lett. **98**, 166802 (2007).

[36] A. Das, S. Pisana, B. Chakraborty, S. Piscanec, S. K. Saha, U. V. Waghmare, K. S. Novoselov, H. R. Krishnamurthy, A. K. Geim, A. C. Ferrari, and A. K. Sood, Nat Nano **3**, 210 (2008).

[37] D. L. Mafra, J. Kong, K. Sato, R. Saito, M. S. Dresselhaus, and P. T. Araujo, Phys. Rev. B **86**, 195434 (2012).

[38] T. Ando, J. Phys. Soc. Jp. **75**, 024707 (2006).

[39] M. Lazzeri, S. Piscanec, F. Mauri, A. C. Ferrari, and J. Robertson, Phys. Rev. B **73**, 155426 (2006).

[40] K. Sasaki, K. Kato, Y. Tokura, S. Suzuki, and T. Sogawa, Phys. Rev. B **86**, 201403 (2012).

[41] C.-F. Chen, C.-H. Park, B. W. Boudouris, J. Horng, B. Geng, C. Girit, A. Zettl, M. F. Crommie, R. A. Segalman, S. G. Louie, and F. Wang, Nature **471**, 617 (2011).

[42] J. Jiang, R. Saito, A. Grüneis, G. Dresselhaus, and M.S. Dresselhaus, Chemical Physics Letters **392**, 383 (2004).

[43] K. Sasaki and R. Saito, Prog. Theor. Phys. **176**, 253 (2008).

[44] U. Fano, Phys. Rev. **124**, 1866 (1961).

[45] E. H. Hasdeo, A. R. T. Nugraha, M. S. Dresselhaus, and R. Saito, Phys. Rev. B **90**, 245140 (2014).

[46] P. C. Eklund and K. R. Subbaswamy, Phys. Rev. B **20**, 5157 (1979).

[47] S. D. M. Brown, A. Jorio, P. Corio, M. S. Dresselhaus, G. Dresselhaus, R. Saito, and K. Kneipp, Phys. Rev. B **63**, 155414 (2001).

[48] M. A. Pimenta, A. Marucci, S. Empedocles, M. Bawendi, E. B. Hanlon, A. M. Rao, P. C. Eklund, R. E. Smalley, G. Dresselhaus, and M. S. Dresselhaus, Phys. Rev. B (R) **58**, R16016 (1998).

[49] A. M. Rao, E. Richter, Shunji Bandow, Bruce Chase, P. C. Eklund, K. A. Williams, S. Fang, K. R. Subbaswamy, M. Menon, A. Thess, R. E. Smalley, G. Dresselhaus, and M. S. Dresselhaus, Science **275**, 187 (1997).

[50] H. Farhat, S. Berciaud, M. Kalbac, R. Saito, T. F. Heinz, M. S. Dresselhaus, and J. Kong, Phys. Rev. Lett. **107**, 157401 (2011).

[51] E. H. Hasdeo, A. R. T. Nugraha, K. Sato, M. S. Dresselhaus, and R. Saito, Phys. Rev. B **88**, 115107 (2013).

[52] T. Ando, J. Phys. Soc **75**, 124701 (2006).

[53] M. Lazzeri and F. Mauri, Phys. Rev. Lett. **97**, 266407 (2006).

[54] A. H. Castro Neto, F. Guinea, N. M. R. Peres, K. S. Novoselov, and A. K. Geim, Rev. Mod. Phys. **81**, 109 (2009).

[55] G. S. Painter and D. E. Ellis, Phys. Rev. B **1**, 4747 (1970).

[56] R. Saito, G. Dresselhaus, and M. S. Dresselhaus, Phys. Rev. B **61**, 2981 (2000).

[57] K. F. Mak, J. Shan, and T. F. Heinz, Phys. Rev. Lett. **106**, 046401 (2011).

[58] G. Samsonidze. *Photophysics of Carbon Nanotubes*. Ph. D. thesis, Massachusetts Institute of Technology, Department of Electrical Engineering and Computer Science, 2006.

[59] S. M. Bachilo, M. S. Strano, C. Kittrell, R. H. Hauge, R. E. Smalley, and R. B. Weisman, Science **298**, 2361 (2002).

[60] R. B. Weisman and S. M. Bachilo, Nano Lett. **3**, 1235 (2002).

[61] D. Chae, T. Utikal, S. Weisenburger, H. Giessen, K. von Klitzing, M. Lippitz, and J. Smet, Nano Letters **11**, 1379 (2011).

[62] D. Porezag, Th. Frauenheim, Th. Köhler, G. Seifert, and R. Kaschner, Phys. Rev. B **51**, 12947 (1995).

[63] O. Dubay and G. Kresse, Phys. Rev. B **67**, 035401 (2003).

[64] M. S. Dresselhaus, G. Dresselhaus, and A. Jorio, "Group Theory Application to the Physics of Condensed Matter", Springer, (2008).

[65] J. Maultzsch, S. Reich, C. Thomsen, H. Requardt, and P. Ordejon, Phys. Rev. Lett. **92**, 075501 (2004).

[66] A. Grüneis, J. Serrano, A. Bosak, M. Lazzeri, S. L. Molodtsov, L. Wirtz, C. Attaccalite, M. Krisch, A. Rubio, F. Mauri, and T. Pichler, Phys. Rev. B **80**, 085423 (2009).

[67] S. Weinberg, "Lectures on Quantum Mechanics", Cambridge, (2015).

[68] L. M. Woods and G. D. Mahan, Phys. Rev. B **61**, 10651 (2000).

[69] K. Sasaki, R. Saito, G. Dresselhaus, M. S. Dresselhaus, H. Farhat, and J. Kong, Phys. Rev. B **78**, 235405 (2008).

[70] P. Venezuela, M. Lazzeri, and F. Mauri, Phys. Rev. B **84**, 035433 (2011).

[71] R. M. Martin and L. M. Falicov, in *Light Scattering in Solids I: edited by M. Cardona*, 79, (Springer-Verlag, Berlin, 1983), Vol. 8. Chapter 3, Topics in Applied Physics.

[72] J. Liu, Q. Li, Y. Zou, Q. Qian, Y. Jin, G. Li, K. Jiang, and S. Fan, Nano Letters **13**, 6170 (2013).

[73] A. Jorio, M. S. Dresselhaus, R. Saito, and G. Dresselhaus. "Raman Spectroscopy in Graphene Related Systems", Wiley, (2011).

[74] J. Friedman and R. M. Hochstrasser, Chem. Phys. Lett. **32**, 414 (1975).

[75] J. Jiang, R. Saito, Ge. G. Samsonidze, A. Jorio, S. G. Chou, G. Dresselhaus, and M. S. Dresselhaus, Phys. Rev. B **75**, 035407 (2007).

[76] V. Perebeinos, J. Tersoff, and P. Avouris, Phys. Rev. Lett. **92**, 257402 (2004).

[77] E. H. Hwang and S. Das Sarma, Phys. Rev. B **75**, 205418 (2007).

[78] J. Jiang, R. Saito, K. Sato, J. S. Park, Ge. G. Samsonidze, A. Jorio, G. Dresselhaus, and M. S. Dresselhaus, Phys. Rev. B **75**, 035405 (2007).

[79] K Sasaki, K. Kato, Y Tokura, S Suzuki, and T. Sogawa, Phys. Rev. B **85**, 075437 (2012).

[80] S. Berciaud, X.L. Li, H. Htoon, L. E. Brus, S. K. Doorn, and T. F. Heinz, Nano Letters **13**, 3517 (2013).

[81] R. Rao, R. Podila, R. Tsuchikawa, J. Katoch, D. Tishler, A. M. Rao, and M. Ishigami, ACS Nano **5**, 1594 (2011).

[82] M. Bruna, A. K. Ott, M. Ijäs, D. Yoon, U. Sassi, and A. C. Ferrari, ACS Nano **8**, 7432 (2014).

[83] Y. Saito, Y. Tani, N. Miyagawa, K. Mitsushima, A. Kasuya, and Y. Nishina, Chem. Phys. Lett. **294**, 593 (1998).

[84] G. Kresse, J. Furthmüller, and J. Hafner, Europhys. Lett. **32**, 729 (1995).

[85] P. Pavone, R. Bauer, K. Karch, O. Schütt, S. Vent, W. Windl, D. Strauch, S. Baroni, and S. de Gironcoli, Physica B **219–220**, 439 (1996).

[86] N. Mounet and N. Marzari, Phys. Rev. B **71**, 205214 (2005).

[87] L. Wirtz and A. Rubio, Solid State Commun. **131**, 141 (2004).

[88] A. Grüneis, R. Saito, Ge. G. Samsonidze, T. Kimura, M. A. Pimenta, A. Jorio, A. G. Souza Filho, G. Dresselhaus, and M. S. Dresselhaus, Phys. Rev. B **67**, 165402 (2003).